
Electronic Thesis and Dissertation Repository

8-7-2013 12:00 AM

Approaches Toward Combining Positron Emission Tomography with Magnetic Resonance Imaging

Geron A. Bindseil
The University of Western Ontario

Supervisor
Prof. Blaine Chronik
The University of Western Ontario

Graduate Program in Physics
A thesis submitted in partial fulfillment of the requirements for the degree in Doctor of Philosophy
© Geron A. Bindseil 2013

Follow this and additional works at: <https://ir.lib.uwo.ca/etd>



Part of the [Physics Commons](#)

Recommended Citation

Bindseil, Geron A., "Approaches Toward Combining Positron Emission Tomography with Magnetic Resonance Imaging" (2013). *Electronic Thesis and Dissertation Repository*. 1419.
<https://ir.lib.uwo.ca/etd/1419>

This Dissertation/Thesis is brought to you for free and open access by Scholarship@Western. It has been accepted for inclusion in Electronic Thesis and Dissertation Repository by an authorized administrator of Scholarship@Western. For more information, please contact wlsadmin@uwo.ca.

APPROACHES TOWARD COMBINING POSITRON EMISSION
TOMOGRAPHY WITH MAGNETIC RESONANCE IMAGING

Integrated Article Thesis

by

Geron André Bindseil

Graduate Program in Physics

A thesis submitted in partial fulfillment
of the requirements for the degree of
Doctor of Philosophy

The School of Graduate and Postdoctoral Studies
The University of Western Ontario
London, Ontario, Canada

© Geron A Bindseil 2013

Abstract

Positron emission tomography (PET) and magnetic resonance imaging (MRI) provide complementary information, and there has been a great deal of research effort to combine these two modalities. A major engineering hurdle is that photomultiplier tubes (PMT), used in conventional PET detectors, are sensitive to magnetic field. This thesis explores the design considerations of different ways of combining small animal PMT-based PET systems with MRI through experimentation, modelling and Monte Carlo simulation. A proof-of-principle hybrid PET and field-cycled MRI system was built and the first multimodality images are shown. A Siemens Inveon PET was exposed to magnetic fields of different strengths and the performance is characterized as a function of field magnitude. The results of this experiment established external magnetic field limits and design studies are shown for wide range of approaches to combining the PET system with various configurations of field-cycled MRI and superconducting MRI systems. A sophisticated Monte Carlo PET simulation workflow based on the GATE toolkit was developed to model the Siemens Inveon PET. Simulated PET data were converted to the raw Siemens list-mode format and were processed and reconstructed using the same processing chain as the data measured on the actual scanner. A general GATE add-on was developed to rapidly generate attenuation correction sinograms using the precise detector geometry and attenuation coefficients built into the emission simulation. Emission simulations and the attenuation correction add-on were validated against measured data. Simulations were performed to study the impact of radiofrequency coil components on PET image quality and to test the suitability of various MR-compatible materials for a dual-modality animal bed.

Keywords

Positron Emission Tomography, Magnetic Resonance Imaging, PET-MRI, Hybrid Systems, Multimodality, Monte Carlo Simulation, Image Quality

Co-Authorship Statement

Chad Harris wrote the code for the boundary element method used in designing the electromagnetic shield coil in Chapter 3. Will Handler and Tim Scholl wrote the software for all other electromagnetic and thermal calculations in Chapter 3. Kyle Gilbert, Will Handler, Tim Scholl and Blaine Chronik developed and constructed the field-cycled magnetic resonance imaging system used in Chapter 4. Will Handler wrote data acquisition software for the positron emission tomography system described in Chapter 4. Hao Peng and Will Handler assembled the PET detector module in Chapter 4.

Acknowledgments

I would like to convey my sincere appreciation for help and mentoring given by my supervisor, Blaine Chronik. Throughout my thesis work, I have benefited greatly from the ideas, assistance and advice of William Handler. I benefited from the support and helpful advice of my advisory committee, Tamie Poepping and Lyudmila Goncharova. I am thankful for the generous scholarship support I received from NSERC. I would like to thank the following people for sharing ideas and technical assistance as well as helping me grow as a researcher over the past six years: Tim Scholl, Chad Harris, Kyle Gilbert, Parisa Hudson, Jamu Alford, Rebecca Feldman, Dustin Haw and Andrew Boivin. Special thanks to my brother, Marsh, who helped find all the the typos. Finally, my deepest gratitude goes to my wife, Nicole, who supported me tirelessly throughout my studies.

Dedication

I dedicate this thesis to my father and mother, Gerhart and Edie, who passed from this world during my studies.

Table of Contents

Abstract	ii
Co-Authorship Statement.....	iv
Dedication	vi
Table of Contents	vii
List of Tables	xii
List of Figures	xiii
List of Appendices	xxv
Preface.....	xxvi
1 Combining PET with MRI: An Introduction	1
1.1 Why PET-MRI?	1
1.1.1 Principles of PET	2
1.1.2 Principles of MRI.....	5
1.1.3 The Complementary Roles of PET and MRI.....	6
1.2 Technical Challenges for Combining PET with MRI.....	6
1.2.1 Sensitivity of PET Detectors to the MRI Environment	7
1.2.2 Attenuation Correction of PET Data.....	8
1.2.3 Design Considerations for MR Hardware.....	10
1.3 Monte Carlo PET Simulation.....	11
1.4 PET Detectors	13
1.5 Developments in Combined PET-MRI.....	16
1.6 Thesis Overview	17
1.7 References.....	23
2 Magnetic field exposure tests on a Siemens Inveon small animal PET system.....	31

2.1	Introduction.....	31
2.2	Materials and Methods.....	33
2.2.1	PET System Description.....	33
2.2.2	Magnetic Field Test Setup	34
2.2.3	Phantom Descriptions and Acquisition Parameters.....	37
2.2.4	Reconstruction Parameters and Analysis Methods.....	37
2.3	Results.....	40
2.3.1	Count Rate and Attenuation Coefficient.....	40
2.3.2	Image Resolution and Positioning Accuracy	42
2.3.3	Position Profiles, Energy Spectra and Time Resolution.....	44
2.3.4	Efficiency Maps	49
2.4	Discussion	51
2.5	Conclusion	55
2.6	Acknowledgements.....	55
2.7	References.....	56
3	Approaches to Combining the Siemens Inveon PET with MRI	58
3.1	Introduction.....	58
3.2	Combining the Inveon PET with Field-Cycled MRI.....	59
3.2.1	Interleaved Field-Cycled MRI – Common Imaging Region	61
3.2.2	Sequential Imaging with PET Docked to FCMRI	65
3.3	Combining the Inveon PET with Conventional Superconducting MRI Systems	69
3.3.1	Dynamically-Controlled Electromagnetic Shielding of the PET Scanner.....	70
3.3.2	Separating the PET and MRI Scanners in the Same Room.....	78
3.4	References.....	88

4	First Image from a Combined PET and Field-cycled MRI System	90
4.1	Introduction.....	90
4.2	Methods.....	94
4.3	Results.....	97
4.4	Discussion and Conclusions	100
4.5	Acknowledgements.....	103
4.6	References.....	104
5	Validation Tests on a Monte Carlo PET Simulation Architecture based on GATE	107
5.1	Introduction.....	107
5.2	Materials & Methods	109
5.2.1	Description of the NEMA NU 4-2008 Image Quality Phantom.....	109
5.2.2	Monte Carlo Simulation Architecture.....	112
5.2.3	Simulated Data Processing Chain.....	114
5.2.4	Experimental PET Acquisition	116
5.2.5	Image Reconstruction and Analysis.....	117
5.3	Results.....	118
5.4	Discussion.....	122
5.5	Conclusion	123
5.6	Acknowledgement	124
5.7	References.....	125
6	Attenuation Correction Sinogram Add-On to GATE	127
6.1	Introduction.....	127
6.1.1	Principles of Attenuation Correction	128
6.1.2	Attenuation Correction in Monte Carlo PET Studies	133
6.2	Methods.....	134

6.2.1	Concept	134
6.2.2	Implementation	135
6.2.3	Validation Testing.....	137
6.3	Results of Validation.....	142
6.3.1	Accuracy of Attenuation Maps	142
6.3.2	Comparison of Simulated and Measured PET Images	144
6.4	Discussion and Conclusion	147
6.5	References.....	150
7	Effect of MR-Compatible Bed Materials and RF Coil Components on PET Performance	152
7.1	Monte Carlo PET Simulation of Effect on Image Quality of Various MR-Compatible Animal Bed Materials	152
7.1.1	Introduction.....	152
7.1.2	Methods.....	153
7.1.3	Results.....	156
7.1.4	Discussion and Conclusions	157
7.2	Design Considerations of RF Coils for PET-MRI Applications and their Impact on PET Performance.....	158
7.2.1	Introduction.....	158
7.2.2	Methods.....	159
7.2.3	Results.....	165
7.2.4	Discussion and Conclusions	169
7.3	References.....	170
8	Conclusion and Future Work	172
8.1	Thesis Summary.....	172
8.2	Future Work	174

8.3 Conclusion	175
Appendix A.....	177
A.1 Code to Convert GATE ROOT Output to Siemens Inveon List-mode Format (<i>root2lst_multi</i>).....	177
A.2 Batch Script to Split GATE Simulations into Multiple Runs for Parallel Processing on Multi-CPU Computers.....	178
A.3 Specification of the NEMA NU 4-2008 Phantom and Source Macros in GATE.....	179
A.4 GATE Attenuation Correction Add-on.....	180
Letters of Permission	182
Curriculum Vitae	187

List of Tables

Table 3.1: Electromagnetic and physical characteristics of the candidate shield coil.	73
Table 5.1: Material definitions for NEMA NU 4-2008 image quality phantom.	111
Table 6.1: Comparison of linear attenuation coefficients used by the GATE simulation with values measured from the reconstructed attenuation maps.....	144
Table 7.1: Material definitions used in PET simulations for MR-compatible animal holders.....	155
Table 7.2: Simulated PET Performance Measures for Various Bed Construction Materials. ^a	156
Table 7.3: Comparison of simulation results for the cases with and without RF coil.	165
Table 7.4: Mean relative activity in the central slice for scatter correction enabled or disabled.	168

List of Figures

Figure 1.1: Schematic showing a PET detector ring (left) and a drawing of the operation of a PSPMT-based scintillation detector (right). A positron annihilation results in two photons, each of which can be detected by a single detector. If an annihilation photon is stopped by a scintillation crystal, a flash of light will appear in the scintillator, which causes electrons to be ejected from the photocathode within the photomultiplier detector. The initial electrons are accelerated through a dynode chain, with each successive dynode at a higher potential. At each dynode the number of electrons increases until the flood of electrons reach the final anode and cause a negative pulse in the anode output voltage signal. The voltage pulses from all the detectors are fed into the coincidence detection electronics. 15

Figure 2.1: Photographs of the geometry of the experimental setup. The current through the electromagnet was varied to produce a range of magnetic field magnitudes through the PET detectors. 35

Figure 2.2: Simulated contour map of the magnetic field magnitude in the vicinity of the PET detectors. The dark and light grey boxes indicate the position and size of the scintillator crystal and position-sensitive photomultiplier tube, respectively. The arrows show the direction of the magnetic field within each photomultiplier tube. For illustration, contour values are shown for an applied current of 3.46 A producing an average field of 1 mT within the photomultiplier tubes. 36

Figure 2.3: (a) Plot of prompts rate and reconstructed activity normalized to the value at zero field as a function of applied magnetic field for the cylinder source. The reconstructed activity values are also shown after adjusting to account for changes in the attenuation coefficient relative to the attenuation coefficient measured at zero field. (b) Plot of mean attenuation coefficient as a function of applied magnetic field.

The proportional decline of the attenuation coefficient as the field increased appears to correlate with the increasing divergence between the prompts rate and the reconstructed activity. The error bars are estimated from repeated emission and transmission scans (20 repetitions) and uncertainty in the temperature measurement.

(c) Reconstructed images of the cylindrical source at various fields showing the central axial slice (top) and the central coronal slice (bottom) using the same contrast colour scheme. All emission data were corrected for the decay of Ge-68 and gantry temperature. 41

Figure 2.4: Full width at half maximum in each direction for the reconstructed image of a point source located at nine positions in the field of view as a function of magnetic field. The uncertainty in positioning was estimated by taking the standard deviation for multiple repetitions at zero field: ± 0.01 mm for radial (x); ± 0.007 mm for tangential (y); and ± 0.005 mm for axial (z)..... 43

Figure 2.5: Position displacement as a function of magnetic field relative to the case at zero field for images of a reconstructed point source at nine positions in the field of view. The uncertainty in positioning was estimated by taking the standard deviation for multiple repetitions at zero field: ± 0.06 mm for radial (x); ± 0.004 mm for tangential (y); and ± 0.01 mm for axial (z). To set the x position, the point source cube was positioned manually against a stopper, increasing the positioning uncertainty for the radial (x) direction. 44

Figure 2.6: Analysis of flood source position profiles for the same detector block at different field strengths (topmost position farthest from the bed side). (a) The energy bins of the photopeak maxima are shown for three separate crystals: Top left corner (position $[x,y] = [0,0]$), top centre (position $[10,0]$) and centre (position $[10,10]$). The dashed line indicates the approximate upper extent of noise in the energy spectra where the noise shoulder would dominate the photopeak. (b) The energy resolution of

each photopeak (FWHM) is shown as a function of magnetic field. (c) The peaks in the position profiles correspond to the coordinates of scintillation events in each of the 400 crystals in the detector. Up to 2.0 mT, positions could be clearly identified for each crystal in most detectors. At 3.0 mT, the crystals near the centres of most blocks had very few counts and the positions could not be identified. 46

Figure 2.7: Emission energy spectra for the three crystal indices analyzed in Figure 2.6 shown at various field strengths. The spectra shown are screen captures from the detector setup utility and are given without axes. The number of bins on the horizontal axis is 1024 and each spectrum is normalized to the same vertical height. The red vertical line in each spectrum indicates the energy bin of the photopeak (511 keV). As the field increased, the energy bin of the photopeak tended to decrease, consistent with a reduction in absolute detector efficiency. All photopeaks were distinguishable from the noise threshold up to 0.9 mT..... 47

Figure 2.8: Transmission energy spectra for the three crystal indices analyzed in Figure 2.6 and Figure 2.7 shown at various field strengths. The energy of the photopeak was 122 keV. The energy bin of the photopeak in the transmission energy spectra tended to decrease with increasing magnetic field, similar to the case for the emission data..... 48

Figure 2.9: Block time resolution as a function of magnetic field for the same detector block as in Figure 2.6..... 49

Figure 2.10: (a) & (b) Efficiency map of the same ring of 16 detector blocks closest to the bed side of the scanner at various magnetic field magnitudes for emission data (a) and for blank transmission data (b). The three other rings of blocks are not displayed, but showed a similar response. The greyscales represent the counts assigned to each crystal normalized to the acquisition at zero field. (c) & (d) An expanded view of the

particular block highlighted by the cyan box. The white dashed lines represent the bounds of the pixels used to produce the line profiles in (e) & (f) at various field strengths. 50

Figure 3.1: Cross-sectional view through a design of a PET/FCMRI system showing PET ring (center), polarizing magnet (two inner coils on either side of the PET ring) and readout magnet (six outer coils). The inner diameter is 16 cm. 62

Figure 3.2: A prototypical timing sequence for the interleaved PET-FCMRI system. PET data can be acquired while all magnetic fields are switched off. B_p represents the strong polarizing magnetic field, B_r represents the homogeneous and stable readout magnetic field, RF refers to radiofrequency pulses, and G refers to gradient coil operation. 63

Figure 3.3: Cross-sectional view through the design of the FCMRI system. Shown (starting from center): 10-cm-diameter imaging volume, birdcage RF coil, RF shield, gradient set, second-order shims, main magnet. Liquid cooling inlet manifold shown on ends. 66

Figure 3.4: Docking geometry of the combined PET and field-cycled MRI system. An extendible bed (not shown) would move the subject between PET and MR imaging regions using the built in bed motion control system of the PET scanner. No modifications to the PET system would be necessary; however, a different bed would need to be constructed. 67

Figure 3.5: Geometry of the PET-FCMRI docked system showing support structures. 67

Figure 3.6: Geometry of the PET-MRI concept with active electromagnetic shielding. Shield coil windings are shown without the coil support structure. 72

Figure 3.7: Plot of magnetic field magnitude as a function of distance from the centre of the MRI scanner at a radial distance $r = 10$ cm (the radial distance of the PMTs in the PET detector ring). The magnetic field magnitude at the PET detectors is reduced by two orders of magnitude when the shield coil is energized. The PET system can be moved up to 10 cm closer to the shield coil and any distance farther and still experience a magnetic field below the target threshold. 74

Figure 3.8: Magnetic field magnitude map in the vicinity of the PET detectors without shielding (top) and with shielding (bottom). Field data for the 2 T MRI was obtained from the manufacturer and field data for the coil was from a Biot-Savart Law model implemented in MATLAB which does not include the susceptibility of the PET detectors. Note that the colourmaps have different scales. The origin of the coordinate system is the MRI isocentre. The dashed line shows the location of the four PMTs that make up one module. To account for positioning error, the shield coil was designed to null the field over the entire region shown. The maximum magnitude field in the detectors was 8.2 mT without shielding and 0.08 mT with shielding. The jaggedness of the contour lines are due to coarse sampling. 75

Figure 3.9: Proposed floor plan for the actively shielded PET system in the same room as the 2.0 T MRI system. The MRI scanner is represented by the box in the centre of the room. The shield coil (coil dimensions not to scale) is positioned between the Siemens Inveon PET and the MRI scanner. The 5 gauss line (0.5 mT line) is shown. In this arrangement, the PET system can be operated only when the shield coil is energized. 76

Figure 3.10: Proposed floor plan for the PET system in the same room as the 2.0 T MRI system. The MRI scanner, represented by the box, is positioned as far as the room size allows from the PET system. The 5 gauss line (0.5 mT line) is shown. 79

Figure 3.11: Simulated magnetic field magnitude as a function of distance for the PET-MRI arrangement shown in Figure 3.10. For this geometry, the magnetic field direction is primarily in the axial direction with respect to the PET system.	80
Figure 3.12: Alternative side-by-side floor plan for the PET system in the same room as the 2.0 T MRI system. The MRI scanner, represented by the box, is oriented parallel to the PET scanner separated by a certain radial distance. The 5 gauss line (0.5 mT line) is shown.	81
Figure 3.13: Photographs of the PET-MRI scanning room showing the room geometry. The PET and MRI systems are placed on opposite sides of the room.....	82
Figure 3.14: Simulated magnetic field magnitude as a function of radial distance for the side-by-side PET-MRI arrangement shown in Figure 3.12. Similar to the axial collinear geometry, the magnetic field direction is also primarily in the axial direction with respect to the PET system; however, the magnitude of the field varies across the PET detector ring. For comparison, the grey dashed lines show the (axial) distances of the 0.3 mT and 1 mT field lines and the difference is shown by the arrow.	83
Figure 3.15: Proposed floor plan of a PET-MRI facility in a typical 9.4 T MRI suite with the PET system located in a separate area but part of the same imaging suite. The magnetic field experienced by the PET system is negligible in this location.	84
Figure 3.16: Alternative floor plan for a PET-MRI facility in a typical 9.4 T MRI suite with the PET system in the same room as the MRI system. At this location, the PET detectors would experience a magnetic field of approximately 0.1 mT.	85
Figure 4.1: Schematic of PET detectors in field-cycled MRI system. The two PET detectors are located in the axial gap. All dimensions shown in centimeters.	94

Figure 4.2: Timing diagram for interleaved sequence of field-cycled MRI and PET. B_{pol} provides the initial polarization, and all MR imaging is done during the readout interval. After a delay of 500 ms, PET data acquisition is started. The sequence repeats after a TR of 2752-ms. Relative pulse magnitudes and timing are to scale. .. 96

Figure 4.3: PET image reconstructed using linear interpolation for back-projection in the original resolution (a) and after smoothing (b). The same sinogram was reconstructed using nearest-neighbor interpolation for back-projection and is shown before smoothing (c) and after smoothing (d). Smoothing was performed by applying two iterations by linear interpolation as an aid in visualization on account of the coarseness of the pixels in the original image. 98

Figure 4.4: Smoothed nearest-neighbor PET image (a) and MR (b) image (not to scale). (c) Photograph of the phantom showing radioactive sealed source inside onion. The triangular cavity cuts through the entire onion. (d) Superimposition of PET onto MR image. The PET image was resized so that the separation between PET peaks was 10 mm in MR image space. MR imaging parameters: three-dimensional fast spin-echo; bandwidth = 20.03 kHz; FOV = 10 x 10 x 2 cm; echo train length = 8; N_{avg} = 6; Imaging matrix = 192 x 128 x 6; TR/TE = 2752 ms/21 ms; T_{scan} = 32 min; view = single transverse slice. Here, TR and T_{scan} include PET acquisition stages. 99

Figure 4.5: Conceptual timing for (a) sequential and (b) interleaved imaging sequences for PET and field-cycled MRI. 102

Figure 5.1: Scale drawing of the NEMA NU-2008 image quality phantom. Nylon screws are shown in dark grey and PMMA is shown in light grey. The main body of the phantom is filled with activity-containing water. The two smaller chambers at the top of the phantom contain non-radioactive water (left) and air (right). Six small

nylon screws on the lower face of the phantom and several rubber gaskets are included in the model, but not shown in this drawing. 110

Figure 5.2: Schematic showing the workflow of experimental and simulated data reconstruction and corrections. In the simulation, the attenuation correction sinogram is computed directly from the lines of response through the phantom materials. In contrast, on the physical scanner, to compute the attenuation correction sinogram requires a blank transmission scan in addition to the transmission data with the phantom present. 116

Figure 5.3: Reconstructed PET images of the NEMA NU 4-2008 image quality phantom for experimental data (top) and simulated data (bottom). Two transverse slices and one coronal slice are shown with no interpolation applied. The reconstructed activity distribution in the simulated image shows agreement with the experimental image. Higher noise is visible in the experimental image due to the fewer prompts recorded in the experimental acquisition. 119

Figure 5.4: Mean recovery coefficient as a function of rod diameter for experimental and simulated images. The error bars represent the standard deviation calculated with Equation (5.1). Lines connecting the data points are meant as guides to the eye. The recovery coefficient is lower for the smaller rods because of the partial volume effect. 121

Figure 6.1: Relative probability of Compton scattering as a function of 511 keV photon scattering angle shown in Cartesian form (left) and in polar form (right). The likelihood of small-angle scattering is significantly greater than large-angle scattering. 131

Figure 6.2: Detector geometry of the Siemens Inveon PET showing the approximate angular range for small-angle Compton scattering. The annihilation photon labeled

ray 2 has undergone Compton scattering, but should not be considered as having been attenuated. Attenuation correction factors should be adjusted to exclude the contribution from small-angle scattering. For the Siemens Inveon PET detector configuration shown, it is estimated that 2.8% of singly scattered annihilation photons would result in no change in the LOR or be placed in a nearest neighbour LOR with negligible impact on the final image..... 133

Figure 6.3: Phantom model for testing the accuracy of attenuation maps generated by the simulation. Three rods of different material are shown embedded in a large cylinder of PMMA. The material definitions (density and composition) were the same as those contained in the default materials database distributed with the GATE package. The ‘RibBone’ material definition was used for bone. The linear attenuation coefficient (LAC) values computed by the GATE physics models at 511 keV are shown for PMMA and the three materials used in each test configuration. The dashed circle indicates the location where the LAC value of PMMA was measured in the reconstructed attenuation map. 139

Figure 6.4: Photograph of the Ge-68 phantom used on the physical scanner. A model based on this phantom was used in the simulation. 140

Figure 6.5: (a) & (b) Reconstructed attenuation maps for the two configurations. The greyscale in (a) has a range $0 - 0.23 \text{ cm}^{-1}$ and the range in (b) is $0 - 0.18 \text{ cm}^{-1}$. The streaking visible in the attenuation maps is a property of the discrete number of lines of response and filtered back-projection reconstruction algorithm. (c) & (d) Horizontal line profiles through the centre of the attenuation maps. For each material, the reconstructed attenuation coefficient matched the value generated by the GATE physics models. In the figure, plexiglass refers to PMMA..... 143

Figure 6.6: Axial and coronal views of the reconstructed attenuation maps generated by the GATE add-on (a) and the transmission scan on the actual scanner (b). They greyscale range is $0 - 0.145 \text{ cm}^{-1}$ for both attenuation maps. (c) Line profiles through both attenuation maps show the agreement between simulated and measured attenuation coefficients. 145

Figure 6.7: Filtered back-projection PET emission images for simulated data and data acquired on the physical scanner. Images reconstructed with no attenuation correction are shown on the left, and those with attenuation and scatter corrections applied are shown on the right. The greyscale range for all images is $1 - 10 \text{ kBq/cm}^3$ 146

Figure 6.8: Line profiles through the images reconstructed from simulated data (a) and data measured on the actual scanner (b). 147

Figure 7.1: (a) CAD model of the PET-MRI mouse bed model. Parallel tubes carry anaesthetic gas to and from the nose cone. All anaesthetic gas and heating water lines connect at the rear of the bed. (b) & (c) Schematic of the simulated phantom geometry. The NEMA NU 4-2008 phantom is shown in green with acrylic screws (blue) and rubber gaskets (red) sitting on the animal holder (white). The blue in the bed corresponds to the heating water channels. The grey rods are delrin anaesthetic gas lines. The white wireframe boxes indicate the position of the PET detector scintillator crystal blocks. 154

Figure 7.2: Mean recovery coefficient associated with each activity-containing rod for various animal bed materials. 157

Figure 7.3: Simulation geometry. The band-pass birdcage coil model with low-pass capacitors on the rungs is shown. A high-pass coil was also modeled which had no capacitors on the rungs. The homogenous cylindrical phantom, shown in red, rests on the same PET bed model discussed earlier. The RF coil consists of the following

materials: copper tape (yellow), capacitors (green), terminators (blue), and solder (grey). The RF coil is supported by a copper former (not shown) and the wireframe shows the location of the RF shield. 162

Figure 7.4: 511 keV attenuation maps of the central transverse plane with no RF coil (left), the high-pass RF coil (middle), and the band-pass RF coil (right). The maps show linear attenuation coefficient and were reconstructed from the attenuation correction sinogram. The capacitor attenuation coefficient was $\sim 0.7 \text{ cm}^{-1}$; however, all maps were windowed with a scale $0 - 0.4 \text{ cm}^{-1}$. A smoothing filter (linear interpolation) was applied. In the band-pass RF coil attenuation map, the streaks are due to the abrupt difference in attenuation coefficient between the capacitors and the adjacent material and arise because of the nature of the sampling of the sinogram and reconstruction algorithm. 163

Figure 7.5: Reconstructed PET images showing the central axial slice. The greyscale has units Bq/voxel. The images on the left correspond to the simulation with no RF coil present, and those on the right are for the case with the RF coil, including the RF coil in attenuation and scatter corrections. The top row shows the PET images with a zoom factor of 2 and full greyscale. Increased noise (25% higher standard deviation) and a circular-shape artifact are apparent in the RF coil image (top right) when compared to the case with no RF coil (top left). The bottom row shows the full field of view windowed to make the background noise visible. The case with the RF coil (bottom right) shows significantly increased noise outside the phantom when compared with the case with no RF coil (bottom left). A symmetric artifact arising from the ring of 8 capacitors is evident. 166

Figure 7.6: Relative reconstructed activities averaged over the phantom volume are shown for simulations with the two RF coil models and scatter correction. The activity values are scaled to a reference image from a simulation with no RF coil

present (100%). Omitting the RF coil in the attenuation correction (AC) results in a significant underestimation of the activity. Error bars were too small to be visible. 167

Figure 7.7: Axial profile of the mean activity with scatter correction. Four slices were averaged to produce each data point. The presence of rung capacitors in the band-pass coil results in greater variation across the image along the axial direction. 168

List of Appendices

A.1	Code to Convert GATE ROOT Output to Siemens Inveon List-mode Format (<i>root2lst_multi</i>).....	177
A.2	Batch Script to Split GATE Simulations into Multiple Runs for Parallel Processing on Multi-CPU Computers.....	178
A.3	Specification of the NEMA NU 4-2008 Phantom and Source Macros in GATE	179
A.4	GATE Attenuation Correction Add-on.....	180

Preface

This thesis is the original work of Geron Bindseil. A version of Chapter 4 has been published. Manuscripts based on Chapters 2, 5, 6 and 7 were in preparation at the time of the publication of this thesis.

Chapter 1

1 Combining PET with MRI: An Introduction

This thesis examines a variety of approaches to combining two imaging modalities: positron emission tomography (PET) and magnetic resonance imaging (MRI). The focus of these investigations was to explore how an MRI system can affect PET and ways of minimizing interactions. This thesis includes magnetic field exposure tests on a small animal PET system, an analysis of the feasibility of various approaches of combining a specific PET scanner with MRI, experimental work on a proof-of-principle PET-MRI system, validation tests of a comprehensive Monte Carlo PET simulation methodology, and a Monte Carlo study of the effects of MR-compatible bed materials and radiofrequency (RF) coil components on PET imaging performance. In this introduction, I describe the primary motivations and technical challenges associated with combining PET and MRI. In addition, I discuss Monte Carlo based modelling techniques for PET imaging. I also survey combined PET-MRI implementations to-date. Finally, I provide a thesis overview.

1.1 Why PET-MRI?

Work towards combining PET and MRI has been an active area of research and development. The motivation for using PET and MR image data together comes from the complementary information provided by the fundamentally different contrast mechanisms of the two modalities.

1.1.1 Principles of PET

In PET, a positron-emitting radioactive nuclide with a short half-life (also called a radiotracer) is injected into the subject and image contrast arises from differences in the concentration of the radiotracer throughout the body. With appropriate corrections, it is possible to measure radiotracer concentration quantitatively. PET data can also provide information on the dynamics of radiotracer distribution over time. The main stages of PET image generation include acquiring coincidence emission data, histogramming data into sinogram representation, applying corrections, and reconstructing a map of activity concentration.

During the acquisition stage, the PET system collects data for millions of radioactive decays. Each positron emitted by an unstable nucleus begins with some kinetic energy and loses most of its energy in collisions before it undergoes an annihilation interaction with an electron. The average displacement from the original point of decay to the location of annihilation is called positron range and is typically on the order of one millimetre in tissue for the most common PET radioisotopes. In the most common case, when the positron-electron annihilation occurs, the total energy of both particles is transformed into two gamma rays (called annihilation photons) travelling in approximately opposite directions, each having energy 511 keV, equal to the rest mass energy of a positron or electron. In the centre of mass frame of reference, both annihilation photons travel in exactly opposite directions, ensuring momentum is conserved. Annihilation photons have high enough energy that many will pass through several centimetres of tissue without being scattered or absorbed.

The scintillation crystal in the PET detector is designed to have a high photon interaction cross-section and will stop a fraction of the annihilation photons. A photomultiplier tube or solid-state detector can detect the flash of light produced when an annihilation photon interacts with a scintillation crystal. When two photon detections occur on opposite sides of the scanner within a short window of time (in coincidence), it is likely that both photons originated from the same annihilation event and the PET system records the coordinates of the two crystal elements involved. The detector cannot distinguish coincident photons arising from a single annihilation pair from those that occur randomly; however, it is possible to estimate the random detection rate and correct for this effect.

The lines connecting each scintillation crystal pair in the detector are called lines of response (LOR). After acquiring millions of coincidence events, the data are sorted into a sinogram projection representation, where each element in the sinogram represents the total number of coincidences detected in a unique LOR. The LORs are ordered in the sinogram with respect to angle, distance to the centre of the field of view, and also tilt in the case of 3D imaging. Each LOR has a fixed width that depends on the detector geometry and the number of coincidences measured in a particular LOR depends on the total activity it contains. The detection efficiency in a particular LOR is the same regardless of the location of the activity along the LOR. The coincidence detection rate is also influenced by photon scattering and attenuation within the scanner bore as well as systematic differences in crystal detection efficiency. Various methods exist for correcting for these effects.

Data in the sinogram are then reconstructed to produce images showing the distribution of activity. A wide range of PET reconstruction algorithms have been implemented and these can be categorized as either analytic or iterative. The most commonly used analytic reconstruction technique is filtered back-projection (FBP), which uses an inverse Radon transform [1] and has the advantage of being computationally fast, but is deterministic and does not include information that may be known *a priori*. While FBP reconstructs images in two dimensional axial planes, analytic reconstruction approaches have been implemented in three dimensions [2]. Iterative reconstruction algorithms incorporate statistical information about the acquisition (such as positron range, photon pair non-collinearity, or detector response) to improve accuracy, minimize image artefacts and improve resolution. Iterative approaches require significantly greater computational resources when compared with analytic methods, and the resulting image depends on the choice of parameters and the number of iterations. The methods in most widespread use include maximum likelihood expectation maximization (MLEM) [3], ordered subsets expectation maximization (OSEM) [4] and maximum *a posteriori* (MAP) [5]. A detailed review of iterative reconstruction algorithms is given by Qi and Leahy [6].

Detector operation and corrections to PET data will be discussed later in this work; however, a comprehensive review of PET physics and instrumentation is given by Cherry, *et al.* [7].

The strength of PET lies in the broad variety of biologically relevant molecules that have been made into radiotracers, providing a range of molecularly specific targeted contrast possibilities [8]. The most widely used radiotracer is ^{18}F -

fluorodeoxyglucose ($[^{18}\text{F}]\text{FDG}$), a glucose analogue, which is used to study cellular metabolism and has important applications in oncology and neuroscience. There are other radiotracers based on molecules used in the normal functioning of the body, such as oxygen or water. Radiotracers can also be designed to bind to specific receptors and can be used for cell tracking and proliferation [9].

1.1.2 Principles of MRI

The image contrast mechanisms offered by MRI are also wide-ranging but provide different information than PET. MRI sequences can be designed to produce contrast involving magnetic relaxation properties, spectroscopy, flow, diffusion, perfusion, and functional information. Contrast agents offer further possibilities for imaging the physiological properties of blood vessels and tissue structures. MRI contrast mechanisms arise from fundamentally different physics processes than PET contrast. In brief, MRI probes the magnetic relaxation properties of tissues in spatially separated voxels that span the field of view. In conventional MRI, a strong, stable and homogeneous magnetic field polarizes the hydrogen nuclei in tissue to produce a bulk magnetization. Radiofrequency (RF) magnetic pulses are used to perturb the tissue magnetization and RF pickup coils sense the time-varying properties of the response. To form images, gradient magnetic fields oriented in each direction are used to encode spatial information. A detailed treatment of MR physics, MRI pulse sequences, and image formation is outside the scope of this work, but many well-written texts are available [10,11].

1.1.3 The Complementary Roles of PET and MRI

PET and MRI provide complementary information: PET offers the ability to probe tissue function and pharmacokinetics, while MRI can image morphologic structures with high resolution and contrast, and investigate the microscopic tissue environment. There are benefits that come from the combination of the two modalities in neurological applications, cardiac studies and tumour imaging [12,13]. Combining PET with MRI is attractive for scientific and clinical diagnostic applications. PET images generally show little or no anatomical structure and the ability to resolve features in PET images is limited by the fundamental physics processes of positron travel and the non-collinearity of annihilation photons, and these effects cannot be overcome completely with corrections or better detection hardware [14-16]. High spatial resolution MRI images can be co-registered and overlaid to provide an anatomical reference for low-resolution PET hotspots. Unlike other anatomical imaging modalities such as x-ray computed tomography (CT), MRI offers the possibility of excellent soft tissue contrast. Modest improvements in positron range effects are possible for fully simultaneous PET-MRI systems where a strong magnetic field is present during PET acquisition [17]. Another benefit for simultaneous or interleaved PET-MRI is the potential to use MR data to provide motion correction for PET acquisitions, with the potential to significantly reduce PET image blurring when imaging the abdomen [18,19].

1.2 Technical Challenges for Combining PET with MRI

PET and MRI have developed and matured independently over the past several decades. Until very recently, PET systems have not been designed with

consideration given to restrictions imposed by the MRI environment. With the exception of some purpose-built systems, such as the one described in Chapter 4, MRI scanners have likewise not been designed with PET compatibility in mind. Before the development of specialized PET-MRI systems, conventional PET scanners had gamma ray detectors based on well-characterized photomultiplier tube (PMT) technology and straightforward schemes of attenuation correction based on CT or transmission sources. The trend in MRI system design for both human and small animal scanners has been towards higher main magnetic field strengths, stronger and more compact gradient coils, and higher channel number RF coils having many discrete elements. These aspects of conventional PET and MRI system design must be carefully considered and potentially redesigned to accommodate the additional constraints that arise from combining the two modalities.

1.2.1 Sensitivity of PET Detectors to the MRI Environment

All PET detection systems must capture 511 keV photons efficiently and output corresponding electrical signals rapidly to an event processing system. Conventional PET detectors use PMTs to convert scintillation light into electrical pulses. PMTs operate by accelerating electrons along defined trajectories. Exposure to magnetic field can affect PMT operation because the electrons experience Lorentz forces that alter their path. For very weak fields, changes to electron trajectories internal to PMTs are insignificant and do not result in changes to PMT performance. For strong fields, such as those associated with MRI systems, PMTs can experience significant reductions in count-rate and systems for

position determination may not function properly. A more detailed treatment of this topic is given in Chapter 2.

Any implementation of combined PET-MRI using PMT-based detectors must ensure that the detectors do not experience strong magnetic fields. This can be achieved by placing the PMTs in a location with low magnetic field or using dynamically controlled magnetic fields to ensure the magnetic field is weak during PET acquisition. For tightly integrated PET-MRI systems, including those that can acquire PET and MRI data simultaneously, PET detectors must be redesigned to use either magnetic field insensitive light detectors, such as linear-mode avalanche photodiodes (APD) or Geiger-mode APDs, known as silicon photomultipliers (SiPM), or long optical fibres to carry scintillation light to PMTs placed in a low-field location. In simultaneous PET-MRI systems, it is also necessary to add metal shielding to the detector housing to minimize electromagnetic interactions of the gradient and RF fields on the PET detector electronics [20-24]. PET detection systems are described further in Section 1.4 of this chapter.

1.2.2 Attenuation Correction of PET Data

Gamma rays released during positron annihilation may undergo interactions with tissue or other material as they travel from the point of generation to the detector, along the line of response between two detector elements. For PET, interactions are typically either photoelectric absorption or Compton scattering, both of which result in fewer annihilation photons reaching the correct detector pair than would be the case without attenuating material. Each line of response has a different attenuation profile that depends on the geometry of the detection system and the

material inside the scanner bore. PET data can be corrected to compensate for the scattered and absorbed photons by measuring or estimating the probability of attenuation along each line of response. In conventional PET systems, attenuation correction is typically done by direct measurement of attenuation probabilities along lines of response, either through a separate CT image [25] or by rotating a transmission source around the subject [26]. These approaches capture all attenuating material within the PET imaging bore. A more detailed introduction on the physics of attenuation and scattering in the context of PET and methods of correcting for these effects can be found in Chapter 6.

PET-MRI systems that have PET detectors integrated with the MRI system use MR data to estimate attenuation correction factors for each line of response. MR-based attenuation correction methods have several limitations. MR images show only tissue inside the RF coil, and other attenuating material such as the RF coil and the bed must be included in the correction. To overcome this, CT data for the RF coil and bed can be combined with the MR-based attenuation map. This can be problematic if flexible RF coils are used; however, using MRI-visible markers in the flexible RF coil, an attenuation map can be estimated using a non-rigid transformation of a prior CT scan [27]. In cases where tissues lie outside of the MRI field of view (i.e. the arms when imaging the abdomen) attenuation estimates based on PET images can be used [28] or specialized MR sequences can be used to extend the MR field of view [29]. Another limitation is that MR sequences cannot measure attenuation properties directly (atomic electron structure and density); however, MR-based attenuation maps can be estimated using tissue segmentation, atlas-based approaches, or methods that use MR data with

uncorrected PET emission data. Detailed reviews of current MR-based attenuation correction methods are given by Bezrukov, *et al.* [30] and Wagenknecht, *et al.* [31].

1.2.3 Design Considerations for MR Hardware

For highly integrated PET-MRI approaches, MRI systems must be redesigned to accommodate the PET hardware. Some approaches have been a significant departure from conventional MRI design. One example of this is field-cycled MRI where a resistive electromagnet can be turned on or off in a matter of hundreds of milliseconds enabling the use of PMT-based PET detectors during the times the magnetic fields are off [32,33]. Other such approaches include split superconducting magnets where long optical fibres carry scintillation light out through a gap in the cryostat to PMT detectors placed in a region with low magnetic field [34] and PET-MRI systems based on permanent magnets [35,36]. Other methods have used conventional superconducting MR cryostats, but with the PET detectors inserted into an axial gap between sections of a split gradient coil [37,38]. PET inserts have been integrated with unmodified MRI scanners for small animal applications and human brain imaging at the cost of significant radial space within the MR bore [24]. For simultaneous PET-MRI approaches, consideration should be given to the design of RF coils, such as moving discrete components outside of the PET field of view and using different materials to improve photon attenuation and scatter characteristics. This topic is discussed in greater depth in Chapter 7.

1.3 Monte Carlo PET Simulation

Monte Carlo methods are useful for simulating systems that do not behave deterministically. A Monte Carlo simulation incorporates the fundamental statistical properties of the system modelled and samples the possible random outcomes with many repetitions. In this way, a Monte Carlo simulation can accurately model the general behaviour of a complicated system by using simple assumptions about the nature of its constituent parts.

In the context of PET physics, the statistical behaviour of the random processes of radioactive decay and photon interaction with matter are well understood. Therefore, Monte Carlo simulations are naturally suited for modelling PET systems. Monte Carlo PET emission simulations typically incorporate well-validated physics models for radioactive decay, positron travel, positron-electron annihilation, annihilation photon non-collinearity, photon-matter interactions, secondary particle generation, energy deposition by annihilation photons in scintillation crystal and the dynamic response of detection electronics. With modern computing capability, positron decays and the resulting interactions can be simulated efficiently for billions of decay events, matching the conditions typical in experimental acquisitions. Monte Carlo PET simulations are an appealing way of characterizing the performance of different detector geometries or phantom configurations without the need for experimentation. Furthermore, Monte Carlo PET simulations can provide insight into effects that are not possible to measure experimentally, such as scattering behaviour.

Several Monte Carlo simulation packages are in use in the high-energy physics and nuclear imaging communities; however, the GEANT4 toolkit (GEometry ANd Tracking) developed by CERN was the first to be coded in object-oriented C++, and is actively supported with a large user base [39,40]. Since the mid 2000s, several packages based on GEANT4 have been developed for tomographic emission simulation to add convenient features, such as detector digitization, and improve flexibility and ease of use. The most notable examples in active development are GATE (GEANT4 Application for Tomographic Emission) [41,42] and GAMOS (GEANT4-based Architecture for Medicine-Oriented Simulations) [43].

Third-party software is commonly used to process data and reconstruct images from Monte Carlo PET simulation output; however, this may introduce systematic errors between simulated and experimental images, which arise from differences in data processing algorithms. To reduce the possibility of such effects, simulated PET data can be converted to the raw data format of the physical scanner modelled so that both sets of data go through the same processing chain. This concept is discussed in further detail in Chapter 5. Furthermore, there is no standard way to produce attenuation correction sinograms for simulated PET data and many simulation studies omit attenuation and scatter corrections entirely. Without attenuation correction, quantitative activity measurements from PET images are inaccurate and the intensity may vary across the image. Chapter 6 introduces a novel method of generating attenuation sinograms quickly within GATE.

1.4 PET Detectors

A typical PET block detector consists of an array of scintillation crystal elements coupled optically to a light detector. When a gamma ray deposits most or all of its energy in one of the crystal elements, the resulting burst of light is detected in such a way that allows the identification of the crystal that was hit. Crystal elements can be made smaller to improve the localization of the gamma ray and increase image resolution down to the point where resolution is limited by the fundamental physics of positron range and photon non-collinearity [16,44]. Alternative detector designs based on monolithic scintillator crystals have also been studied [45]. The block detectors are set up in a ring geometry to form the PET detector. Photons detected by the scintillation detector trigger electrical pulses, which are used to produce a timing signal in the coincidence detection system. The PET electronics also reject pulses with heights that are below or above a certain range. By windowing the full energy peak, the detector can exclude some of the annihilation photons that have Compton scattered before reaching the detector, can reject multiple photons arriving in the same detector simultaneously, and can exclude some photons that scatter multiple times within the detector.

A variety of combinations of different scintillator materials have been implemented in PET systems to date. The qualities desirable in a PET scintillation crystal include high detection efficiency for 511 keV photons (high density and large interaction cross section), high light yield, fast rise times for coincidence detection, and fast decay times to reduce detector dead time [46]. The suitability of various scintillators for PET has been studied extensively [47-49]. The

scintillators in most widespread use in modern PET scanners include LSO ($\text{Lu}_2\text{SiO}_5\text{:Ce}$), LYSO ($(\text{Lu}_2\text{-Y})\text{SiO}_5\text{:Ce}$), GSO ($\text{Gd}_2\text{SiO}_5\text{:Ce}$), and the long-used BGO ($\text{Bi}_4\text{Ge}_3\text{O}_{12}$).

Until recently, scintillation light was typically detected with an array of 4 PMTs or with a position-sensitive PMT (PSPMT); however, solid-state light detectors, such as APDs or SiPMs, are being employed in an increasing variety of PET systems, especially in PET-MRI applications. Block detectors based on fractional light detection with 4 PMTs are discussed in detail in Chapter 4, and the operation of PSPMT-based detectors is described in Chapter 2. These types of detectors, which use the acceleration and multiplication of electrons to amplify signals, have been used for many years because of their high gain ($\sim 10^6$), fast recovery times, robustness, and well-characterized energy response. Figure 1.1 below shows the general operating principles of a PSPMT-based scintillation detector. For PET-MRI applications, the main shortcomings of PMT and PSPMT sensors are their high sensitivity to magnetic fields and large physical size. In contrast, APDs and SiPMs are highly compact and their performance is not significantly affected by strong magnetic fields.

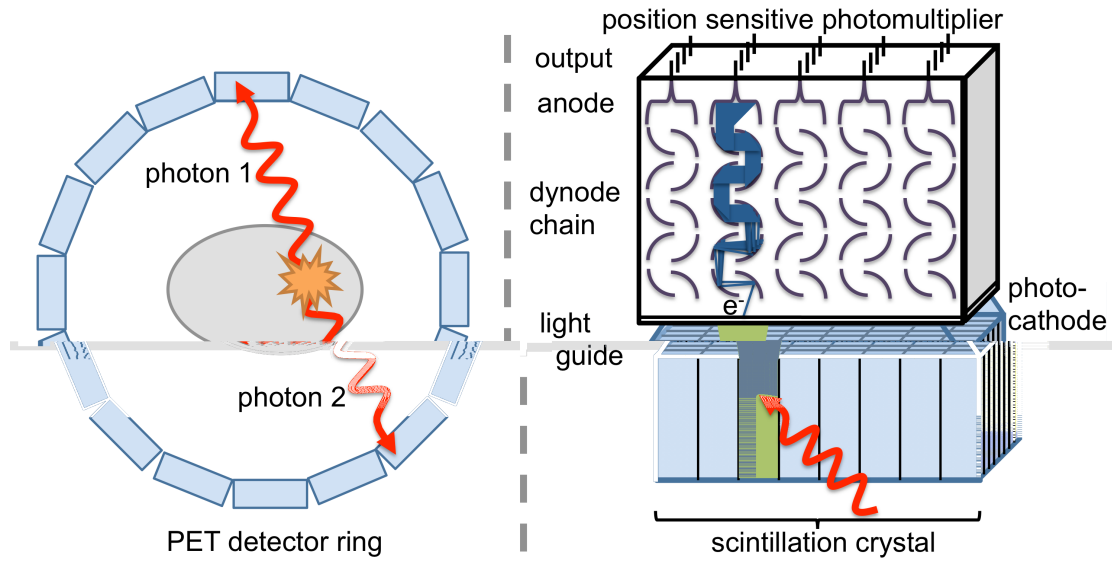


Figure 1.1: Schematic showing a PET detector ring (left) and a drawing of the operation of a PSPMT-based scintillation detector (right). A positron annihilation results in two photons, each of which can be detected by a single detector. If an annihilation photon is stopped by a scintillation crystal, a flash of light will appear in the scintillator, which causes electrons to be ejected from the photocathode within the photomultiplier detector. The initial electrons are accelerated through a dynode chain, with each successive dynode at a higher potential. At each dynode the number of electrons increases until the flood of electrons reach the final anode and cause a negative pulse in the anode output voltage signal. The voltage pulses from all the detectors are fed into the coincidence detection electronics.

Energetic electrons entering a semiconductor create electron-hole pairs due to impact ionization. For linear-mode APDs, a reverse bias voltage just below the breakdown voltage is applied to the semiconductor (typically 100-1500 V) and when a photoelectron creates electron-hole pairs this bias voltage results in avalanche breakdown [50]. APD gain typically ranges from 100-1000 and is sensitive to temperature. To improve the signal gain, an external low-noise preamplifier is required [51,52]. Like PMTs, the output pulse height of an APD is

proportional to the number of scintillation photons detected. APDs have high quantum efficiency [53] and their simple design makes them straightforward and relatively inexpensive to manufacture. SiPMs were designed to overcome the main shortcomings of linear-mode APDs: low gain and high bias voltage. A SiPM consists of a dense array of thousands of miniature APDs with each APD operated in Geiger-mode. In this mode, the reverse bias voltage is set slightly higher than the breakdown voltage and each APD element can detect a single photon. The result is that SiPMs only require bias voltages of 30-100 V and can achieve high gains comparable to those of PMTs ($\sim 10^5$ - 10^6) [54]. Due to their increased complexity, SiPMs are significantly more challenging to manufacture than APDs and, until recently, SiPMs were not available commercially in sufficient quantities and at low enough cost for widespread use in new PET systems. As costs decrease, SiPMs are expected to replace APDs as the photodetector of choice in combined PET-MRI applications and may also replace PMTs in standalone PET-CT systems.

1.5 Developments in Combined PET-MRI

Approaches to combining PET and MRI have been proposed and implemented as far back as the mid 1990s with the first small animal prototypes using long optical fibres to carry scintillation light to PMTs placed in a region of reduced magnetic field several metres from the MR system. The first such system was developed for a 0.2 T open geometry MRI at UCLA [55] and similar approaches were developed further by several groups throughout the next decade [35,56-59] including one with a split MRI geometry [60,61]. An alternative approach to PET-MRI using field-cycled MRI was proposed in 2006 by Handler, et al. [62]. In the

mid 2000s, APD-based PET inserts were developed first for preclinical applications [21,63-66] and then for human brain imaging [67]. Since the late 2000s, several designs for sequential human PET-MRI systems using a shared patient transport system have been demonstrated [68-70]. The first commercial preclinical PET-MRI system was introduced in 2011 by Mediso (Budapest, Hungary) and was based on a sequential coaxial geometry using a 1 T permanent magnet MRI. In the same year, Siemens (Knoxville, TN) introduced a whole-body human simultaneous PET-MRI system, which used an APD-based PET detector integrated into the bore of a 3 T MRI [38]. The development of hybrid systems based on SiPM detectors is currently an active area of research [71-73]. Detailed reviews of historical and current developments in PET-MRI have been published recently [74-76].

1.6 Thesis Overview

The central theme of this thesis is the investigation of how to combine PMT-based small-animal PET systems with MRI. This work focuses on characterization and mitigation of the effects a MRI scanner can have on PET systems of various architectures. MRI systems can affect PET in two primary ways: strong magnetic fields can interfere with the operation of PET detectors, and RF coil components introduce increased scattering and attenuation during PET acquisition. The experimental work and design studies described in Chapters 2 – 4 focus on how magnetic fields can affect PET systems, and investigates various approaches to overcome this obstacle. Specifically, in Chapter 2 the results of magnetic field exposure tests on a commercial stand-alone PET system are presented. These results are used to inform the studies described in Chapter 3, in which several

strategies for installation of a commercial PET system in the vicinity of an MRI system are investigated. In Chapter 4, the results of work to develop and evaluate a fully-integrated form of PET-MRI are presented and the first combined PET-MR images obtained with that system are shown. Chapters 5 and 6 lay the foundation for a sophisticated Monte Carlo PET simulation methodology, which is used in Chapter 7 to investigate how RF coils can affect PET image quality in fully-integrated PET-MR systems.

In Chapter 2, I characterize the performance of the PSPMT-based Siemens Inveon small animal PET system in the presence of an external magnetic field. My intention here was to investigate how this high-performance scanner could be combined in the same imaging facility with an MRI scanner. To do this it was necessary to establish magnetic field exposure limits on the scanner, which had not been done previously. I exposed the PET scanner to axial magnetic fields ranging from 0 – 3 mT using a large homogenous electromagnet built around the PET detector housing. I investigated a variety of PET performance metrics using a large homogenous cylinder source and a point source at different positions within the scanner bore. I determined that the effect of magnetic field on the performance of the Siemens Inveon PET was not significant up to 0.9 mT, and that imaging at 2 mT could not be recommended.

My contributions to the experiments described in Chapter 2 included the experimental design, the construction of the coil, and all data acquisition and analysis. I was also the lead author of the manuscript. Brian Dalrymple and Frank Van Sas machined the spindles on which the coil segments were wound. Andrew Boivin assisted with the coil winding and construction of the support structure.

In Chapter 3, I describe different approaches to setting up a PET-MRI facility using the Siemens Inveon PET scanner. The first approach I describe is an extension of the proof-of-principle PET and field-cycled MRI system for interleaved scanning. For the other approaches, the PET image would be acquired sequentially with the MRI image and the animal would be moved from one imaging region to the next between scans. I investigated the feasibility of the following approaches: constructing a new field-cycled MRI system with an axial gap large enough for the PET detectors, building a field-cycled MRI scanner with no axial gap and docking the PET system to the end of the MRI system, using a superconducting MRI scanner with an actively powered electromagnetic shield coil to reduce the fringe field at the PET detectors, and arranging the PET and MRI scanners in the same room separated by a certain distance.

I conducted all design studies described in this chapter. Chad Harris wrote the boundary element method code that I used to investigate different electromagnetic shielding options. Will Handler and Tim Scholl wrote the code I used to model the electromagnetic and thermal properties of the field-cycled MRI systems. Joe Gati provided the floor plans for the 9.4 T MRI suite.

In Chapter 4, I demonstrate a method of interleaved PET-MRI using field-cycled MRI with PMT-based PET detectors and I show the first multimodality images. In this experimental proof-of-principle demonstration, I inserted block PET detectors from a human scanner into an axial gap in the field-cycled MRI system and I imaged a multimodality phantom using an interleaved acquisition workflow of approximately 1 s PET and 1 s MRI. This demonstrated the feasibility of this approach to PET-MRI.

My contribution to this experiment involved the final system integration, writing code for PET data processing, and the complete experimental acquisition. I integrated the PET detectors into the axial gap of the MRI system and analysed their effect on magnetic field inhomogeneity. I determined that the increased inhomogeneity was unacceptable for MR imaging and I solved this problem by enhancing the field-cycled MRI system with additional second-order magnetic field shim coils, which I constructed. I designed and built an electronic system that provided dynamic interleaving control of the PET acquisition based on a blanking signal from the MRI console and I modified the MR pulse sequence to incorporate this control. Prior to the PET-MRI experiment, I calibrated the PET detectors, generated look up tables for flood histograms and implemented a normalization procedure. Following this, I designed and assembled the PET-MRI phantom and performed the experimental acquisition. I wrote all of the PET data processing and image reconstruction code and performed all of the analysis. I was the lead author of the manuscript reproduced in Chapter 4. Kyle Gilbert, Will Handler, Tim Scholl and Blaine Chronik designed and built the original field-cycled MRI system and wrote the original pulse sequences. Hao Peng and Will Handler assembled the PET detectors. Will Handler designed and set up the PET acquisition hardware and wrote software to record the raw data.

In Chapter 5, I present a Monte Carlo simulation architecture for the Siemens Inveon PET and compare simulated and experimental data for the NEMA NU 4-2008 image quality phantom. I describe the methodology of using the histogramming and reconstruction software of the Inveon scanner to process simulated data. The significance of this approach is that differences between

images from simulated data and those acquired on the physical scanner can be attributed to differences in the emission simulation and not to differences in sinogram production or image reconstruction algorithms. The details of the data processing code are given in the appendices.

In Chapter 6, I present a general add-on to the GATE Monte Carlo package for producing attenuation correction sinograms using the 511 keV attenuation coefficients in the emission simulation. I describe the benefits and limitations of this new approach and show the results of two validation tests. The add-on code is given in the appendices.

In Chapter 7, I use a Monte Carlo simulation to investigate the effect of different bed construction materials on the design of a small-animal holder compatible with both PET and MRI. Furthermore, I investigate the effects of photon attenuation and scattering for RF coil components present in the PET field of view through Monte Carlo simulation. I show that discrete coil components can have a significant effect on PET images even if they are included in attenuation correction. Further, the results indicated that even with RF coils designed to minimize photon attenuation, it is necessary to include the RF coil in the attenuation correction to achieve quantitative accuracy in PET images.

In these three chapters on Monte Carlo PET studies, I wrote all of the GATE macro code with the exception of the geometric specification of the Siemens Inveon PET detector, which I modified from a version obtained from Arda Konik. I wrote the following code, which is available in the appendices: a script to run GATE simulations on multiple CPUs simultaneously in batch mode, a program to

convert the GATE ROOT output files into Siemens list-mode format, and a general GATE add-on to produce attenuation correction sinograms. I designed and performed all simulations and experiments and analysed all of the data used in these chapters. For the experiment described in Chapter 5, Hamed Moazami filled the NEMA NU 4-2008 with ^{18}F -FDG and measured the activity in a well counter.

In Chapter 8, I conclude the thesis by summarizing the major findings and I suggest possible directions for future research.

The appendices include descriptions of important software algorithms developed during the course of this project and explain how they can be accessed and used. In Appendix A.1, I provide code for converting the data output from the PET emission simulation to the raw listmode data format used by the Siemens Inveon PET scanner. In Appendix A.2 I describe a simple script for running multiple instances of a GATE simulation simultaneously on multi-CPU computers. In Appendix A.3, I describe the GATE macro codes for the PET phantoms and sources used in the NEMA NU 4-2008 standard. In Appendix A.4, I describe the GATE attenuation correction add-on. The add-on is written in a general form that can be used on different scanner geometries without significant modification.

1.7 References

1. Brooks RA, Di Chiro G. Principles of computer assisted tomography (CAT) in radiographic and radioisotopic imaging. *Physics in Medicine and Biology* 1976;21(5):689-732.
2. Kinahan PE, Rogers JG. Analytic 3D image reconstruction using all detected events. *Nuclear Science, IEEE Transactions on* 1989;36(1):964-968.
3. Shepp LA, Vardi Y. Maximum likelihood reconstruction for emission tomography. *IEEE Transactions on Medical Imaging* 1982;1(2):113-122.
4. Hudson HM, Larkin RS. Accelerated image reconstruction using ordered subsets of projection data. *IEEE Transactions on Medical Imaging* 1994;13(4):601-609.
5. Fessler JA. Mean and variance of implicitly defined biased estimators (such as penalized maximum likelihood): applications to tomography. *IEEE Trans Image Process* 1996;5(3):493-506.
6. Qi J, Leahy RM. Iterative reconstruction techniques in emission computed tomography. *Physics in Medicine and Biology* 2006;51(15):R541-578.
7. Cherry SR, Dahlbom M, Phelps ME, SpringerLink (Online service). *PET Physics, Instrumentation, and Scanners*. New York, NY: Springer Science+Business Media, LLC; 2006.
8. Wester HJ. Nuclear imaging probes: from bench to bedside. *Clinical Cancer Research* 2007;13(12):3470-3481.
9. Been LB, Suurmeijer AJ, Cobben DC, Jager PL, Hoekstra HJ, Elsinga PH. [18F]FLT-PET in oncology: current status and opportunities. *European Journal of Nuclear Medicine and Molecular Imaging* 2004;31(12):1659-1672.
10. Haacke EM. *Magnetic resonance imaging : physical principles and sequence design*. New York: J. Wiley-Liss; 1999. xxvii, 914 p. p.
11. McRobbie DW. *MRI from picture to proton*. Cambridge, UK ; New York: Cambridge University Press; 2007. xii, 394 p. p.
12. Wehrl HF, Sauter AW, Judenhofer MS, Pichler BJ. Combined PET/MR imaging--technology and applications. *Technology in Cancer Research and Treatment* 2010;9(1):5-20.

13. Judenhofer MS, Cherry SR. Applications for preclinical PET/MRI. *Seminars in Nuclear Medicine* 2013;43(1):19-29.
14. Sanchez-Crespo A, Larsson SA. The influence of photon depth of interaction and non-collinear spread of annihilation photons on PET image spatial resolution. *European Journal of Nuclear Medicine and Molecular Imaging* 2006;33(8):940-947.
15. Sanchez-Crespo A, Andreo P, Larsson SA. Positron flight in human tissues and its influence on PET image spatial resolution. *European Journal of Nuclear Medicine and Molecular Imaging* 2004;31(1):44-51.
16. Levin CS, Hoffman EJ. Calculation of positron range and its effect on the fundamental limit of positron emission tomography system spatial resolution. *Physics in Medicine and Biology* 1999;44(3):781-799.
17. Raylman RR, Hammer BE, Christensen NL. Combined MRI-PET scanner: a Monte Carlo evaluation of the improvements in PET resolution due to the effects of a static homogeneous magnetic field. *Nuclear Science, IEEE Transactions on* 1996;43(4):2406-2412.
18. Catana C, Benner T, van der Kouwe A, Byars L, Hamm M, Chonde DB, Michel CJ, El Fakhri G, Schmand M, Sorensen G. MRI-Assisted PET Motion Correction for Neurologic Studies in an Integrated MR-PET Scanner. *Journal of Nuclear Medicine* 2011;52(1):154-161.
19. Chun SY, Reese TG, Ouyang JS, Guerin B, Catana C, Zhu XP, Alpert NM, El Fakhri G. MRI-Based Nonrigid Motion Correction in Simultaneous PET/MRI. *Journal of Nuclear Medicine* 2012;53(8):1284-1291.
20. Maramraju SH, Smith SD, Rescia S, Stoll S, Budassi M, Vaska P, Woody C, Schlyer D. Electromagnetic Interactions in a Shielded PET/MRI System for Simultaneous PET/MR Imaging in 9.4 T: Evaluation and Results. *IEEE Transactions on Nuclear Science* 2012;59(5):1892-1899.
21. Pichler BJ, Judenhofer MS, Catana C, Walton JH, Kneilling M, Nutt RE, Siegel SB, Claussen CD, Cherry SR. Performance test of an LSO-APD detector in a 7-T MRI scanner for simultaneous PET/MRI. *Journal of Nuclear Medicine* 2006;47(4):639-647.
22. Judenhofer MS, Wehrli HF, Newport DF, Catana C, Siegel SB, Becker M, Thielscher A, Kneilling M, Lichy MP, Eichner M *and others*. Simultaneous PET-MRI: a new approach for functional and morphological imaging. *Nature Medicine* 2008;14(4):459-465.

23. Peng BJ, Walton JH, Cherry SR, Willig-Onwuachi J. Studies of the interactions of an MRI system with the shielding in a combined PET/MRI scanner. *Physics in Medicine and Biology* 2010;55(1):265-280.
24. Wehrl HF, Judenhofer MS, Thielscher A, Martirosian P, Schick F, Pichler BJ. Assessment of MR Compatibility of a PET Insert Developed for Simultaneous Multiparametric PET/MR Imaging on an Animal System Operating at 7 T. *Magnetic Resonance in Medicine* 2011;65(1):269-279.
25. Carney JP, Townsend DW, Rappoport V, Bendriem B. Method for transforming CT images for attenuation correction in PET/CT imaging. *Medical Physics* 2006;33(4):976-983.
26. deKemp RA, Nahmias C. Attenuation correction in PET using single photon transmission measurement. *Medical Physics* 1994;21(6):771-778.
27. Paulus DH, Braun H, Aklan B, Quick HH. Simultaneous PET/MR imaging: MR-based attenuation correction of local radiofrequency surface coils. *Medical Physics* 2012;39(7):4306-4315.
28. Nuyts J, Bal G, Kehren F, Fenchel M, Michel C, Watson C. Completion of a truncated attenuation image from the attenuated PET emission data. *IEEE Transactions on Medical Imaging* 2013;32(2):237-246.
29. Blumhagen JO, Ladebeck R, Fenchel M, Scheffler K. MR-based field-of-view extension in MR/PET: B(0) homogenization using gradient enhancement (HUGE). *Magnetic Resonance in Medicine* 2012.
30. Bezrukov I, Mantlik F, Schmidt H, Scholkopf B, Pichler BJ. MR-Based PET attenuation correction for PET/MR imaging. *Seminars in Nuclear Medicine* 2013;43(1):45-59.
31. Wagenknecht G, Kaiser HJ, Mottaghy FM, Herzog H. MRI for attenuation correction in PET: methods and challenges. *Magnetic Resonance Materials in Physics Biology and Medicine* 2013;26(1):99-113.
32. Bindseil GA, Gilbert KM, Scholl TJ, Handler WB, Chronik BA. First Image From a Combined Positron Emission Tomography and Field-Cycled MRI System. *Magnetic Resonance in Medicine* 2011;66(1):301-305.
33. Gilbert KM, Scholl TJ, Handler WB, Alford JK, Chronik BA. Evaluation of a Positron Emission Tomography (PET)-Compatible Field-Cycled MRI (FCMRI) Scanner. *Magnetic Resonance in Medicine* 2009;62(4):1017-1025.

34. Poole M, Bowtell R, Green D, Pittard S, Lucas A, Hawkes R, Carpenter A. Split Gradient Coils for Simultaneous PET-MRI. *Magnetic Resonance in Medicine* 2009;62(5):1106-1111.
35. Yamamoto S, Imaizumi M, Kanai Y, Tatsumi M, Aoki M, Sugiyama E, Kawakami M, Shimosegawa E, Hatazawa J. Design and performance from an integrated PET/MRI system for small animals. *Annals of Nuclear Medicine* 2010;24(2):89-98.
36. Yamamoto S, Watabe H, Kanai Y, Aoki M, Sugiyama E, Watabe T, Imaizumi M, Shimosegawa E, Hatazawa J. Interference between PET and MRI sub-systems in a silicon-photomultiplier-based PET/MRI system. *Physics in Medicine and Biology* 2011;56(13):4147-4159.
37. Delso G, Ziegler S. Pet/Mri System Design. *European Journal of Nuclear Medicine and Molecular Imaging* 2009;36:86-92.
38. Delso G, Furst S, Jakoby B, Ladebeck R, Ganter C, Nekolla SG, Schwaiger M, Ziegler SI. Performance Measurements of the Siemens mMR Integrated Whole-Body PET/MR Scanner. *Journal of Nuclear Medicine* 2011;52(12):1914-1922.
39. Agostinelli S, Allison J, Amako K, Apostolakis J, Araujo H, Arce P, Asai M, Axen D, Banerjee S, Barrand G *and others*. Geant4—a simulation toolkit. *Nuclear Instruments and Methods in Physics Research Section A: Accelerators, Spectrometers, Detectors and Associated Equipment* 2003;506(3):250-303.
40. Allison J, Amako K, Apostolakis J, Araujo H, Dubois PA, Asai M, Barrand G, Capra R, Chauvie S, Chytrcek R *and others*. Geant4 developments and applications. *Nuclear Science, IEEE Transactions on* 2006;53(1):270-278.
41. Jan S, Santin G, Strul D, Staelens S, Assie K, Autret D, Avner S, Barbier R, Bardies M, Bloomfield PM *and others*. GATE: a simulation toolkit for PET and SPECT. *Physics in Medicine and Biology* 2004;49(19):4543-4561.
42. Jan S, Benoit D, Becheva E, Carlier T, Cassol F, Descourt P, Frisson T, Grevillot L, Guigues L, Maigne L *and others*. GATE V6: a major enhancement of the GATE simulation platform enabling modelling of CT and radiotherapy. *Physics in Medicine and Biology* 2011;56(4):881-901.
43. Arce P, Lagares JJ, Harkness L, Desorgher L, de Lorenzo G, Abreu Y, Zhentian W. GAMOS: An easy and flexible way to use GEANT4. 2011 23-29 Oct. 2011. p 2230-2237.

44. Stickel JR, Cherry SR. High-resolution PET detector design: modelling components of intrinsic spatial resolution. *Physics in Medicine and Biology* 2005;50(2):179-195.
45. Seifert S, van Dam HT, Huizenga J, Vinke R, Dendooven P, Lohner H, Schaart DR. Monolithic LaBr₃:Ce crystals on silicon photomultiplier arrays for time-of-flight positron emission tomography. *Physics in Medicine and Biology* 2012;57(8):2219-2233.
46. Melcher CL. Scintillation crystals for PET. *Journal of Nuclear Medicine* 2000;41(6):1051-1055.
47. Moses WW. Recent advances and future advances in time-of-flight PET. *Nuclear Instruments & Methods in Physics Research Section a-Accelerators Spectrometers Detectors and Associated Equipment* 2007;580(2):919-924.
48. Nassalski A, Kapusta M, Batsch T, Wolski D, Mockel D, Enghardt W, Moszynski M. Comparative study of scintillators for PET/CT detectors. *IEEE Transactions on Nuclear Science* 2007;54(1):3-10.
49. Korzhik M, Fedorov A, Annenkov A, Borissevitch A, Dossovitski A, Missevitch O, Lecoq P. Development of scintillation materials for PET scanners. *Nuclear Instruments & Methods in Physics Research Section a-Accelerators Spectrometers Detectors and Associated Equipment* 2007;571(1-2):122-125.
50. McKay KG. Avalanche Breakdown in Silicon. *Physical Review* 1954;94(4):877-884.
51. Binkley DM, Puckett BS, Casey ME, Lecomte R, Saoudi A. A power-efficient, low-noise, wideband, integrated CMOS preamplifier for LSO/APD PET systems. *IEEE Transactions on Nuclear Science* 2000;47(3):810-817.
52. Lecomte R, Pepin CM, Lepage MD, Pratte JF, Dautet H, Binkley DM. Performance analysis of phoswich/APD detectors and low-noise CMOS preamplifiers for high-resolution PET systems. *IEEE Transactions on Nuclear Science* 2001;48(3):650-655.
53. McClish M, Farrell R, Vanderpuye K, Shah KS. A reexamination of silicon avalanche photodiode gain and quantum efficiency. 2005 IEEE Nuclear Science Symposium Conference Record, Vols 1-5 2005:2959-2962.
54. Kolb A, Lorenz E, Judenhofer MS, Renker D, Lankes K, Pichler BJ. Evaluation of Geiger-mode APDs for PET block detector designs. *Physics in Medicine and Biology* 2010;55(7):1815-1832.

55. Shao YP, Cherry SR, Farahani K, Meadors K, Siegel S, Silverman RW, Marsden PK. Simultaneous PET and MR imaging. *Physics in Medicine and Biology* 1997;42(10):1965-1970.
56. Mackewn J, Strul D, Hallett W, Halsted P, Page R, Keevil S, Williams S, Cherry S, Marsden P. Design and development of an MR-compatible PET scanner for imaging small animals. *IEEE Transactions on Nuclear Science* 2005;52(5 Part 1):1376-1380.
57. Mackewn JE, Halsted P, Charles-Edwards G, Page R, Totman JJ, Sunassee K, Strul D, Hallett WA, Jauregui-Osoro M, Liepins P *and others*. Performance Evaluation of an MRI-Compatible Pre-Clinical PET System Using Long Optical Fibers. *IEEE Transactions on Nuclear Science* 2010;57(3):1052-1062.
58. Raylman RR, Majewski S, Lemieux SK, Velan SS, Kross B, Popov V, Smith MF, Weisenberger AG, Zorn C, Marano GD. Simultaneous MRI and PET imaging of a rat brain. *Physics in Medicine and Biology* 2006;51(24):6371-6379.
59. Yamamoto S, Hatazawa J, Imaizumi M, Shimosegawa E, Aoki M, Sugiyama E, Kawakami M, Takamatsu S, Minato K, Matsumoto K *and others*. A Multi-Slice Dual Layer MR-Compatible Animal PET System. *IEEE Transactions on Nuclear Science* 2009;56(5):2706-2713.
60. Lucas AJ, Hawkes RC, Ansorge RE, Williams GB, Nutt RE, Clark JC, Fryer TD, Carpenter TA. Development of a combined microPET-MR system. *Technology in Cancer Research and Treatment* 2006;5(4):337-341.
61. Hawkes RC, Fryer TD, Siegel S, Ansorge RE, Carpenter TA. Preliminary Evaluation of a Combined MicroPET (R)-MR System. *Technology in Cancer Research and Treatment* 2010;9(1):53-60.
62. Handler WB, Gilbert KM, Peng H, Chronik BA. Simulation of scattering and attenuation of 511 keV photons in a combined PET/field-cycled MRI system. *Physics in Medicine and Biology* 2006;51(10):2479-2491.
63. Catana C, Wu YB, Judenhofer MS, Qi JY, Pichler BJ, Cherry SR. Simultaneous acquisition of multislice PET and MR images: Initial results with a MR-compatible PET scanner. *Journal of Nuclear Medicine* 2006;47(12):1968-1976.
64. Judenhofer MS, Catana C, Swann BK, Siegel SB, Jung W-I, Nutt RE, Cherry SR, Claussen CD, Pichler BJ. PET/MR Images Acquired with a Compact MR-compatible PET Detector in a 7-T Magnet. *Radiology* 2007;244(3):807-814.

65. Woody C, Schlyer D, Vaska P, Tomasi D, Solis-Najera S, Rooney W, Pratte JF, Junnarkar S, Stoll S, Master Z *and others*. Preliminary studies of a simultaneous PET/MRI scanner based on the RatCAP small animal tomograph. *Nucl Instrum Methods Phys Res Sect A* 2007;571(1-2):102-105.
66. Maramraju SH, Smith SD, Junnarkar SS, Schulz D, Stoll S, Ravindranath B, Purschke ML, Rescia S, Southekal S, Pratte JF *and others*. Small animal simultaneous PET/MRI: initial experiences in a 9.4 T microMRI. *Physics in Medicine and Biology* 2011;56(8):2459-2480.
67. Schlemmer HPW, Pichler BJ, Schmand M, Burbar Z, Michel C, Ladebeck R, Jattke K, Townsend D, Nahmias C, Jacob PK *and others*. Simultaneous MR/PET imaging of the human brain: Feasibility study. *Radiology* 2008;248(3):1028-1035.
68. Cho ZH, Son YD, Kim HK, Kim KN, Oh SH, Han JY, Hong IK, Kim YB. A hybrid PET-MRI: An integrated molecular-genetic imaging system with HRRT-PET and 7.0-T MRI. *International Journal of Imaging Systems and Technology* 2007;17(4):252-265.
69. Zaidi H, Ojha N, Morich M, Griesmer J, Hu Z, Maniawski P, Ratib O, Izquierdo-Garcia D, Fayad ZA, Shao L. Design and performance evaluation of a whole-body Ingenuity TF PET-MRI system. *Physics in Medicine and Biology* 2011;56(10):3091-3106.
70. Veit-Haibach P, Kuhn FP, Wiesinger F, Delso G, von Schulthess G. PET-MR imaging using a tri-modality PET/CT-MR system with a dedicated shuttle in clinical routine. *Magnetic Resonance Materials in Physics Biology and Medicine* 2013;26(1):25-35.
71. Schulz V, Weissler B, Gebhardt P, Solf T, Lerche CW, Fischer P, Ritzert M, Mlotok V, Piemonte C, Goldschmidt B *and others*. SiPM based preclinical PET/MR Insert for a human 3T MR: first imaging experiments. 2011 Ieee Nuclear Science Symposium and Medical Imaging Conference (Nss/Mic) 2011:4467-4469.
72. Yoon HS, Ko GB, Il Kwon S, Lee CM, Ito M, Song IC, Lee DS, Hong SJ, Lee JS. Initial Results of Simultaneous PET/MRI Experiments with an MRI-Compatible Silicon Photomultiplier PET Scanner. *Journal of Nuclear Medicine* 2012;53(4):608-614.
73. Yamamoto S, Watabe T, Watabe H, Aoki M, Sugiyama E, Imaizumi M, Kanai Y, Shimosegawa E, Hatazawa J. Simultaneous imaging using Si-PM-

based PET and MRI for development of an integrated PET/MRI system. *Physics in Medicine and Biology* 2012;57(2):N1-N13.

74. Herzog H. PET/MRI: Challenges, solutions and perspectives. *Z Med Phys* 2012;22(4):281-298.
75. Wehrli HF, Judenhofer MS, Wiehr S, Pichler BJ. Pre-clinical PET/MR: technological advances and new perspectives in biomedical research. *European Journal of Nuclear Medicine and Molecular Imaging* 2009;36 Suppl 1:S56-68.
76. Vaska P, Cao TY. The State of Instrumentation for Combined Positron Emission Tomography and Magnetic Resonance Imaging. *Seminars in Nuclear Medicine* 2013;43(1):11-18.

Chapter 2

2 Magnetic field exposure tests on a Siemens Inveon small animal PET system¹

When siting a photomultiplier tube (PMT)-based small-animal PET scanner near an MRI system, it is important to investigate how PET performance is affected by external magnetic field and determine the field limit below which performance is not degraded. In this study, an electromagnet was used to expose a Siemens Inveon PET scanner to axial magnetic fields of various strengths. Most investigated metrics suggested that the PMT-based PET system tested could withstand fields up to 0.9 mT without significant effects.

2.1 Introduction

There has been significant interest in the development of small animal imaging systems that permit the simultaneous or sequential acquisition of positron emission tomography (PET) data and magnetic resonance (MR) images. Over the past decade, several independent groups have developed working prototypes of MR-compatible small animal PET inserts or optical light guide arrangements that have been shown to acquire PET and MR data simultaneously [1-7]. In addition to its relevance in preclinical research, combined PET-MRI is becoming increasingly important in neuroscience and oncology.

¹ A manuscript based on the contents of this chapter was in preparation at the time of thesis publication.

One option for imaging facilities without access to specialized simultaneous PET-MRI hardware is to implement a time sequential approach whereby standalone PET and MRI systems are used. In fact, with two separate scanners, there are many advantages to having both placed in proximity: a single bed can be used for both scans keeping the animal fixed in position, the animal can remain connected to heating and gas anaesthetic between modalities and all radioactivity remains confined to one room. Importantly, conducting both scans immediately in succession with the same bed would also enable the use of an *a priori* rigid body transformation matrix for the co-registration of PET and MR image data and would allow for studies to be performed that use both the functional information from PET, and the anatomical information from MRI.

PET systems typically employ photomultiplier tube (PMT)-based detectors, which are sensitive to magnetic fields. Specialized MRI scanners with negligible fringe magnetic field can be positioned near PET scanners without concern [8]. If a PET system were positioned too close to a high-field conventional MRI system, the stronger fringe field would affect PET system performance. When designing a time sequential PET-MRI facility with a conventional MRI scanner, it is important to balance the desire for proximity with the need to avoid reducing PET performance. Therefore, it is necessary to determine limits for magnetic field exposure or in other words, determine how closely the two scanners can be positioned. In this study, the authors investigated how the performance of a small animal PET system in widespread use, the Siemens Inveon Dedicated PET (Siemens Medical Solutions), was affected by external magnetic fields of various

strengths, to guide the placement of the Inveon system with respect to pre-existing MRI scanners.

2.2 Materials and Methods

2.2.1 PET System Description

The Siemens Inveon Dedicated PET detector consists of a ring of 16 PET modules; with each module having a row of four lutetium oxyorthosilicate (LSO) crystal blocks (1.59x1.59x10 mm crystals in each 20x20 block) coupled to four position-sensitive photomultiplier tubes (model R8900-C12; Hamamatsu Photonics). The PET system permits fast scanning due to its very high sensitivity (up to 10% at the centre of the field of view) and has a large axial field of view (12.7 cm) enabling whole-mouse imaging [9,10].

Each detector contains a scintillator crystal array connected to a smaller-area photomultiplier tube via a tapered optical light guide [11]. The internal structure of the photomultiplier tube includes a grid of metal channel dynodes with the dynodes in each channel separated by a small distance to minimize crosstalk. After traveling through the light guide, optical scintillation photons hit the photocathode inside the photomultiplier tube. Electrons ejected from the photocathode are accelerated through a potential difference and directed onto one of the dynode channels using a focusing mesh. Secondary electrons generated from the first dynode are accelerated towards the dynode directly beneath the first dynode. This process repeats until the electrons hit a single large dynode and the subsequent photoelectrons reflect back to hit the cross-plate anode, which is arranged in two intersecting layers and permits position determination [12].

Exposing the detector to an external magnetic field results in a deflection of the electron trajectory within the photomultiplier tube.

2.2.2 Magnetic Field Test Setup

A resistive electromagnet, built around the PET detector housing, as shown in Figure 2.1, was constructed to provide the magnetic field. The geometry and orientation of the magnet was chosen to produce a field with the same symmetry as the detector ring, such that each detector block, at the same axial position, experienced the same field profile. The device was designed to be as close as possible to a Helmholtz coil geometry given the constraints of the PET system dimensions and it consisted of two identical solenoids of 100 turns each with an average radius of 28.1 cm and a centre-to-centre separation of 34.6 cm. A DC power supply (Agilent 6032A) was used in constant current mode to control the strength of the magnetic field. The magnetic field in the bore was measured using a Hall effect field probe and these measurements were used to verify field values from a Biot-Savart Law computational model of the electromagnet. With a verified model it is possible to calculate the magnetic field within the detector blocks; the result shown in Figure 2.2 indicates that the field magnitude varies by approximately $\pm 3\%$ within the detectors with data from the computational model. This variation is not expected to have a significant effect on the results. All field values reported henceforth are the average magnitudes within the PMTs, unless otherwise stated.

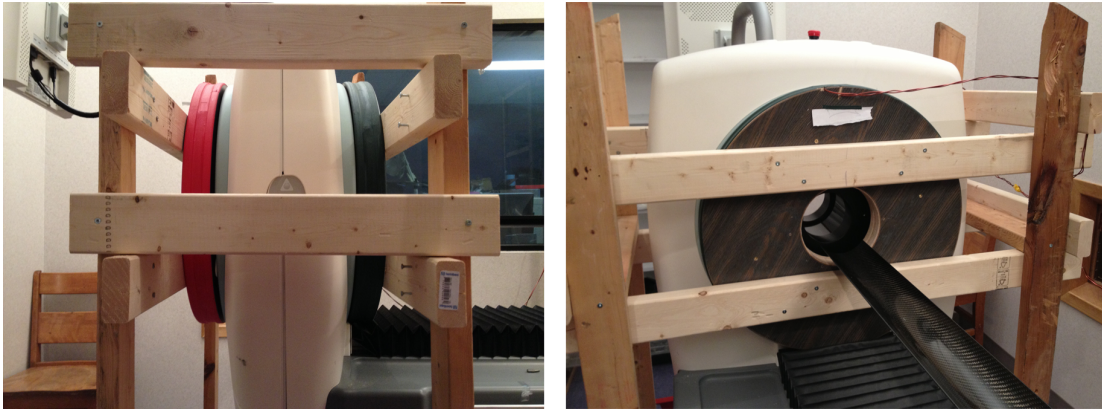


Figure 2.1: Photographs of the geometry of the experimental setup. The current through the electromagnet was varied to produce a range of magnetic field magnitudes through the PET detectors.

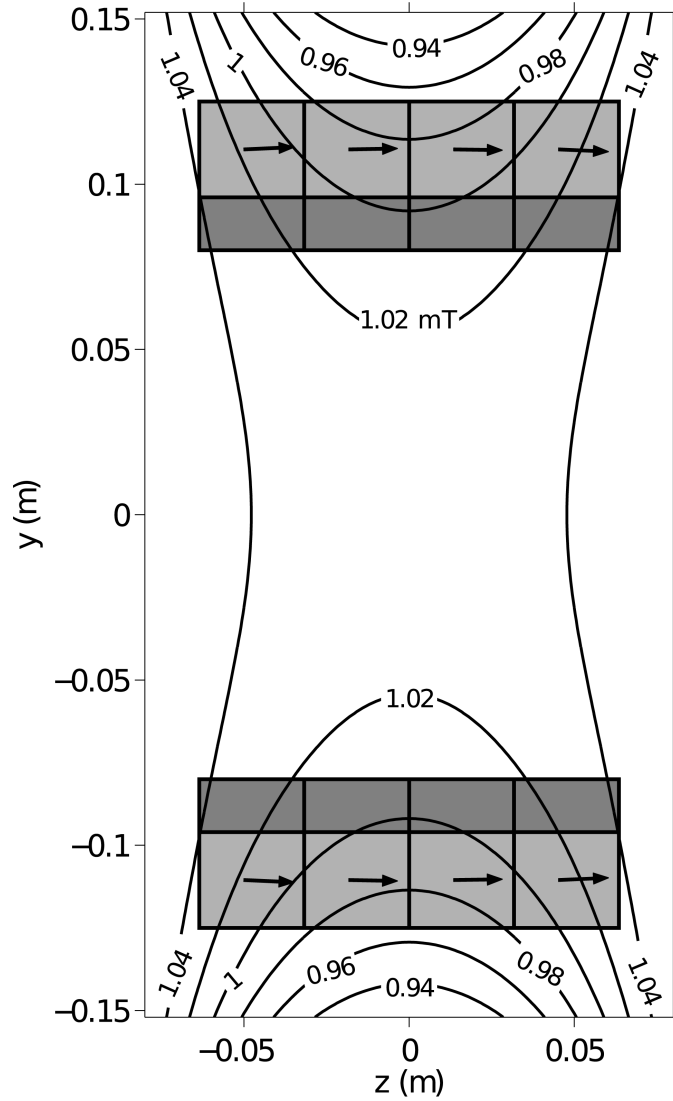


Figure 2.2: Simulated contour map of the magnetic field magnitude in the vicinity of the PET detectors. The dark and light grey boxes indicate the position and size of the scintillator crystal and position-sensitive photomultiplier tube, respectively. The arrows show the direction of the magnetic field within each photomultiplier tube. For illustration, contour values are shown for an applied current of 3.46 A producing an average field of 1 mT within the photomultiplier tubes.

2.2.3 Phantom Descriptions and Acquisition Parameters

Two sealed-source phantoms were used: A homogeneous cylinder source (Ge-68, 1.8 MBq, radius: 3 cm, length: 16 cm) was used to measure reconstructed activity, noise and image artifacts, and a point source (Na-22, 0.22 MBq, diameter: 0.25 mm, 1 cm³ plastic cube) was used to measure reconstructed positioning accuracy and resolution. Acquisitions were performed during the application of various sustained magnetic field strengths ranging from zero to 3.0 mT.

At each field value, a full detector setup was performed followed by a normalization scan (component-based, 3 billion counts) and a blank transmission scan (15 hours). The manufacturer recommends doing these calibrations at regular intervals as well as whenever the PET system is moved or serviced. Calibrating the crystal look up tables during the detector setup is necessary because magnetic fields stretch and skew the position profile.

The cylinder source was positioned at the centre and the acquisition workflow included a 60-minute transmission scan followed by a 45-minute emission scan. The point source was positioned at nine locations throughout the field of view and an 11-minute emission acquisition was collected for each position. For all acquisitions, the time and energy coincidence windows were 3.432 ns and 350-650 KeV, respectively.

2.2.4 Reconstruction Parameters and Analysis Methods

The data from each acquisition were reconstructed using a filtered back-projection algorithm (Inveon Acquisition Workplace 1.5; Siemens Medical Solutions) with the default parameters recommended by the manufacturer (128x128x159

resolution with voxel dimensions: (0.776383, 0.776383, 0.796) mm, projection filter: ramp, projection cut-off (nyquist): 0.5). The Ge-68 cylinder source images were reconstructed with attenuation correction. For the Na-22 point source acquisitions, the source and holder represented a relatively small amount of attenuating material and image reconstruction was performed without a transmission-based attenuation correction.

The Ge-68 Image analysis was performed using the manufacturer's software (Inveon Research Workplace 3.0; Siemens Medical Solutions) and point source resolution and positioning accuracy were computed using MATLAB (The MathWorks). For the cylinder source scans, the prompts rate was determined by source data in the sinogram header file. The mean reconstructed activity and image noise were investigated by measuring the percentage standard deviation (standard deviation divided by mean) of the voxel intensities in a cylindrical volume of interest spanning nearly the complete active volume (length: 12 cm, radius: 2.5 cm). A correction for the decay of Ge-68 between scans was applied. The average gantry temperature was recorded and the reconstructed activity values were scaled by the temperature dependence of the light yield of LSO detectors, $-0.2\%/^{\circ}\text{C}$, as reported by Mao, et al. [13]. Mean linear attenuation coefficients for the cylinder were measured from attenuation maps computed using transmission data to investigate how attenuation correction is affected by magnetic field. The uncertainty of the prompts rate was estimated by repeating the acquisition and analysis 20 times at zero field. The uncertainty of the reconstructed activity was estimated by a combination of repeated measurement

and the error associated with translating the volume of interest by one voxel along each direction.

Crystal efficiency maps and position profiles were also generated from the cylindrical source. Energy spectra could not be analysed directly because the manufacturer's software does not provide access to the raw spectrum data; however, we report the energy resolution and photopeak energy bin computed during detector setup for selected crystals in a representative detector. For these same crystals, screen captures of the emission and transmission energy spectra are shown for various magnetic field strengths. The magnetic field dependence of the timing resolution is analysed for the same detector.

For the point source, resolution was measured in the radial (x), tangential (y) and axial (z) directions by computing the full width at half maximum (FWHM) according to the method described in the NEMA NU 4-2008 standards document [14]. For each direction, a profile through the peak was produced, then the maximum was determined by fitting a parabola to the three data points closest to the peak, and finally the width at half maximum was computed by linear interpolation. The coordinates of the point source were determined by the locations of the maxima from the parabolic fits. Uncertainties associated with the coordinates and resolutions were estimated by repeating the acquisition and analysis 10 times at zero field, removing and replacing the point source between each repetition.

2.3 Results

2.3.1 Count Rate and Attenuation Coefficient

The prompts rate and reconstructed activity for data collected with the magnetic field present are shown in Figure 2.3(a) as a function of applied magnetic field (normalized to 1 at zero field). As the magnetic field increased, the prompts rate did not change significantly up to 0.9 mT. The reconstructed activity in the volume of interest tended to decrease as the field increased, consistent with the decrease in the mean attenuation coefficient seen in Figure 2.3(b). The measured attenuation coefficient decreased by 3% between zero field and 2.0 mT. When the reconstructed activity values were scaled to account for differences in measured attenuation coefficient from the zero field case, the reconstructed activity appeared to more closely match the prompts rate behaviour as a function of field. The decrease in measured attenuation coefficient with increasing field strength can be explained by the effect of Compton scattered transmission photons, as discussed later in this chapter. Artifacts were not apparent in reconstructed images of the cylinder source up to 2.0 mT, as seen in Figure 2.3(c). The average percentage standard deviation image noise was 39.7% and the variation in this value was ± 0.2 % across the images between zero field and 2.0 mT. As a comparison, for a data set of 20 repetitions at zero field analysed identically, the variation in the percentage standard deviation was also ± 0.2 %. Although detector setup was performed at 3.0 mT, the normalization procedure failed to produce a normalization sinogram at this field and image results could not be compared directly.

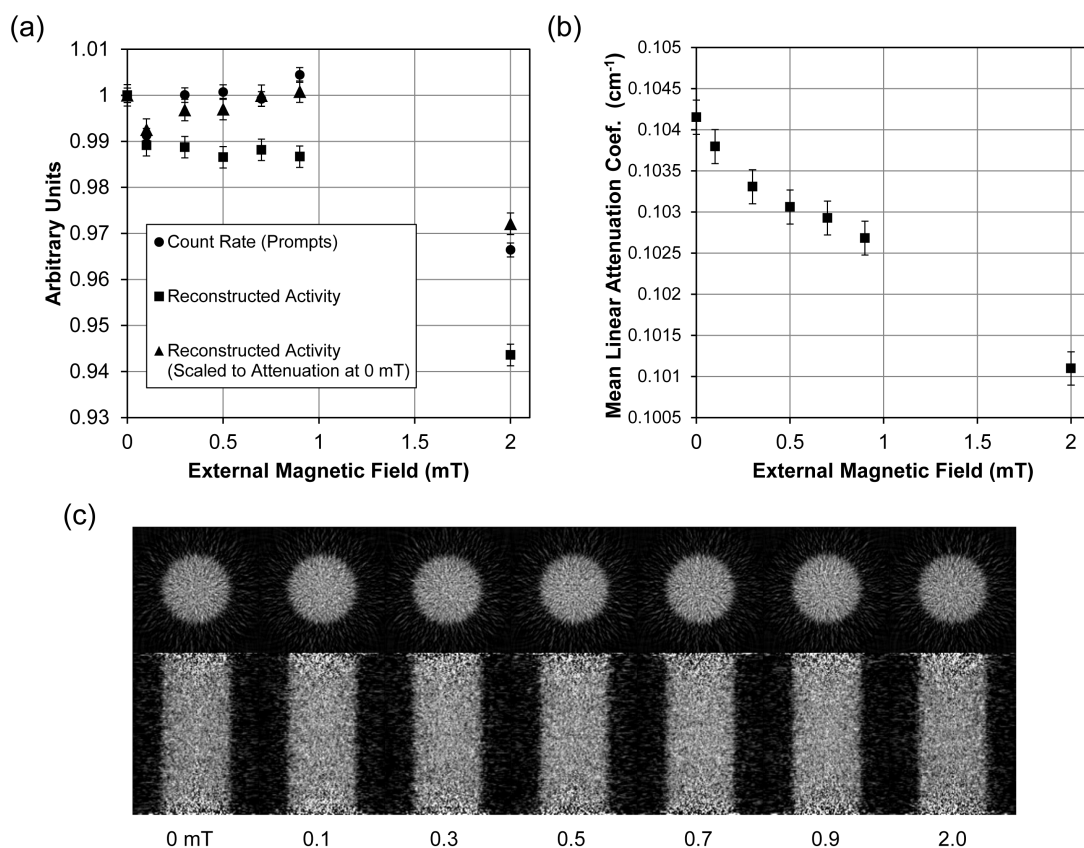


Figure 2.3: (a) Plot of prompts rate and reconstructed activity normalized to the value at zero field as a function of applied magnetic field for the cylinder source. The reconstructed activity values are also shown after adjusting to account for changes in the attenuation coefficient relative to the attenuation coefficient measured at zero field. (b) Plot of mean attenuation coefficient as a function of applied magnetic field. The proportional decline of the attenuation coefficient as the field increased appears to correlate with the increasing divergence between the prompts rate and the reconstructed activity. The error bars are estimated from repeated emission and transmission scans (20 repetitions) and uncertainty in the temperature measurement. (c) Reconstructed images of the cylindrical source at various fields showing the central axial slice (top) and the central coronal slice (bottom) using the same contrast colour scheme. All emission data were corrected for the decay of Ge-68 and gantry temperature.

2.3.2 Image Resolution and Positioning Accuracy

Figure 2.4 shows that the image resolutions for the point source in the radial (x), tangential (y) and axial (z) directions were not significantly affected for various point source positions through the range of magnetic fields tested. The maximum deviations of the FWHM from the zero field case were typically less than 5 per cent. The positioning accuracy of the reconstructed point source for each coordinate as a function of applied magnetic field is shown in Figure 2.5. The values correspond to the displacement from the coordinates of the point source image at zero field.

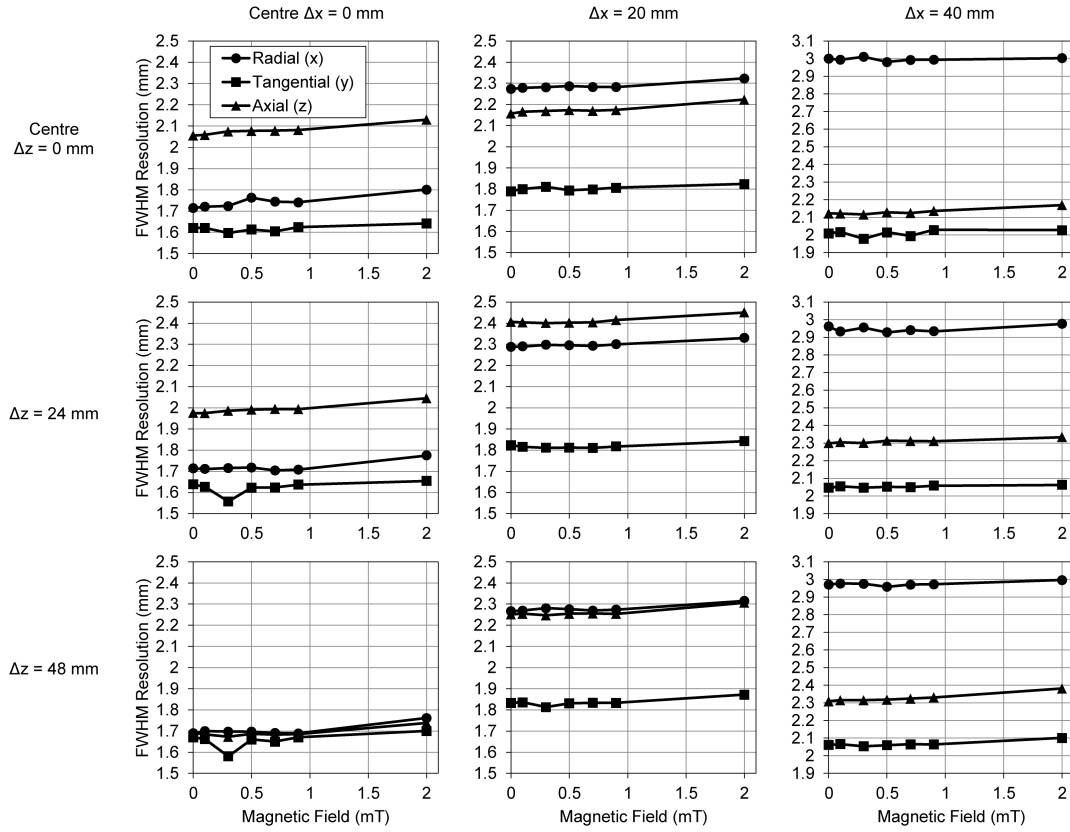


Figure 2.4: Full width at half maximum in each direction for the reconstructed image of a point source located at nine positions in the field of view as a function of magnetic field. The uncertainty in positioning was estimated by taking the standard deviation for multiple repetitions at zero field: ± 0.01 mm for radial (x); ± 0.007 mm for tangential (y); and ± 0.005 mm for axial (z).

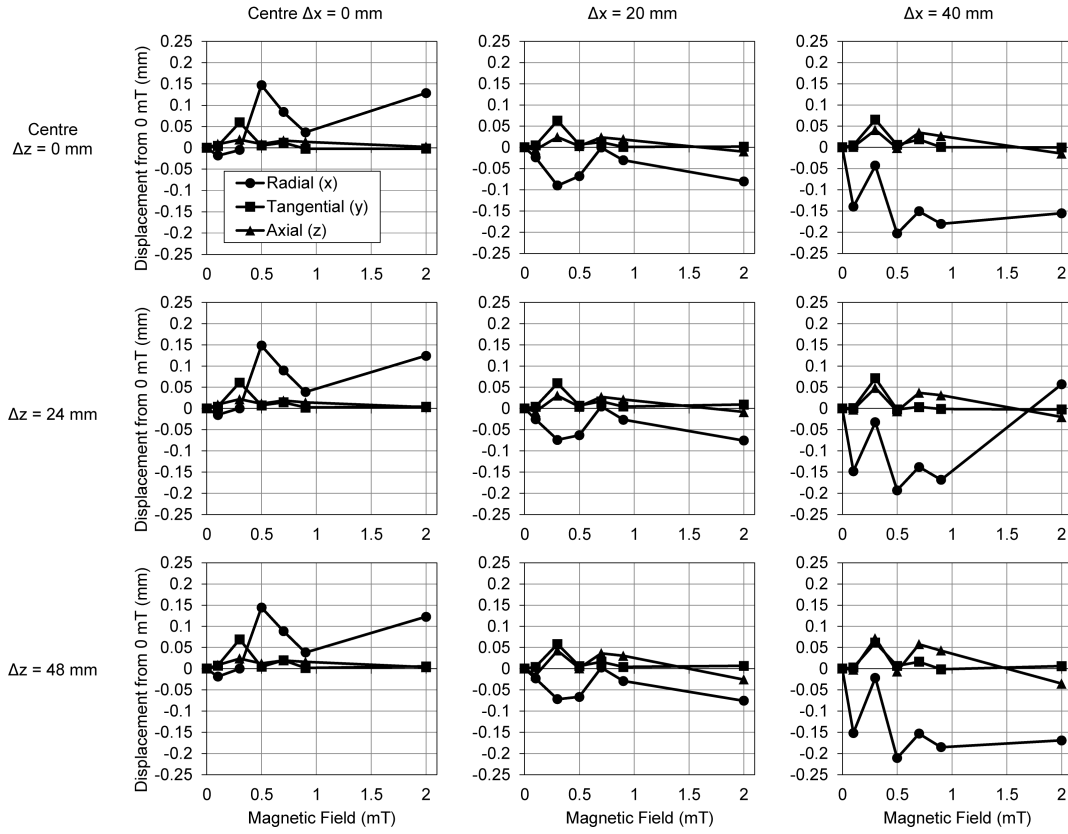


Figure 2.5: Position displacement as a function of magnetic field relative to the case at zero field for images of a reconstructed point source at nine positions in the field of view. The uncertainty in positioning was estimated by taking the standard deviation for multiple repetitions at zero field: ± 0.06 mm for radial (x); ± 0.004 mm for tangential (y); and ± 0.01 mm for axial (z). To set the x position, the point source cube was positioned manually against a stopper, increasing the positioning uncertainty for the radial (x) direction.

2.3.3 Position Profiles, Energy Spectra and Time Resolution

Figure 2.6 shows the position profiles acquired during detector setup for a typical block at a range of field strengths. An analysis of the energy spectra for three crystals in this block is also included as a function of magnetic field. As the external field increased, the magnitude of changes in peak coordinates in the

position profile increased showing that electron trajectories within the photomultiplier tube were sensitive to magnetic field. Figure 2.7 shows the emission energy spectra for three crystal positions for several magnetic field strengths. The energy bin of the photopeak maximum tended to decrease with greater field strengths, while the energy resolution worsened at higher fields. The transmission energy spectra are shown in Figure 2.8.

Differences in the profiles and energy spectra between zero field and 0.9 mT were inconsequential to the detector setup procedure. Although the positions of the photopeak in the emission energy spectra had changed at 0.9 mT, it was nevertheless possible to distinguish the photopeak and the noise shoulder for each crystal. At 2.0 mT, the photopeak was mixed with the noise shoulder for some of the crystals. The coordinates of peaks in the position profile were still identifiable, but there was a reduction in the number of counts for crystals near the centre of the block and the position profile was skewed. At this field, the distortion of the position profiles prevented the peak finding algorithm from automatically generating proper look up tables for most blocks. It was therefore necessary to select each peak position manually during detector setup – a process that took approximately 30 hours to complete. These effects were worse at 3.0 mT where some crystals had very few counts and it was necessary to infer the locations of peaks near the block centre.

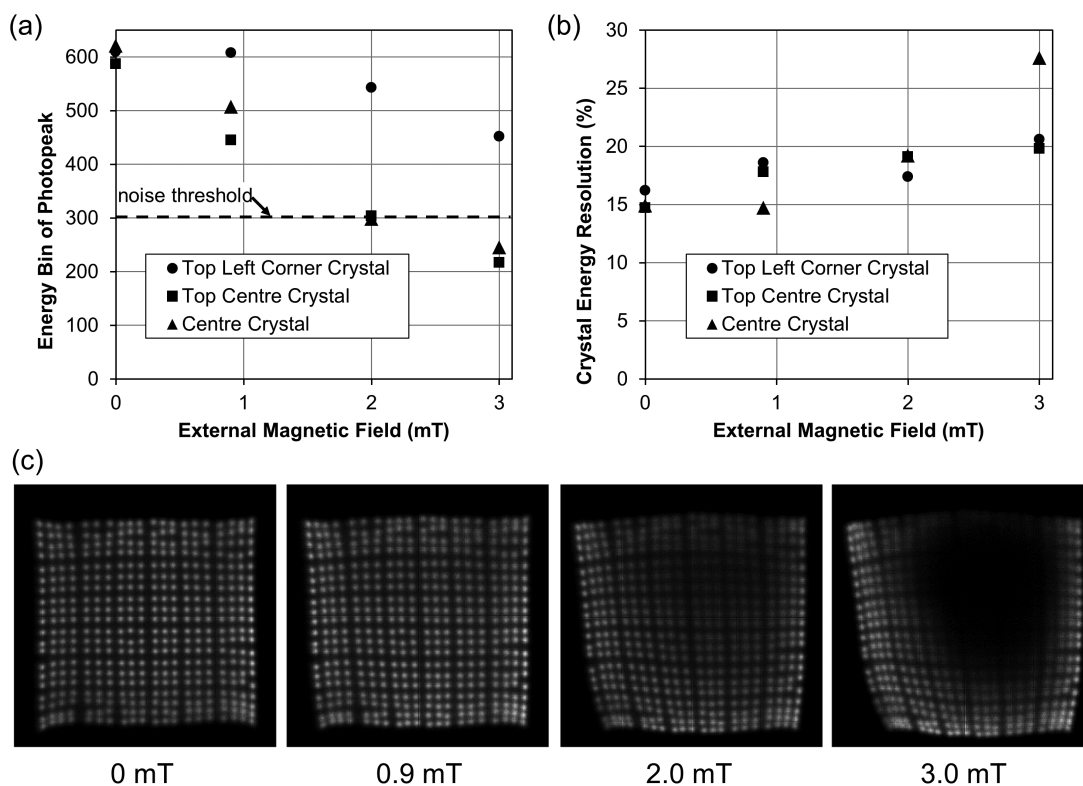


Figure 2.6: Analysis of flood source position profiles for the same detector block at different field strengths (topmost position farthest from the bed side). (a) The energy bins of the photopeak maxima are shown for three separate crystals: Top left corner (position $[x,y] = [0,0]$), top centre (position $[10,0]$) and centre (position $[10,10]$). The dashed line indicates the approximate upper extent of noise in the energy spectra where the noise shoulder would dominate the photopeak. (b) The energy resolution of each photopeak (FWHM) is shown as a function of magnetic field. (c) The peaks in the position profiles correspond to the coordinates of scintillation events in each of the 400 crystals in the detector. Up to 2.0 mT, positions could be clearly identified for each crystal in most detectors. At 3.0 mT, the crystals near the centres of most blocks had very few counts and the positions could not be identified.

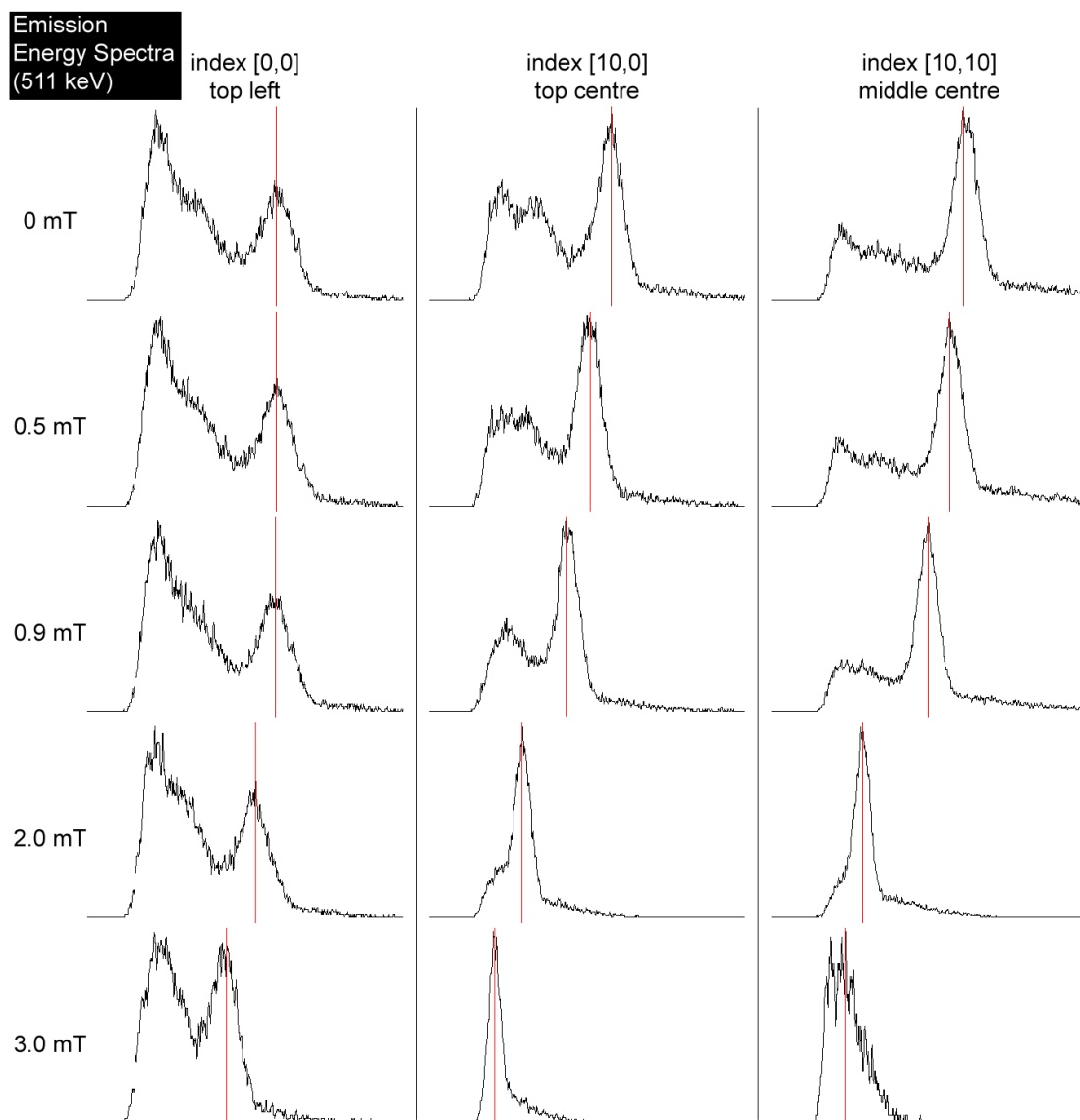


Figure 2.7: Emission energy spectra for the three crystal indices analyzed in **Figure 2.6** shown at various field strengths. The spectra shown are screen captures from the detector setup utility and are given without axes. The number of bins on the horizontal axis is 1024 and each spectrum is normalized to the same vertical height. The red vertical line in each spectrum indicates the energy bin of the photopeak (511 keV). As the field increased, the energy bin of the photopeak tended to decrease, consistent with a reduction in absolute detector efficiency. All photopeaks were distinguishable from the noise threshold up to 0.9 mT.

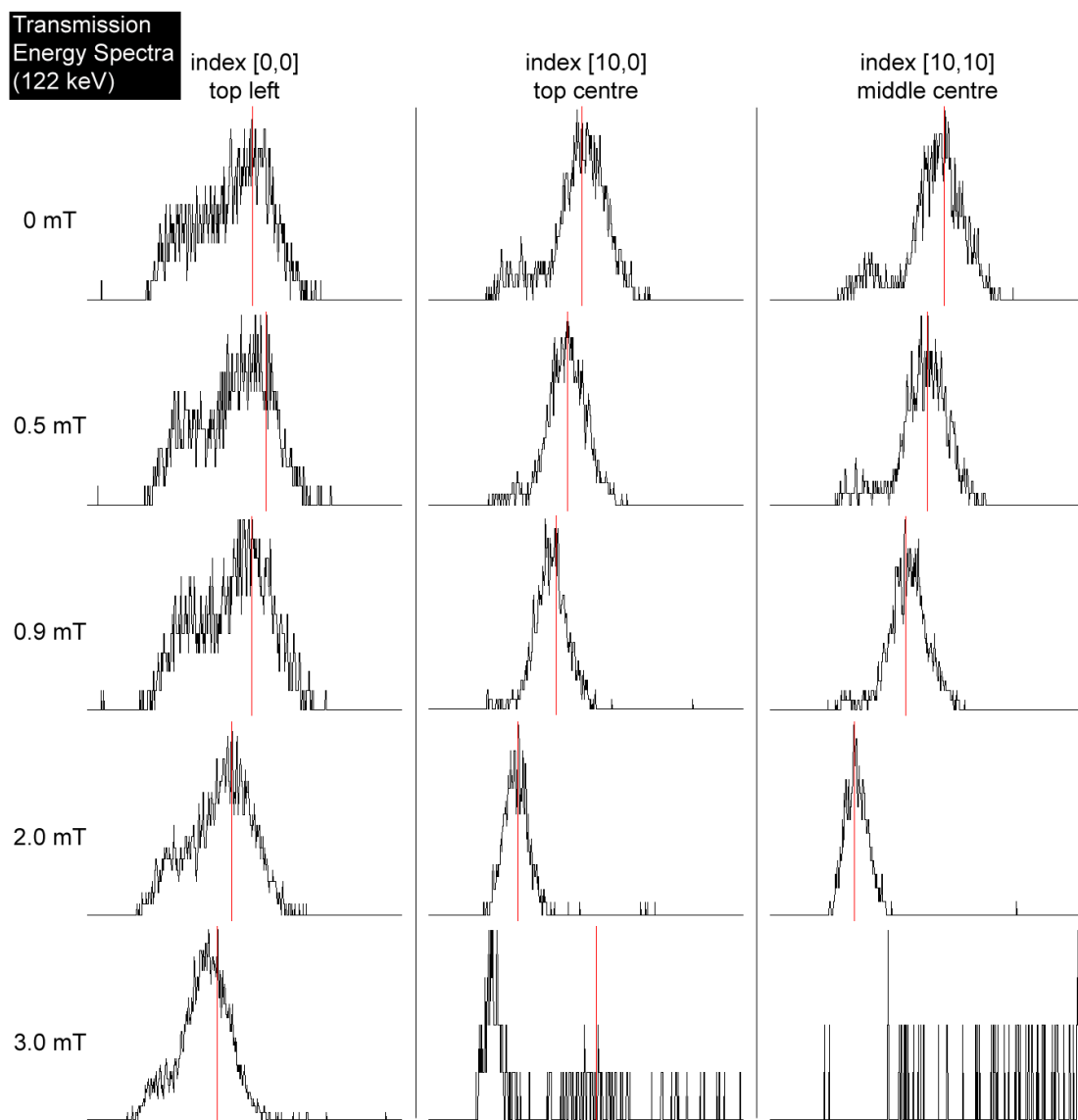


Figure 2.8: Transmission energy spectra for the three crystal indices analyzed in **Figure 2.6** and **Figure 2.7** shown at various field strengths. The energy of the photopeak was 122 keV. The energy bin of the photopeak in the transmission energy spectra tended to decrease with increasing magnetic field, similar to the case for the emission data.

Figure 2.9 shows the magnetic field dependence of the timing resolution (FWHM) for the same detector block analysed in Figure 2.6. The time performance worsened as the field increased. Other detector blocks showed similar behaviour.

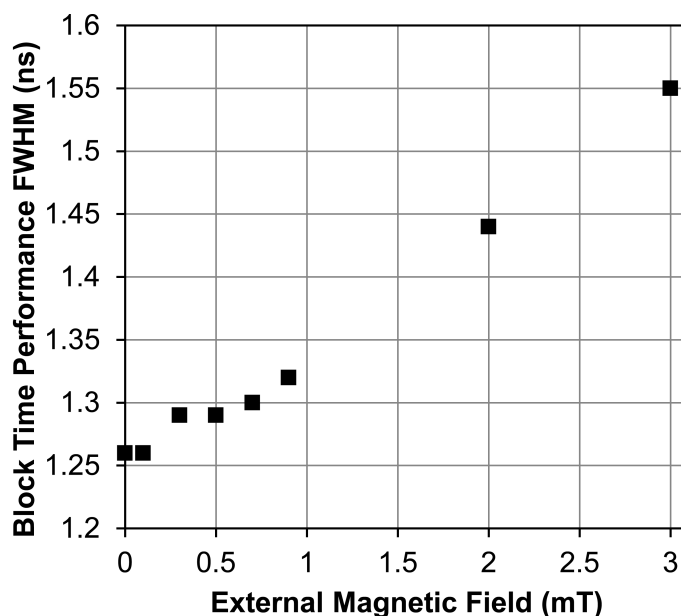


Figure 2.9: Block time resolution as a function of magnetic field for the same detector block as in **Figure 2.6**.

2.3.4 Efficiency Maps

Efficiency maps are shown at various field strengths for the ring of blocks closest to the bed side of the scanner in Figure 2.10(a) for the emission data and in Figure 2.10(b) for the blank transmission data. Each crystal element efficiency is normalized to 1 for the case at zero field. The efficiency maps of one block at 2.0 mT, highlighted in cyan, are expanded in Figure 2.10(c) and Figure 2.10(d) for emission and transmission data, respectively. It should be noted that as field increased, the efficiency generally became lower in the centre but did not change

significantly at the edges. Figure 2.10(e) and Figure 2.10(f) show the efficiency line profiles at various field strengths for the highlighted block using the crystals bounded by the white dashed lines in the expanded efficiency maps. For the emission efficiency maps, there were no significant changes up to 0.9 mT. The crystal efficiencies for the transmission data were somewhat more sensitive to magnetic field and variations in efficiency of approximately $\pm 10\%$ were observed in some blocks at 0.9 mT.

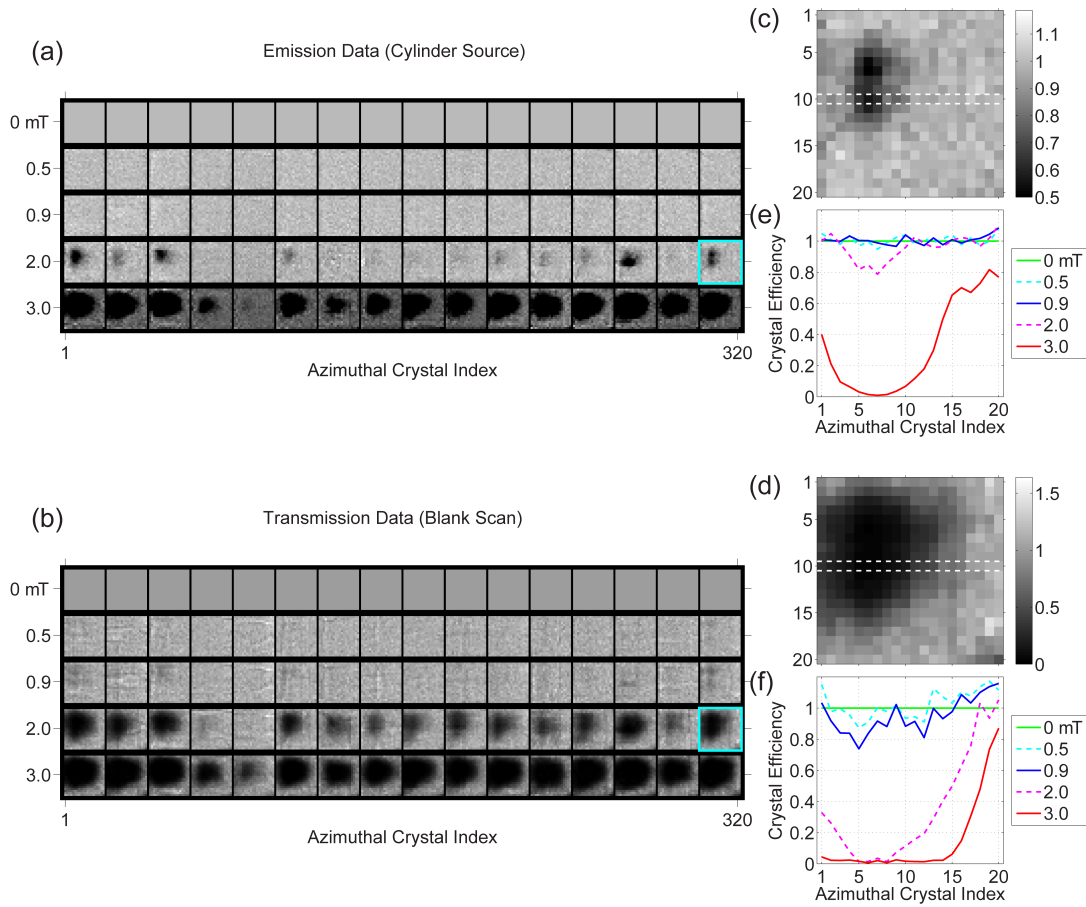


Figure 2.10: (a) & (b) Efficiency map of the same ring of 16 detector blocks closest to the bed side of the scanner at various magnetic field magnitudes for emission data (a) and for blank transmission data (b). The three other rings of blocks are not

displayed, but showed a similar response. The greyscales represent the counts assigned to each crystal normalized to the acquisition at zero field. (c) & (d) An expanded view of the particular block highlighted by the cyan box. The white dashed lines represent the bounds of the pixels used to produce the line profiles in (e) & (f) at various field strengths.

2.4 Discussion

The degradation of multiple measures of PET performance in the presence of an external magnetic field was evident. External fields of 0.9 mT and below resulted in no significant changes in most investigated metrics, with the exception of a 1% decrease in transmission scan sensitivity. At 2.0 mT, significant changes appeared in quantitative measures of PET performance; however no visible artifacts or distortions appeared in reconstructed images at this field. At 3.0 mT, the detector position profiles were significantly affected and it was not possible to perform a normalization calibration.

The distortions and count-rate drops affecting the position profile at higher field strengths are consistent with changes visible in the efficiency maps and can be understood by considering the deflection of the electron trajectory within the photomultiplier tube. With the magnetic field oriented along the scanner's axial direction, the Lorentz force acting on electrons initially moving radially outward will cause an azimuthal deflection. Under such conditions, a gamma ray scintillation occurring in a particular crystal may be registered at a different azimuthal coordinate than would be the case at zero field. This explanation is consistent with the azimuthal shift of peak coordinates in the flood source position profiles, as observed in Figure 2.6 in the horizontal direction. The changes observed in the position profiles and efficiency maps are in reality more

complicated due to non-radial components of the electron trajectory. The extent of distortions in the position profile was not extreme at the fields tested and it was possible to generate look up tables accurately up to 2.0 mT.

One might assume that the electron path would be primarily in the radial direction, and that therefore the detectors would be most sensitive to magnetic fields oriented parallel to the photocathode, along the axial direction, where the field component is perpendicular to the electron path. However, it has been shown that the R8900 photomultiplier tube is most sensitive to the field component perpendicular to the photocathode, along the radial direction of the scanner [12,15]. The most significant deflections are likely to occur between the photocathode and the first dynode, or between the last dynode and the anode, where the electron path is longest. Compared with previous position-sensitive photomultiplier tube designs from the manufacturer, which were used in previous-generation small animal PET scanners, the area of the photocathode in the R8900 is larger than the area of the dynode grid, requiring a focusing mesh. The result is a longer, non-radial electron path between the photocathode and the first dynode when compared with earlier devices. Therefore the R8900 is expected to be more sensitive to external magnetic fields. In a future study, the effects from fields of different directions should be investigated.

The time resolution worsened as the field increased. The limit specified by the manufacturer for acceptable timing performance is 1.5 ns FWHM. At fields lower than 2.0 mT, the timing performances of the detectors were well within this limit. Changes in the time resolution were not a limiting factor for operating the PET scanner in the presence of magnetic fields.

For higher fields, we observed a reduction in count rate for the central crystals in each block with some blocks being more sensitive to this effect than others. At the same field strength, transmission acquisitions showed a greater drop in sensitivity than emission acquisitions. The most likely cause is the lower energy of the Co-57 photons (122 keV) used in the transmission scan. The Co-57 photopeaks were closer to the noise level in the energy spectra and thus more susceptible to small shifts in the position of the photopeak than the 511 keV photopeaks in the emission data. Up to 0.9 mT, the distribution of counts was sufficiently uniform in both the emission and transmission efficiency maps that it was possible to correct for the small variations through normalization and blank transmission calibrations. At 2.0 mT, the variation in crystal efficiency for the transmission scan was substantial for most blocks, and at 3.0 mT, both the transmission and emission efficiency maps were significantly affected.

Despite the distortions observed in the position profiles, there were no apparent changes in image quality observed for the Ge-68 cylinder source up to 2.0 mT. The apparent reduction in reconstructed activity up to 0.9 mT can be attributed to the $-1.5\%/mT$ reduction in measured attenuation coefficient. At 2.0 mT, the sensitivity of the emission acquisition was lower by approximately 3% when corrected for the field dependence of the attenuation correction. This suggests that the reconstructed activity can be corrected for images with attenuation correction for fields up to 0.9 mT. One explanation for the decrease in measured attenuation coefficient is the presence of Compton scattered photons in the transmission scan combined with field-dependent changes in the detector energy spectra. Attenuation correction factors are computed from the comparison of blank

transmission data, with no attenuating material in the bore, to transmission data with attenuating material present. Lower-energy Compton scattered photons are present in the transmission scan, but not in the blank scan. At higher fields, the detector gain decreases and the energy window begins to include more spurious prompts due to electronic noise and small-angle Compton scattered transmission photons. These changes to the energy spectra have a greater effect on transmission acquisitions due to their already low starting energy (122 keV). As the field increases, a greater fraction of Compton scattered photons are detected in the energy window, which results in a reduction of the apparent attenuation.

No meaningful off-axis distortions were observed for images of the point source at fields up to 2.0 mT. FWHM resolutions did not change meaningfully for all positions tested up to 0.9 mT, while at 2.0 mT, the FWHM changed by a maximum of 5%. All changes in position relative to the zero field case were significantly smaller than the resolution of the scanner up to 2.0 mT and could be attributed to uncertainties in the physical placement of the point source.

This study suggests an upper limit of 0.9 mT external magnetic field when siting a Siemens Inveon PET in the vicinity of an MRI scanner. The effects on PET performance are significant beyond 2.0 mT and it would be clearly inadvisable to operate the PET scanner under conditions much beyond this field strength. A typical actively-shielded preclinical MRI scanner with main field between 7.0 T and 11.7 T has a 0.5 mT fringe field at a radial distance approximately ± 2 m from the centre. Under such an arrangement, sequential PET and MRI imaging where the animal is moved from one scanner to the other in close proximity would be feasible for many existing imaging facilities. Recently, lower field MRI systems

having negligible fringe field have been made commercially available. PMT-based PET scanners can be placed in close proximity to these types of MRI systems [8].

2.5 Conclusion

The performance of the Siemens Inveon photomultiplier tube based small animal PET system was investigated during exposure to axial magnetic fields of various strengths. For external fields with magnitude 2.0 mT and higher, significant changes were observed in quantitative measures of PET performance. Such effects were negligible at fields between 0 – 0.9 mT.

2.6 Acknowledgements

This work was supported by the Natural Sciences and Engineering Research Council of Canada (NSERC), the Ontario Innovation Trust, the Canadian Foundation for Innovation, and the Plunkett Foundation. B.A.C holds the Canada Research Chair in Medical Physics at the University of Western Ontario. G.A.B. was supported by an NSERC Alexander Graham Bell Canada Graduate Scholarship.

2.7 References

1. Maramraju SH, Smith SD, Junnarkar SS, Schulz D, Stoll S, Ravindranath B, Purschke ML, Rescia S, Southehal S, Pratte JF *and others*. Small animal simultaneous PET/MRI: initial experiences in a 9.4 T microMRI. *Physics in Medicine and Biology* 2011;56(8):2459-2480.
2. Wehrl HF, Judenhofer MS, Thielscher A, Martirosian P, Schick F, Pichler BJ. Assessment of MR Compatibility of a PET Insert Developed for Simultaneous Multiparametric PET/MR Imaging on an Animal System Operating at 7 T. *Magnetic Resonance in Medicine* 2011;65(1):269-279.
3. Yamamoto S, Imaizumi M, Kanai Y, Tatsumi M, Aoki M, Sugiyama E, Kawakami M, Shimosegawa E, Hatazawa J. Design and performance from an integrated PET/MRI system for small animals. *Annals of Nuclear Medicine* 2010;24(2):89-98.
4. Catana C, Procissi D, Wu YB, Judenhofer MS, Qi JY, Pichler BJ, Jacobs RE, Cherry SR. Simultaneous in vivo positron emission tomography and magnetic resonance imaging. *Proceedings of the National Academy of Sciences of the United States of America* 2008;105(10):3705-3710.
5. Raylman RR, Majewski S, Velan SS, Lemieux S, Kross B, Popov V, Smith MF, Weisenberger AG. Simultaneous acquisition of magnetic resonance spectroscopy (MRS) data and positron emission tomography (PET) images with a prototype MR-compatible, small animal PET imager. *Journal of Magnetic Resonance* 2007;186(2):305-310.
6. Marsden PK, Strul D, Keevil SF, Williams SCR, Cash D. Simultaneous PET and NMR. *British Journal of Radiology* 2002;75:S53-S59.
7. Hawkes RC, Fryer TD, Lucas AJ, Siegel SB, Ansorge RE, Clark JC, Carpenter TA. Initial Performance Assessment of a Combined microPET (R) Focus-F120 and MR Split Magnet System. 2008 Ieee Nuclear Science Symposium and Medical Imaging Conference (2008 Nss/Mic), Vols 1-9 2009:2948-2953.
8. Schmid A, Schmitz J, Mannheim JG, Maier FC, Fuchs K, Wehrl HF, Pichler BJ. Feasibility of sequential PET/MRI using a state-of-the-art small animal PET and a 1 T benchtop MRI. *Molecular Imaging and Biology* 2013;15(2):155-165.
9. Constantinescu CC, Mukherjee J. Performance evaluation of an Inveon PET preclinical scanner. *Physics in Medicine and Biology* 2009;54(9):2885-2899.
10. Bao Q, Newport D, Chen M, Stout DB, Chatziioannou AF. Performance Evaluation of the Inveon Dedicated PET Preclinical Tomograph Based on the NEMA NU-4 Standards. *Journal of Nuclear Medicine* 2009;50(3):401-408.

11. Mintzer RA, Siegel SB. Design and performance of a new pixelated-LSO/PSPMT gamma-ray detector for high resolution PET imaging. 2007 Ieee Nuclear Science Symposium Conference Record, Vols 1-11 2007:3418-3422.
12. Kawasaki Y, Bertaina ME, Sakaki N, Shimizu HM, Inoue N, Hasegawa S, Ohtsu I, Adachi T, Ebisuzaki T, Hirota K *and others*. Performance of a multi-anode photomultiplier employing a weak electrostatic focusing system (Hamamatsu R8900 series). Nuclear Instruments & Methods in Physics Research Section a-Accelerators Spectrometers Detectors and Associated Equipment 2006;564(1):378-394.
13. Mao RH, Zhang LY, Zhu RY. Optical and Scintillation Properties of Inorganic Scintillators in High Energy Physics. IEEE Transactions on Nuclear Science 2008;55(4):2425-2431.
14. National Electrical Manufacturers Association. NEMA Standard Publication NU 4-2008: Performance Measurements of Small Animal Positron Emission Tomographs. Rosslyn, VA: National Electrical Manufacturers Association; 2008.
15. Artuso M, Boulahouache C, Blusk S, Butt J, Dorjkhaidav O, Menaa N, Mountain R, Muramatsu H, Nandakumar R, Randrianarivony K *and others*. Performance of a C4F8O gas radiator ring imaging Cherenkov detector using multi-anode photomultiplier tubes. Nuclear Instruments & Methods in Physics Research Section a-Accelerators Spectrometers Detectors and Associated Equipment 2006;558(2):373-387.

Chapter 3

3 Approaches to Combining the Siemens Inveon PET with MRI¹

In this chapter, I survey the feasibility of different methods of utilizing the Siemens Inveon small animal PET scanner in a PET-MRI facility.

3.1 Introduction

The Siemens Inveon small animal PET is in widespread use with well over 100 installations worldwide. There has been considerable interest in setting up preclinical imaging facilities with the capability to acquire both PET and MRI images in the same study. Until very recently, hybrid simultaneous PET-MRI systems for small animal applications were not available commercially and considerable engineering effort has been directed to developing one-off MR-compatible PET inserts for use with high-field superconducting MRI scanners. On the other end of the spectrum, some facilities have used sequential imaging workflows, which involve moving the animal between a room containing the MRI scanner and a different room containing the PET scanner. This latter approach has the advantage of requiring no unconventional scanner modifications or compromises to PET or MRI performance. However, a significant limitation to

¹ The content of this chapter has not been submitted for publication to any journal. Versions of some of the figures and text contained in this chapter have appeared in conference contributions presented by the author.

this two-room approach is that the accuracy of co-registration is reduced if the animal is transferred from one bed to another or the animal is roused from anaesthesia between scans. In this chapter, I explore various approaches of siting a small animal PET scanner, specifically the Siemens Inveon PET, in the same room as an MRI scanner.

There are several desirable criteria for combining PET and MRI in the same room that should guide the choice of approach. It is important that PET and MRI performance are not significantly compromised compared with standalone PET or MRI procedures. The results from Chapter 2 suggest that for the Siemens Inveon PET, performance is not impacted at magnetic fields below approximately 1 mT. It is also important to design the facility so that PET and MRI images can be co-registered accurately. Ideally, the same animal holder should be used for both modalities so that the co-registration method would be an *a priori* rigid-body transformation. It is also desirable to have the dual modality facility take up minimum physical floor space. Other important criteria include the following: The combined system should be easy for end users to operate, the cost of additional equipment should be significantly less than the costs of the scanners themselves, and the room should not require significant modifications (physical, electrical, chilled water supply, etc.) beyond what is typical for a small-animal MR imaging facility.

3.2 Combining the Inveon PET with Field-Cycled MRI

Current approaches to systems that integrate PET and MRI in a compact system typically (a) modify MRI in some manner to make it compatible with

conventional PET, or (b) alter PET hardware to make it compatible with conventional MRI. One approach of the second type has been to employ avalanche photodiodes (APD), or other solid-state detectors, which are unaffected by magnetic fields, in place of PMTs in an MR-compatible PET insert. An approach of the first type is to use field-cycled MRI (FCMRI) with a conventional PMT-based PET system. Combining PET with FCMRI would enable the use of commercially available, highly optimized PET systems with potentially little physical modification.

In a type of FCMRI called prepolarized FCMRI, two sets of resistive electromagnets independently produce the polarizing and readout magnetic fields. The polarizing field supplies the main magnetization and must be strong, but need not have high spatial or temporal uniformity. Conversely, the readout field must have high spatial and temporal uniformity, but need not be strong [1]. A fully-functional FCMRI system has been built and has generated images of good quality [2]. The magnetic fields of the FCMRI system can be turned on and off during a scan allowing PMTs to operate normally during the time the field is off. Proof-of-principle tests have shown that linear and mesh PMTs recovered normal operation within 2-3 milliseconds of the field being turned off with no long-term effects [3]. An example of a PMT-based PET system operating successfully when interleaved with an FCMRI system has been demonstrated in Chapter 4. While this proof-of-principle system used coarse PET detectors from a human-scale scanner, PET detectors with smaller scintillator crystal pitch are more appropriate for small animal imaging.

In this section, I describe two designs for a PET-FCMRI system specifically based on the Siemens Inveon small-animal PET: The first design concept is an extension of the proof-of-principle approach described in Chapter 4 where the PET detectors are placed in an axial gap in the FCMRI system. The second concept is a docking geometry where the FCMRI system is aligned axially with the PET system, similar to the geometry of PET-CT.

3.2.1 Interleaved Field-Cycled MRI – Common Imaging Region

3.2.1.1 System Description

A larger-scale FCMRI system with an axial gap was under consideration for integration with the Inveon PET system. The proposed geometry is shown in Figure 3.1. At 60 kW, the polarizing magnet produces a polarizing magnetic field of 0.5 T. Calculations showed that the readout-field inhomogeneity after mechanical shimming was expected to be less than 100 ppm over a 10 cm diameter sphere. Resistive shimming could be used to further reduce the inhomogeneity to better than 10 ppm.

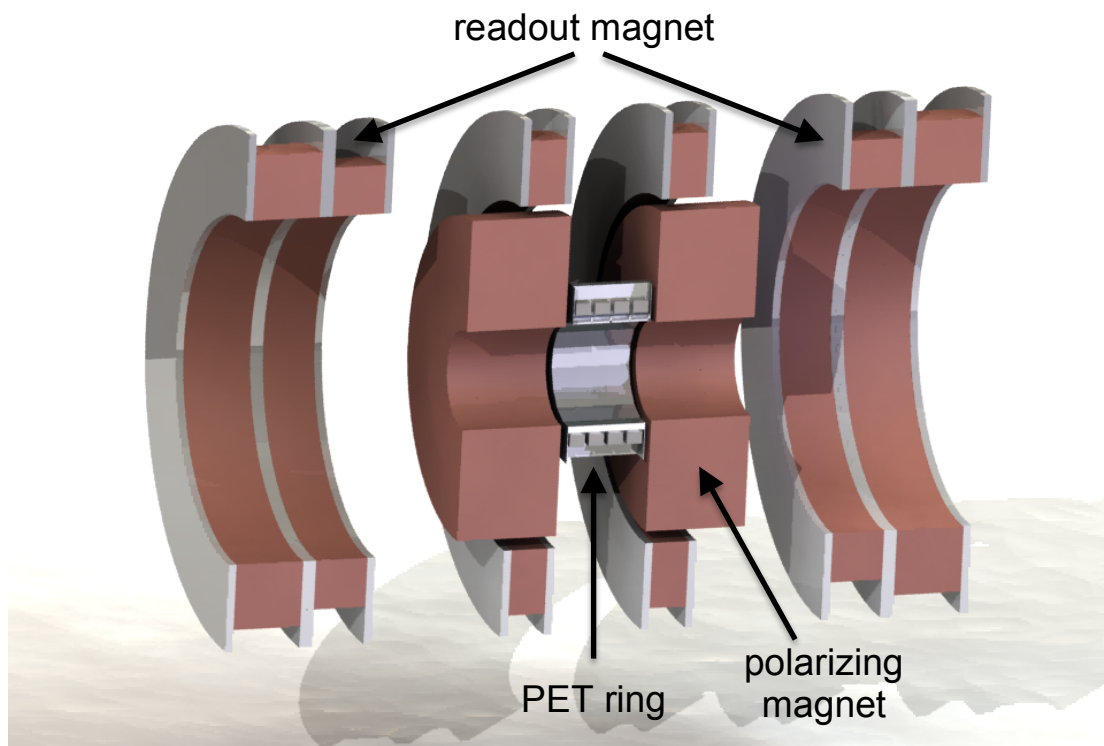


Figure 3.1: Cross-sectional view through a design of a PET/FCMRI system showing PET ring (center), polarizing magnet (two inner coils on either side of the PET ring) and readout magnet (six outer coils). The inner diameter is 16 cm.

The proposed system offers increased flexibility in PET-MRI sequences. Figure 3.2 shows a simple interleaved sequence. This will necessarily result in a reduced duty cycle for both modalities compared with simultaneous PET-MRI approaches. Alternate sequences could conduct MR while the animal metabolizes the radiotracer and then acquire subsequent PET images interleaved with further MRI data acquisition.

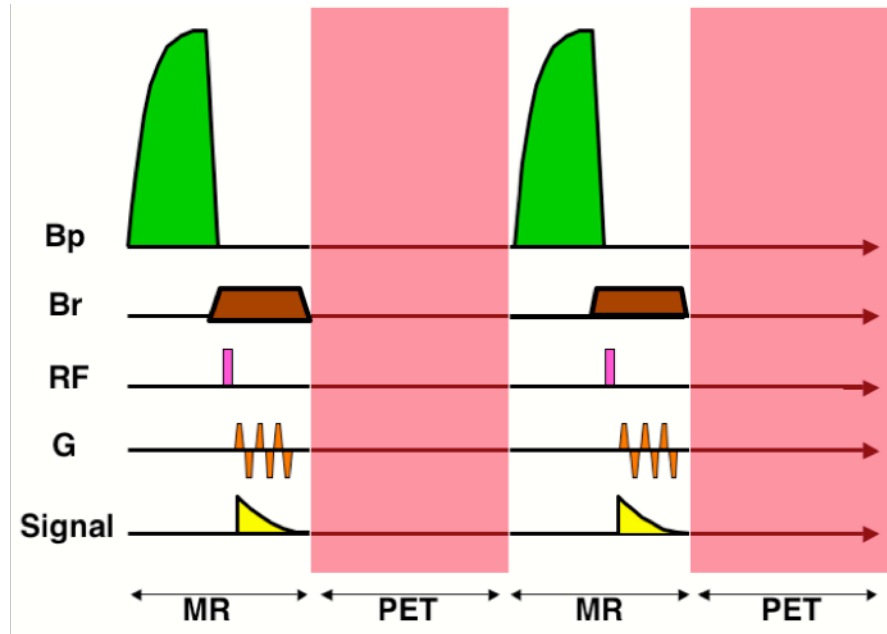


Figure 3.2: A prototypical timing sequence for the interleaved PET-FCMRI system. PET data can be acquired while all magnetic fields are switched off. B_p represents the strong polarizing magnetic field, B_r represents the homogeneous and stable readout magnetic field, RF refers to radiofrequency pulses, and G refers to gradient coil operation.

3.2.1.2 Discussion

The proposed PET-FCMRI approach could have several advantages over other PET-MRI approaches but the system integration carries substantial risk.

One appealing advantage of this approach is that PET data can be acquired in a quasi-simultaneous manner with MRI data. This would enable the possibility to perform MR-based motion correction of the PET images for changes that occur on time scales longer than tens of seconds. Another significant benefit is that the PET and MRI imaging regions occupy the same location. There would be no need to move the animal between modalities. The transformation required to coregister

PET and MR image data would be straightforward to characterize and would be the same for every scan.

Like other methods proposed in this chapter, this approach uses the commercially available Inveon system offering state-of-the-art timing resolution, energy resolution, and highly optimized event processing hardware. While FCMRI is less mature than conventional MRI, it is likely more critical to achieve the best possible PET resolution rather than maximize MR image quality. FCMRI image quality is more than sufficient for the anatomical detail required for image coregistration. Furthermore, FCMRI has several advantages over conventional MRI: the ability to vary the amplitude and duration of the polarizing field offers novel T_1 dispersion contrast possibilities; substantially reduced susceptibility artifacts enable imaging around metallic devices; lower required RF power drastically reduces the specific absorption rate; gradient operation only in the readout magnetic field renders the system virtually silent.

The primary drawback of this approach is that the detector ring of the PET system would need to be removed from its standard housing and placed in the axial gap of the FCMRI system. One problematic engineering challenge is to implement a temperature control system for the detector ring because the lutetium orthosilicate (LSO) based scintillator is sensitive to temperature and experiences a change in light yield of $-0.2\%/^{\circ}\text{C}$ [4].

Another disadvantage is that the hybrid system would no longer benefit from the attenuation correction technique implemented on the original PET scanner. For attenuation correction, the Siemens Inveon includes two rotating Co-57 point

sources that are used in combination with bed motion to produce CT-like transmission data. While attenuation correction is less important in small animal imaging when compared with human imaging, it remains a necessary correction in order to measure quantitative tracer uptake values in small animals. Thus, a different system of attenuation correction would need to be implemented, such as an MR-based approach or rotating an external rod source around the animal and holder. These additional steps add complexity and an extra step in software to the PET imaging protocols and would substantially reduce the ease of use.

3.2.2 Sequential Imaging with PET Docked to FCMRI

3.2.2.1 System Description

Here we describe designs for a larger-scale FCMRI system for docking with the Inveon PET system. The FCMRI system would be a standalone scanner, which could achieve greater field strength and better homogeneity when compared with the design described in the previous section. The proposed geometry is shown in Figure 3.3. At 60-kW-continuous operation (180 A and 330 V), the main magnet would produce 0.7 T, and would be rough-shimmed to ~ 250 ppm homogeneity over a 10-cm-diameter sphere. First- and second-order resistive shims would be used to further reduce the inhomogeneity to better than 10 ppm. The main magnet wire would have 7x7 mm cross-section with a 5-mm-diameter liquid cooling channel. With 7 parallel cooling channels for each magnet half, the temperature rise under full load could be brought below 20°C with commercially available chillers. With gradients and shims, the bore diameter would be 15.9 cm. The length, diameter and mass of the system would be 72.5 cm, 61 cm and approx. 900 kg, respectively. The resistance and inductance would be 1.85 Ω and 0.81 H.

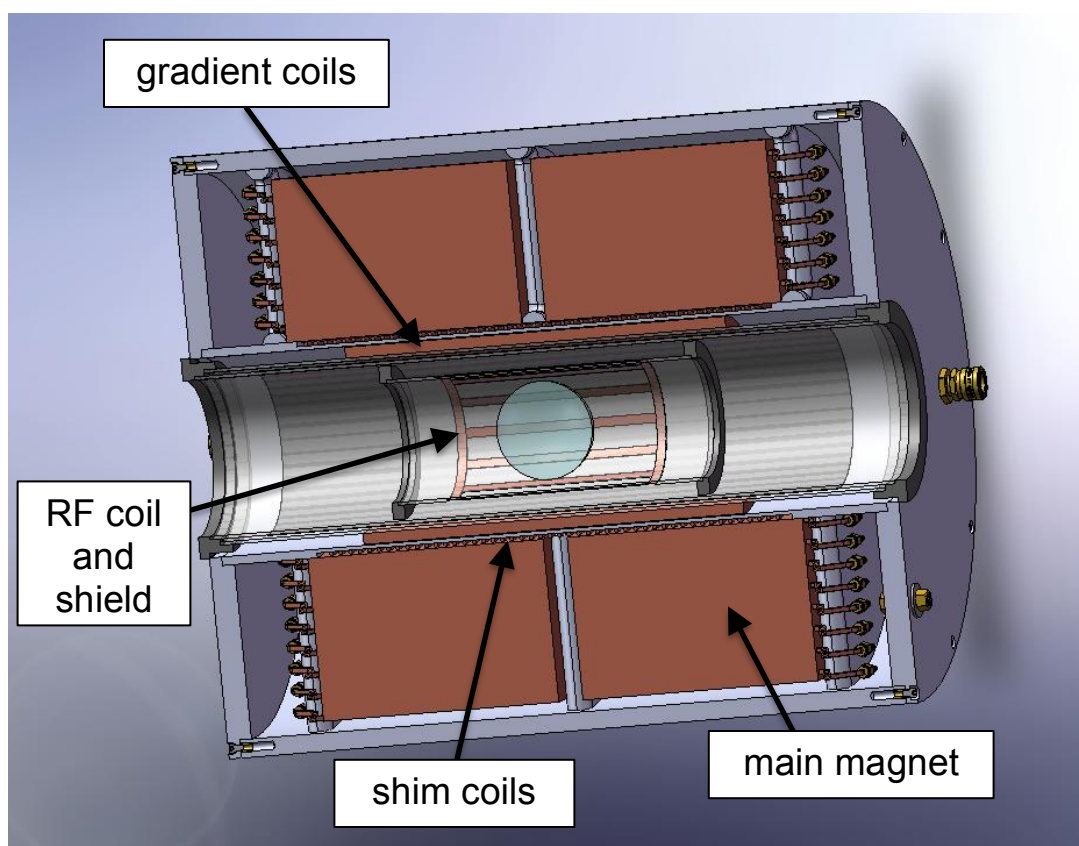


Figure 3.3: Cross-sectional view through the design of the FCMRI system. Shown (starting from center): 10-cm-diameter imaging volume, birdcage RF coil, RF shield, gradient set, second-order shims, main magnet. Liquid cooling inlet manifold shown on ends.

The proposed docking geometry is shown in Figure 3.4. The system is best suited for sequential PET-MRI sequences. This FCMRI system is designed so that it can be operated in continuous mode with 100% duty cycle for conventional MR sequences, but it can also be operated with dynamic field and prepolarization. The spacing of the two systems can be adjusted to account for support structures, and one proposed support structure is shown in Figure 3.5.

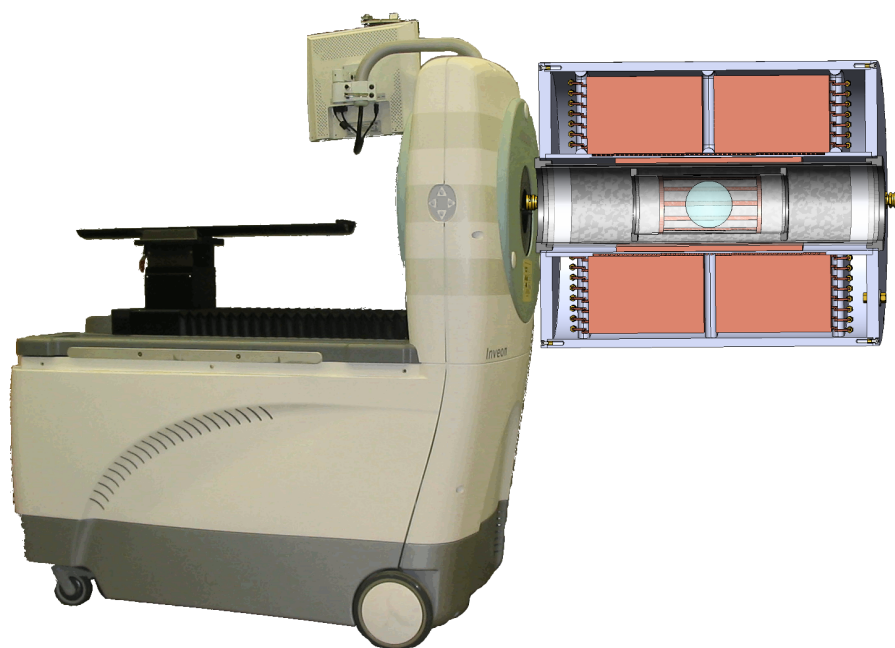


Figure 3.4: Docking geometry of the combined PET and field-cycled MRI system. An extendible bed (not shown) would move the subject between PET and MR imaging regions using the built in bed motion control system of the PET scanner. No modifications to the PET system would be necessary; however, a different bed would need to be constructed.

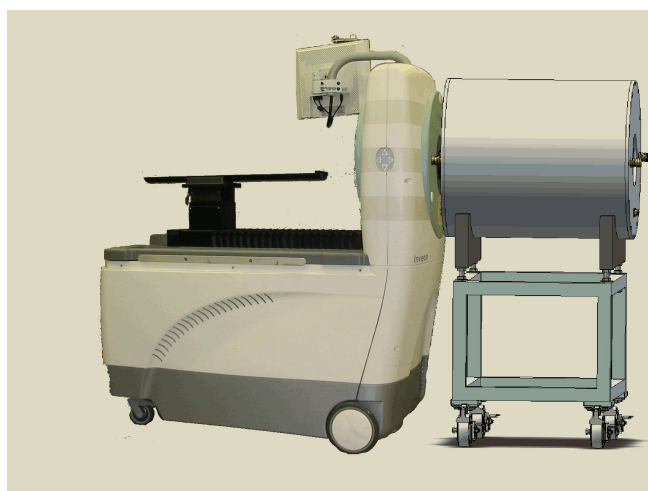


Figure 3.5: Geometry of the PET-FCMRI docked system showing support structures.

3.2.2.2 Discussion

Like the previous approach, using field-cycled MRI enables several unique MR imaging capabilities; however, in this proposed arrangement, the Siemens Inveon PET would remain intact and retain the full functionality of the attenuation correction and detector temperature control systems.

The design and construction of a FCMRI system without a gap would present somewhat less of an engineering challenge than building such a system with an axial gap because gradient coils could be designed on a simple cylindrical geometry.

While this approach has far fewer risks than the split FCMRI approach described in the previous section, there are several disadvantages from the perspective of system integration. For this approach, the PET and MR imaging regions are physically separate and the subject must be moved between the two regions by some movable bed mechanism. Interleaved imaging on time scales of about one minute is still conceivable, but this would require a bed motion control system that can move the animal between imaging regions rapidly and without human interaction. If the bed motion control system built into the Siemens Inveon were to be used for this purpose, it would be necessary to make modifications to the PET acquisition software. This automatic motion would only be possible if the FCMRI imaging region were unfeasibly close to the PET imaging region. For the geometry proposed here, the built in system can supply fine motion control, but the animal bed would need to be manually extended to reach the MR imaging region. Automatic motion between modalities could be achieved by placing the bed on a track controlled independently from the built in motion system, but this

is undesirable because the transmission scanning protocols rely on precise bed movements controlled by the scanner. Therefore, this docking PET-MRI approach is best suited for sequential imaging protocols. For a bed that moves linearly between the two imaging regions, the accuracy of PET-MRI image coregistration would be less than the case for a common imaging region arrangement, but it would be at least as good as arrangements where the bed is detached from one scanner and physically moved to the other scanner.

3.3 Combining the Inveon PET with Conventional Superconducting MRI Systems

Unlike field-cycled MRI where the all magnetic fields can be turned off in a short period of time, conventional superconducting MRI scanners have a strong main magnetic field that is always on. The so-called ‘fringe-field’ in the vicinity of a conventional MRI scanner is orders of magnitude weaker than the main magnetic field inside the scanner bore, but can still be strong enough to affect the operation of PET detectors. If the Siemens Inveon PET is to be used in the same room as a conventional MRI system, the magnetic field in the PET detector ring should be under 1 mT in the axial direction (see Chapter 2). To achieve this, the PET system can be placed sufficiently far from the MRI scanner that the fringe field at the detector ring is under 1 mT. For arrangements where the systems are closer together, the detectors must be shielded magnetically to bring the field at the detectors below 1 mT. The detectors can be shielded passively with permanent magnets and mu-metal casing, an approach taken in some human scale PET-MRI systems [5,6]; however, this would require extensive hardware modification of the Siemens Inveon PET and the use of permanent magnets would preclude moving

the scanner to a different location without removing the magnets. An alternative approach to shielding that avoids modifications to the PET system is to use an external electromagnet to null the fringe magnetic field at the position of the PET detectors. In this section, I analyse two arrangements for a PET-MRI facility based on the Siemens Inveon PET and a conventional superconducting MRI: using an actively powered electromagnetic shielding coil and separating the scanners within the room.

3.3.1 Dynamically-Controlled Electromagnetic Shielding of the PET Scanner

In this section, I describe an approach to PET-MRI in which a resistive electromagnet shield coil is used to null the field at the PMTs of the Siemens Inveon PET system in the vicinity of a superconducting MRI system.

3.3.1.1 System Description

The proposal described here is based on a Magnex 2.0 T 310-mm-bore MRI, although the method of designing the shield coil is general and can be applied to any MRI system. Our laboratory had recently come into possession of this particular MRI system and I studied it for this application. For ease of construction, the coil geometries investigated were single cylinders of various lengths, radii and axial positions. During exposure to magnetic fields, the Hamamatsu R8900 PMTs in the Siemens Inveon suffer changes in gain and efficiency. As long as the spatial field profile does not change with time, the PET system can be calibrated to account for the small changes in gain and efficiency that result from weak magnetic fields with negligible affect on performance. Based on the results from Chapter 2 and the findings reported by Kawasaki, *et al.*

[7], the goal was to reduce the magnetic field at the PET detector ring to significantly below 0.3 mT (radial, xy) and 1.0 mT (axial, z).

The targeted shield coil was designed using the boundary element method implemented by Harris, C.T., *et al.* [8] with data for the MRI fringe field obtained from the manufacturer by a personal communication. A cylindrical ring of null-field targets extended 15 cm axially along the length of the 12-cm-long four-PMT module (1.5 cm buffer on either end) and extended from a radius of 8 cm (the face of the scintillator) to 14 cm (1 cm beyond the PMT). The distance between the centre of the MRI system and the PET system was chosen to be 1.7 m. While larger separations would reduce power requirements, the range of bed motion must be short enough for cables and supply lines to remain connected between PET and MRI scans. Field profiles and power requirements were analysed for a range of coil radii and lengths at various positions between the PET and MRI scanners. From among the approximately 100 candidate coils investigated, one design having low power requirements and good shielding was selected. The geometry of the proposed arrangement is shown in Figure 3.6.

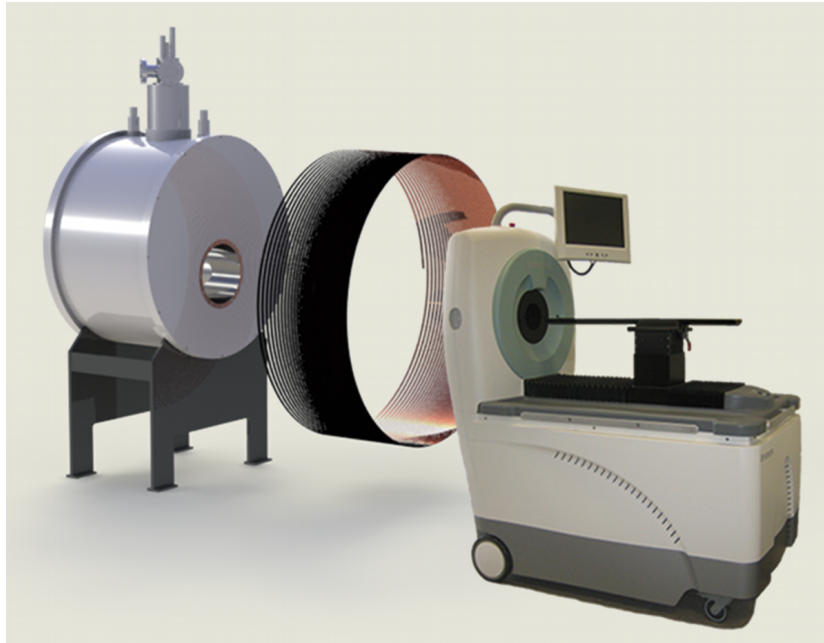


Figure 3.6: Geometry of the PET-MRI concept with active electromagnetic shielding. Shield coil windings are shown without the coil support structure.

The candidate shielding coil has radius 75 cm and length 60 cm and its front end is located 90 cm from the centre of the MRI system. The coil consists of a single layer of 34 variable-separation turns with a 10.7-mm minimum wire separation. The hollow wire to be used has 10x10-mm cross-section with a 5-mm-diameter liquid cooling channel. The characteristics of the shield coil are summarized in Table 3.1.

Table 3.1: Electromagnetic and physical characteristics of the candidate shield coil.

Characteristic	
Inductance	2.1 mH
Resistance	34 m Ω
Efficiency (average over null region)	0.016 mT/A
5 Gauss line (minimum radius)	2.2 m
Net force on coil (z-axis)	720 N
Mass (copper / total)	120 / 200 kg
Wire length	160 m
Current (DC)	460 A
Power	7300 W
Parallel cooling channels	4
Cooling water flow at 3.5 atm	130 cc/s
Temperature rise	14 °C

The proposed design successfully reduces the maximum magnetic field at the location of the detector PMTs from approximately 8 mT to better than 0.1 mT with the shield coil energized, lower than the required 1 mT limit. A plot of magnetic field as a function of distance for the cases with and without shielding is shown in Figure 3.7 and field maps showing the field in the detector before and after are shown in Figure 3.8. One suggested room layout based on room F5-122 in St. Joseph's Hospital in London, Ontario is proposed in Figure 3.9. This particular room has more floor space than is necessary for this approach.

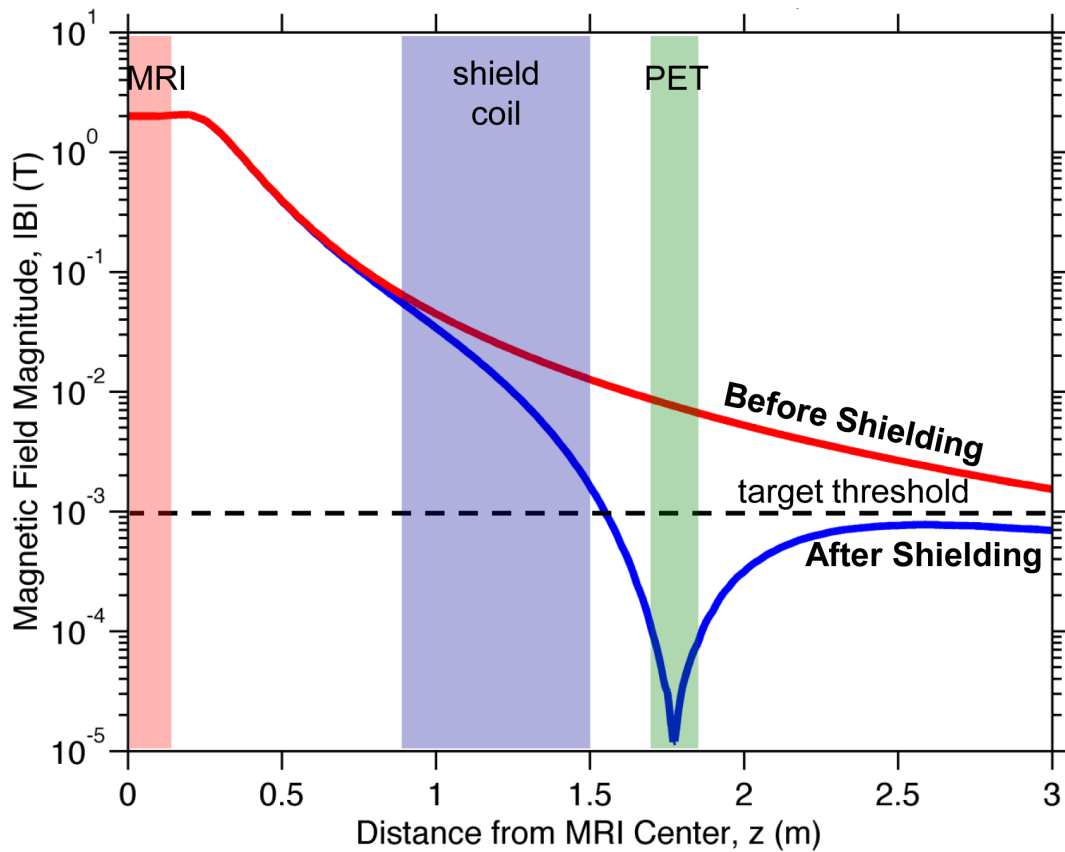


Figure 3.7: Plot of magnetic field magnitude as a function of distance from the centre of the MRI scanner at a radial distance $r = 10$ cm (the radial distance of the PMTs in the PET detector ring). The magnetic field magnitude at the PET detectors is reduced by two orders of magnitude when the shield coil is energized. The PET system can be moved up to 10 cm closer to the shield coil and any distance farther and still experience a magnetic field below the target threshold.

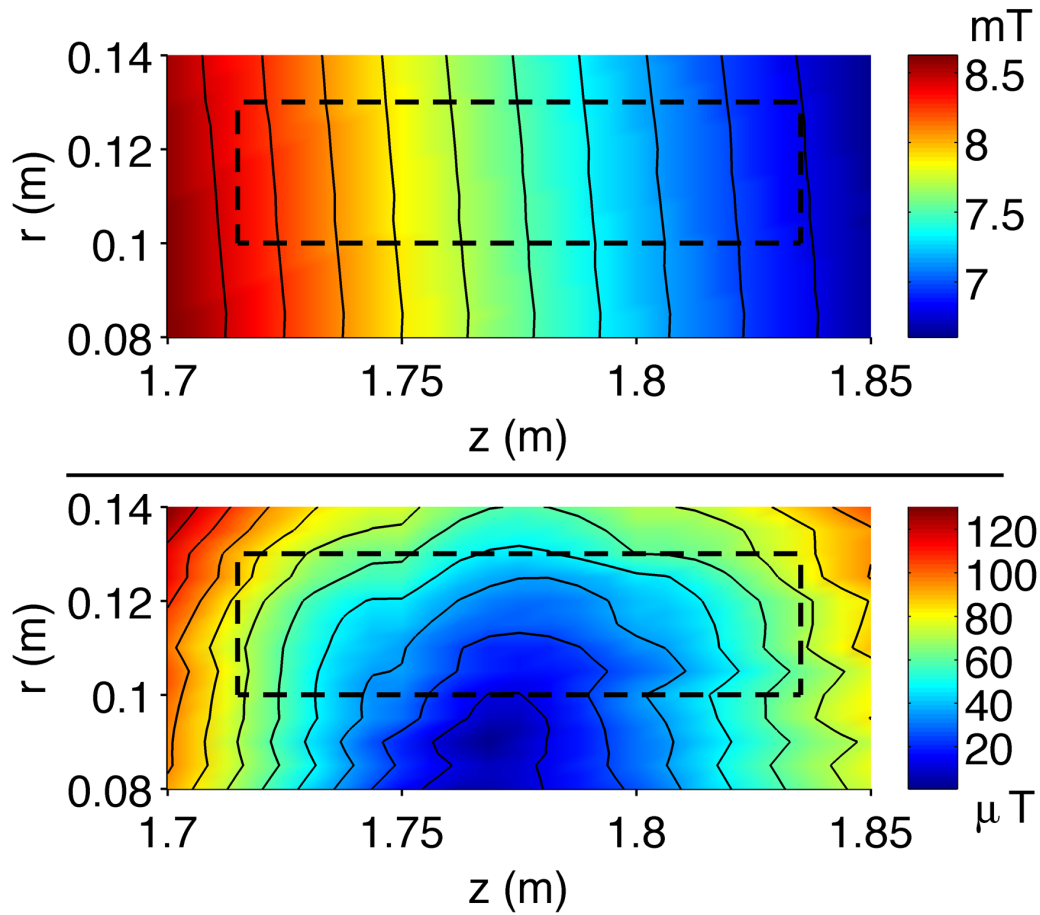


Figure 3.8: Magnetic field magnitude map in the vicinity of the PET detectors without shielding (top) and with shielding (bottom). Field data for the 2 T MRI was obtained from the manufacturer and field data for the coil was from a Biot-Savart Law model implemented in MATLAB which does not include the susceptibility of the PET detectors. Note that the colourmaps have different scales. The origin of the coordinate system is the MRI isocentre. The dashed line shows the location of the four PMTs that make up one module. To account for positioning error, the shield coil was designed to null the field over the entire region shown. The maximum magnitude field in the detectors was 8.2 mT without shielding and 0.08 mT with shielding. The jaggedness of the contour lines are due to coarse sampling.

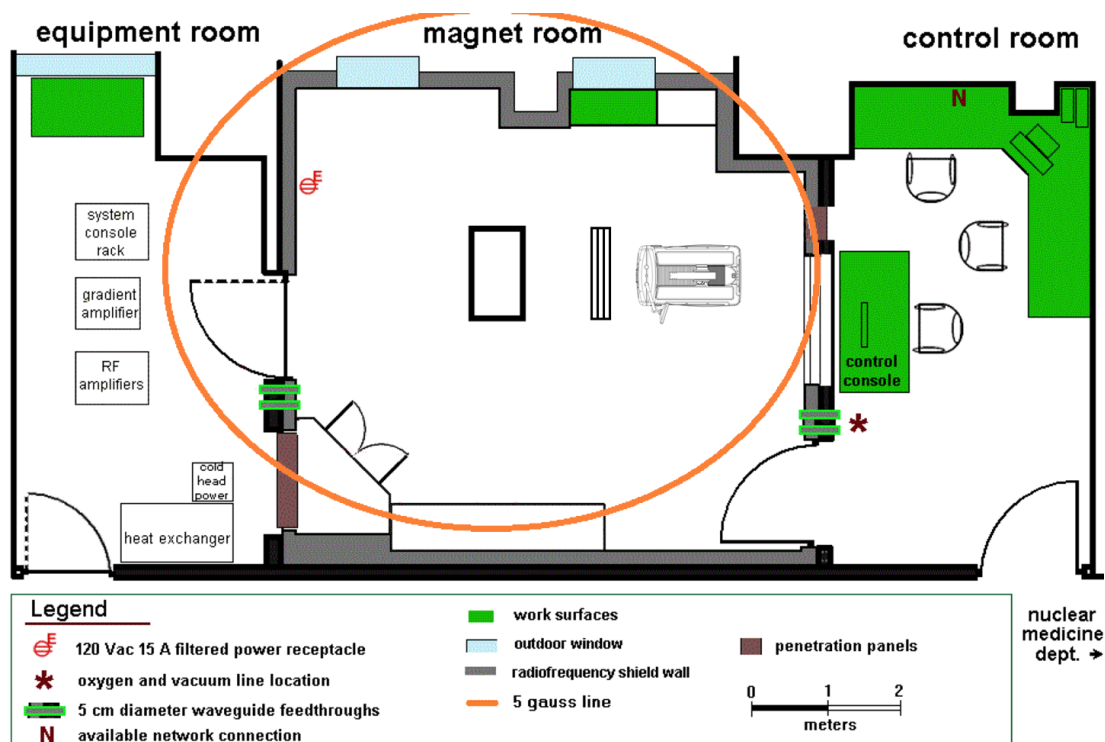


Figure 3.9: Proposed floor plan for the actively shielded PET system in the same room as the 2.0 T MRI system. The MRI scanner is represented by the box in the centre of the room. The shield coil (coil dimensions not to scale) is positioned between the Siemens Inveon PET and the MRI scanner. The 5 gauss line (0.5 mT line) is shown. In this arrangement, the PET system can be operated only when the shield coil is energized.

3.3.1.2 Discussion

The design study and simulations have shown that an actively controlled electromagnetic shield coil can be used to reduce the magnetic field in the close vicinity of a superconducting MRI system sufficiently to allow the normal operation of a Siemens Inveon PET. The shield would be energized during PET imaging and would be turned off during MRI acquisitions. Unlike most high-field

small animal MRI systems commercially available, the particular MRI scanner used in this study had no self-shielding and its fringe field is generally stronger than would be the case with a more modern scanner, even at much higher main field strengths. Despite this added difficulty, the power requirements for the coil are essentially equivalent to those of present-day insert gradient coil systems and would be acceptable for this application.

The primary challenge in the operation of this system is certainly expected to be interaction between the shield and the superconducting magnet. Additional flux from the shield coil in the MRI system may affect the stability of the main magnetic field. The allowed distance between the PET and MRI systems directly affects the shield requirements and further trade-offs are possible. It would also be possible to add a term in the algorithm cost-function that represents coupling between the shield and magnet. The result would be increased power deposition in the shield.

Several negative aspects of this approach include the added requirement for a separate power supply and chilled water source for the shielding electromagnet and the construction of the magnet itself. These aspects add to the cost and complexity of combining the Siemens Inveon in the same room as an MRI scanner. The main benefit is reducing the floor space requirements for the PET-MRI facility. When compared with simply separating the PET and MRI systems physically in the same room, this approach is worth considering primarily for facilities where only a small physical space is available for the PET-MRI imaging suite.

3.3.2 Separating the PET and MRI Scanners in the Same Room

For imaging suites with more physical space, it may be practical to arrange the PET and MRI systems so that the fringe magnetic field experienced by the PET detectors is weak enough that it does not affect PET performance. For the Siemens Inveon PET, the fringe field should be weaker than 1 mT (10 gauss).

3.3.2.1 System Description

There is no standard room size or facility arrangement for small animal MRI installations. In this section, I describe two options for the floor plan of a PET-MRI facility using the 2.0 T unshielded MRI scanner in St. Joseph's Hospital (London, Ontario) Room F5-122 based on fringe field data from the manufacturer. I also propose arrangements for installing the Siemens Inveon PET in a typical high-field 9.4 T shielded MRI facility. The model for the 9.4 T suite was the CFMM facility at Robarts Research Institute (London, Ontario) Rooms 130-133.

For the laboratory at St. Joseph's Hospital, one arrangement where the PET and MRI systems are oriented along a common axis is proposed in Figure 3.10. The field profile, shown in Figure 3.11, demonstrates that for the maximum centre-to-centre separation of 5.2 m, the field is below 0.3 mT. For a fringe field magnitude of 1 mT, the systems can be brought closer together to a separation of 3.5 m.

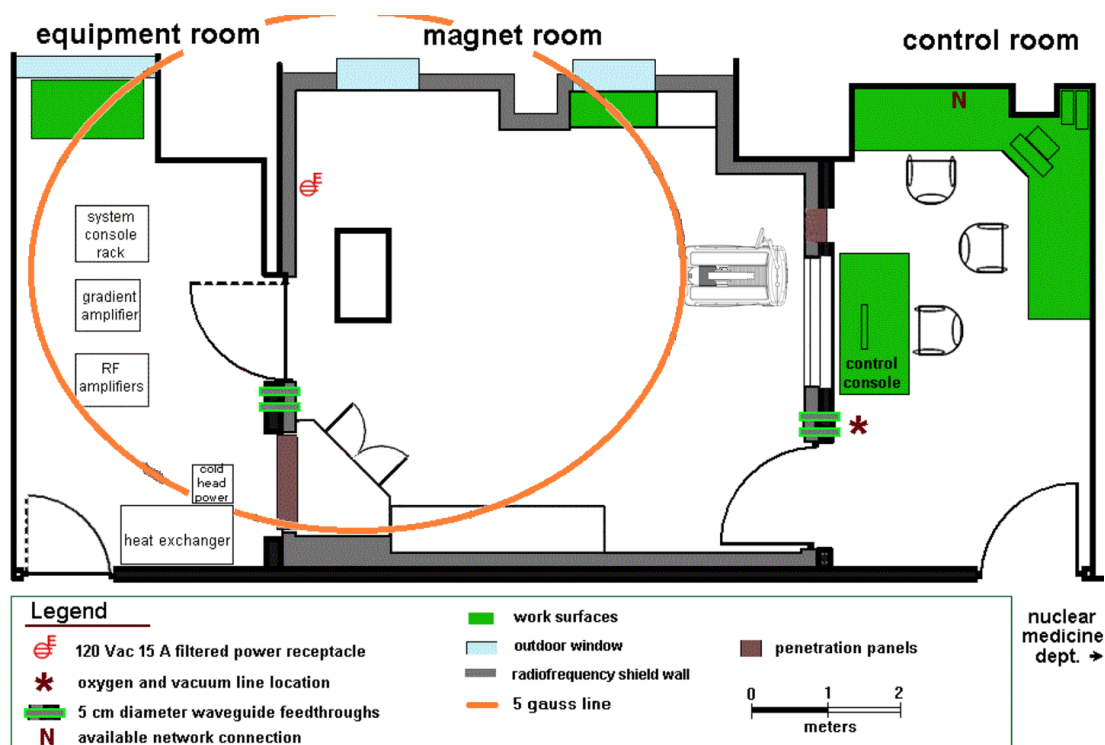


Figure 3.10: Proposed floor plan for the PET system in the same room as the 2.0 T MRI system. The MRI scanner, represented by the box, is positioned as far as the room size allows from the PET system. The 5 gauss line (0.5 mT line) is shown.

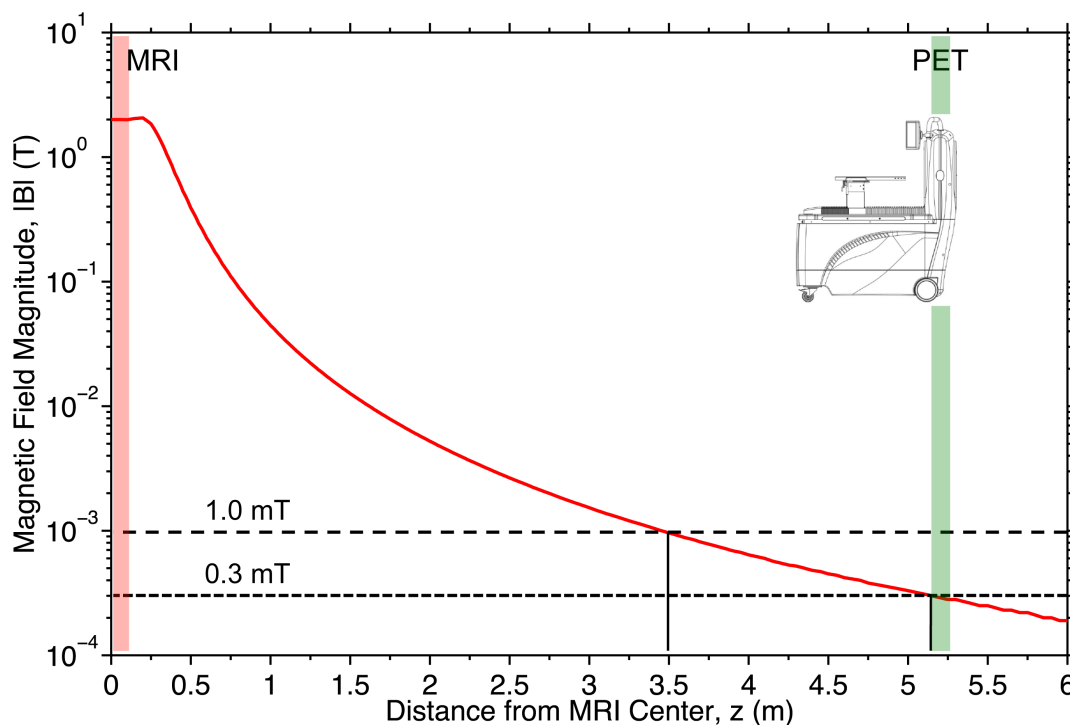


Figure 3.11: Simulated magnetic field magnitude as a function of distance for the PET-MRI arrangement shown in **Figure 3.10**. For this geometry, the magnetic field direction is primarily in the axial direction with respect to the PET system.

A side-to-side arrangement is also possible given the floor layout in the laboratory at St. Joseph's Hospital. The floor plan is shown in Figure 3.12 and a photograph of the proposed arrangement is shown in Figure 3.13. The field profile is shown as a function of radial distance in Figure 3.14. While the magnetic field would vary slightly across the PET detector ring in this geometry, the magnitude of the fringe field is, in general, weaker in the radial direction and the PET system can be placed closer to the MRI system than would be the case if the scanners were aligned in a collinear manner. At the maximum separation allowed by the size of the room (approximately 5 m centre-to-centre), the field would be approximately

0.2 mT in the PET detector ring. For a 1mT field at the PET detectors, the systems can be brought to approximately 2.9 m centre-to-centre.

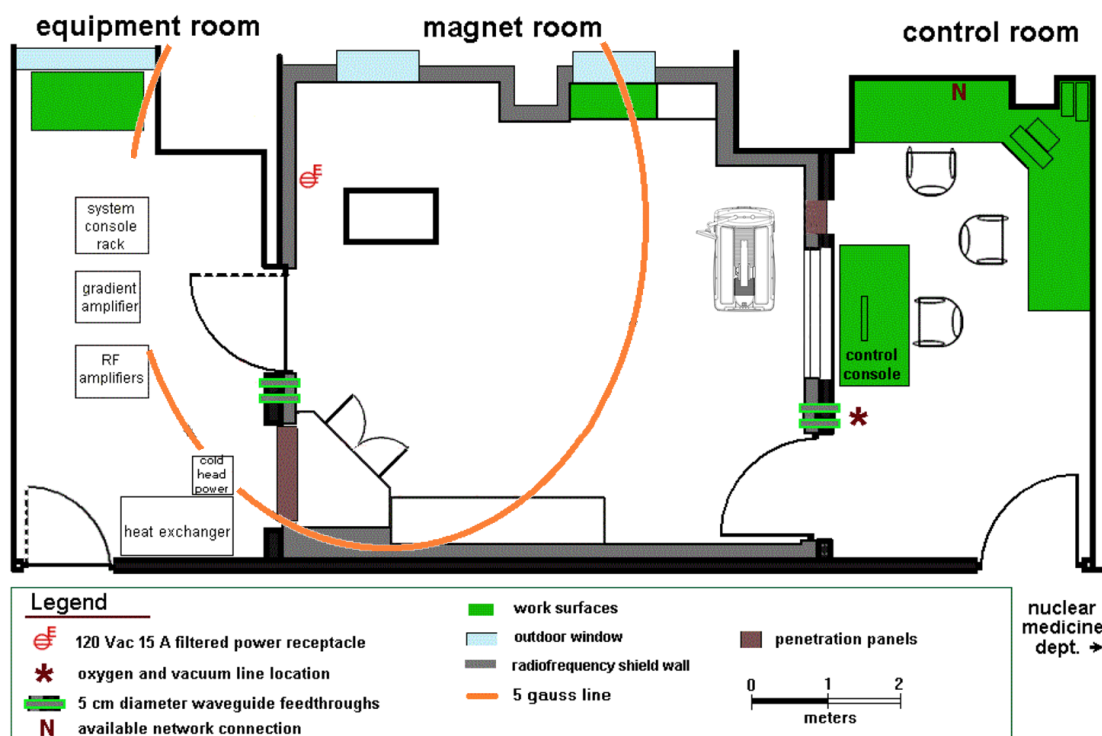


Figure 3.12: Alternative side-by-side floor plan for the PET system in the same room as the 2.0 T MRI system. The MRI scanner, represented by the box, is oriented parallel to the PET scanner separated by a certain radial distance. The 5 gauss line (0.5 mT line) is shown.

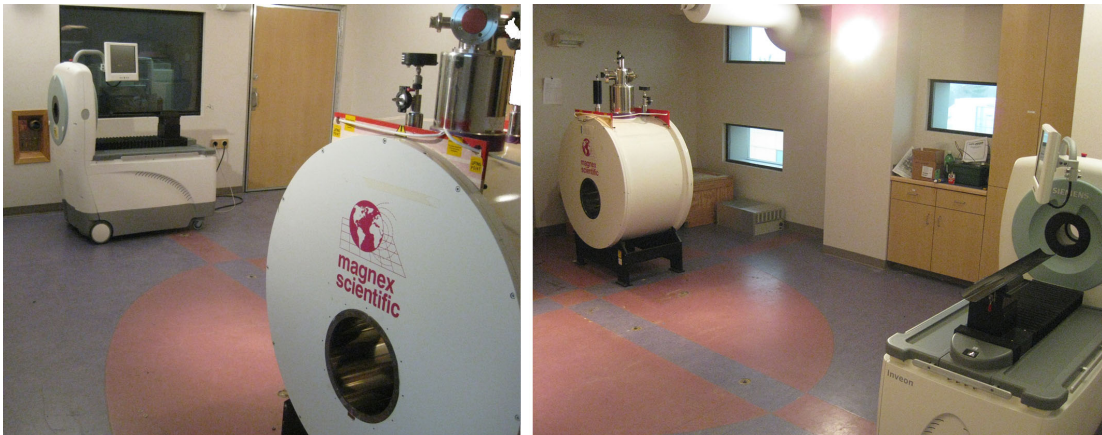


Figure 3.13: Photographs of the PET-MRI scanning room showing the room geometry. The PET and MRI systems are placed on opposite sides of the room.

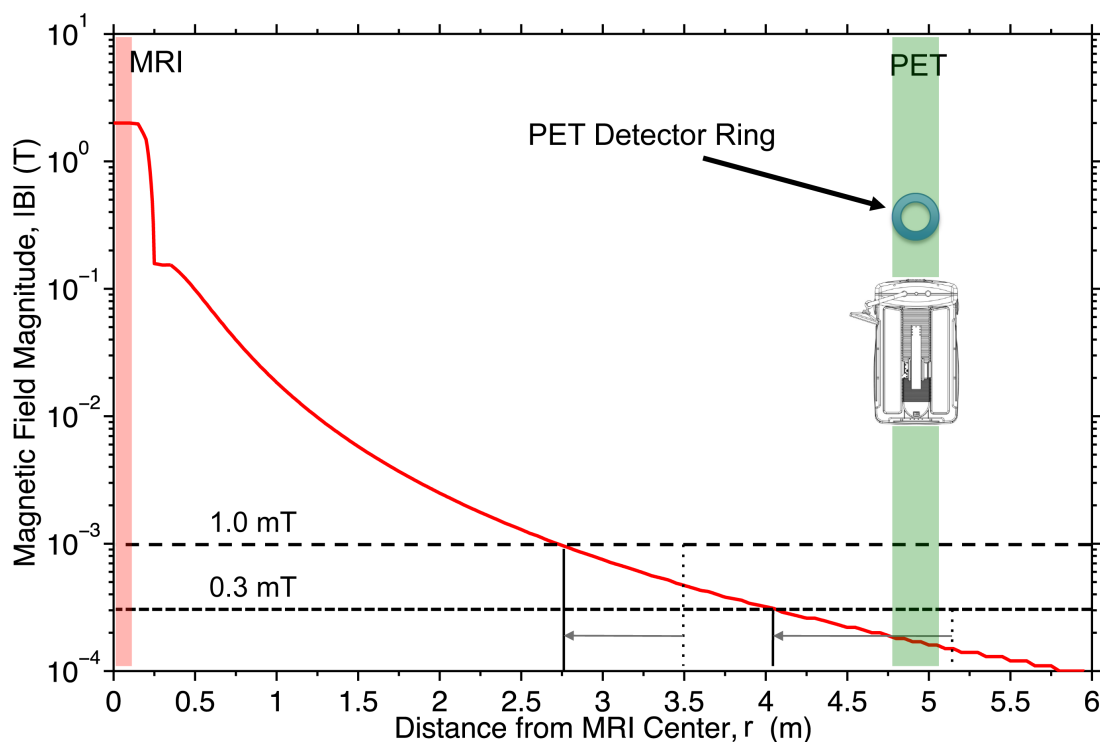


Figure 3.14: Simulated magnetic field magnitude as a function of radial distance for the side-by-side PET-MRI arrangement shown in **Figure 3.12**. Similar to the axial collinear geometry, the magnetic field direction is also primarily in the axial direction with respect to the PET system; however, the magnitude of the field varies across the PET detector ring. For comparison, the grey dashed lines show the (axial) distances of the 0.3 mT and 1 mT field lines and the difference is shown by the arrow.

For the high-field small animal MRI scanner, it was also possible to find locations within the facility for the Siemens Inveon PET where the fringe field is weaker than 1 mT (10 gauss). One option where the PET system is placed in a nearby room is shown in Figure 3.15 and another option where the PET system is inside the MRI room is shown in Figure 3.16.

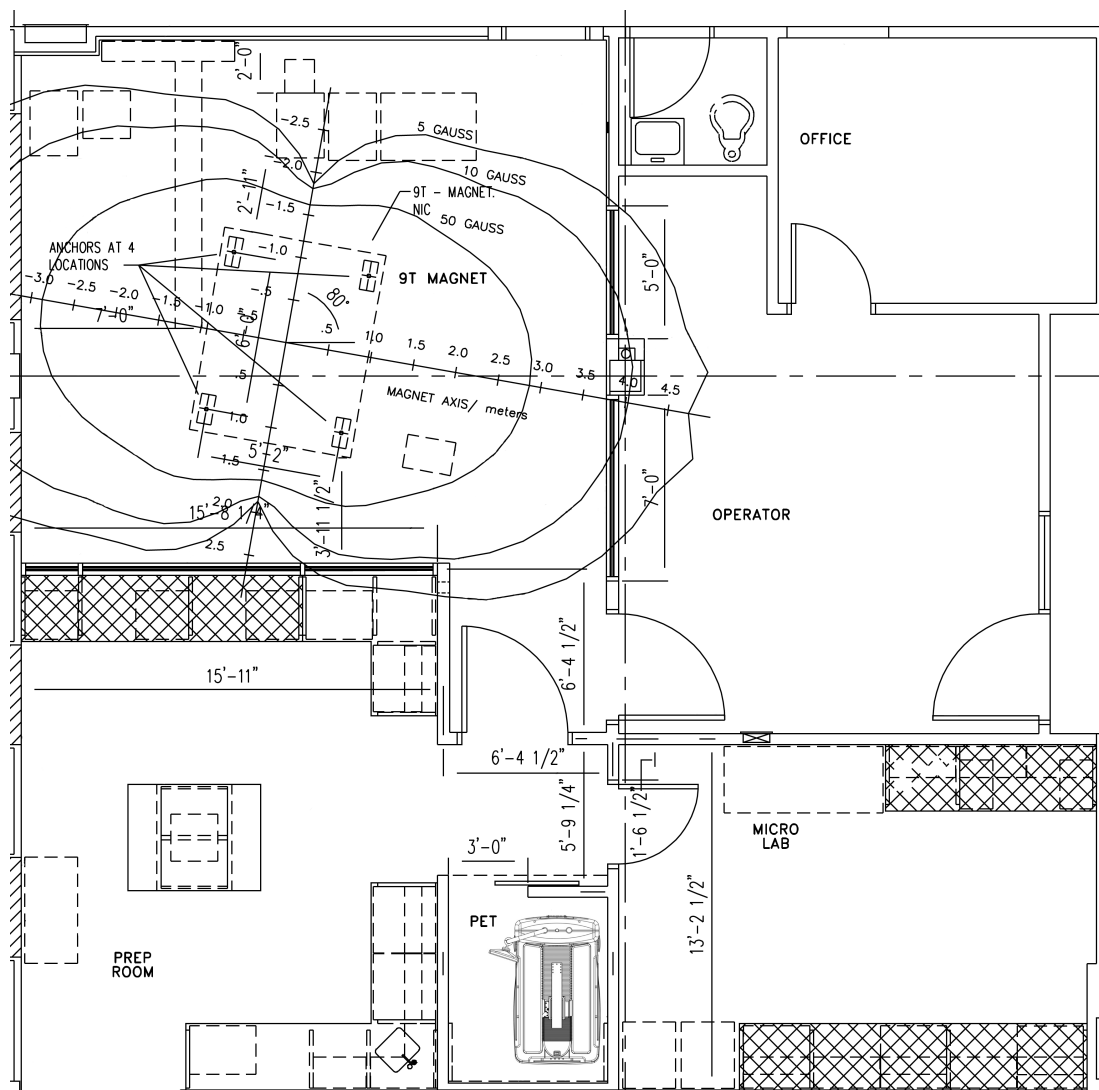


Figure 3.15: Proposed floor plan of a PET-MRI facility in a typical 9.4 T MRI suite with the PET system located in a separate area but part of the same imaging suite. The magnetic field experienced by the PET system is negligible in this location.

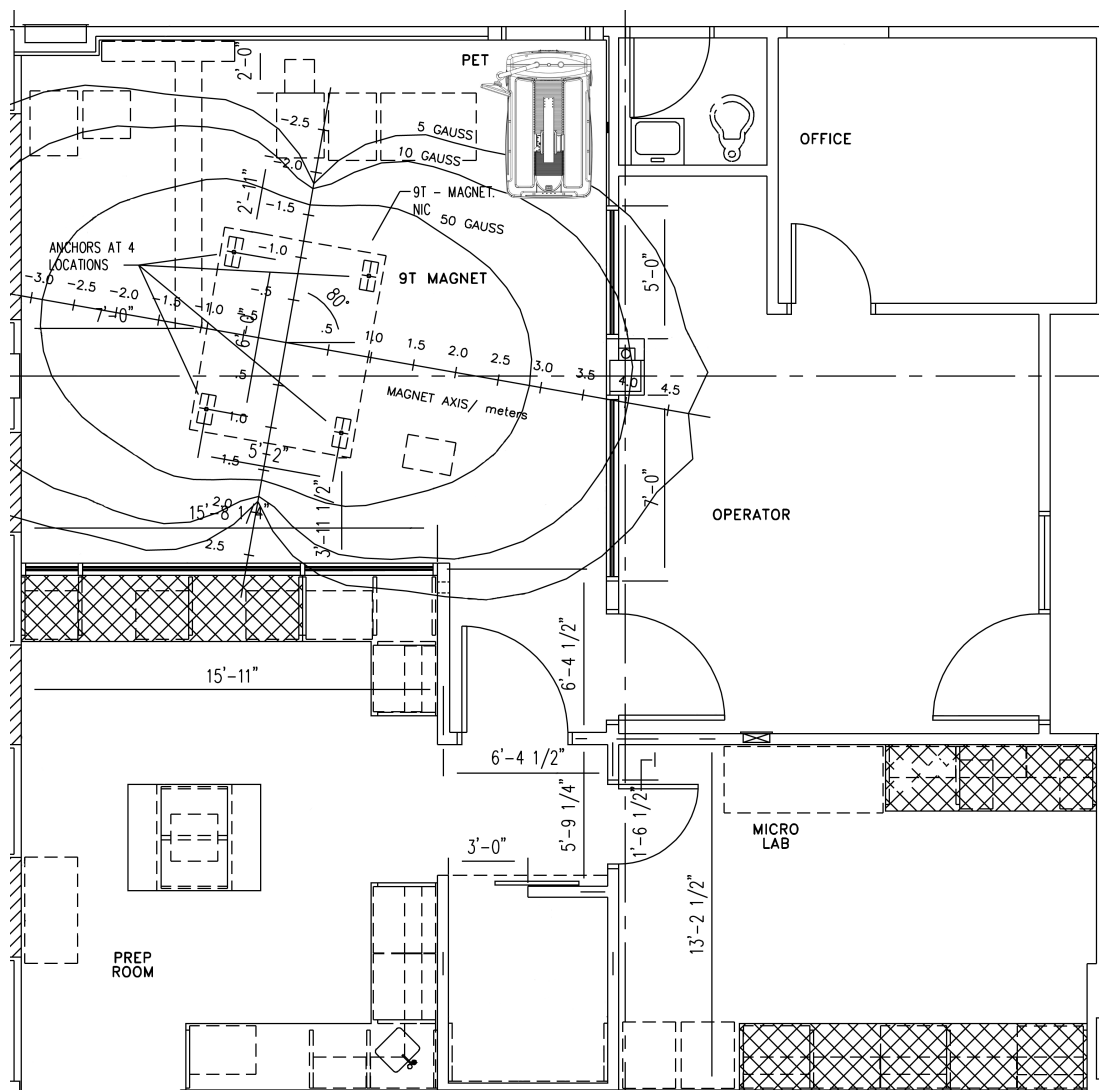


Figure 3.16: Alternative floor plan for a PET-MRI facility in a typical 9.4 T MRI suite with the PET system in the same room as the MRI system. At this location, the PET detectors would experience a magnetic field of approximately 0.1 mT.

3.3.2.2 Discussion

The fringe field map surrounding superconducting MRI systems at two facilities indicated that there were locations having field magnitude below 1 mT. This shows that external magnetic fields would not preclude installing the Siemens Inveon PET in the same room as a superconducting MRI for the imaging

laboratory layouts studied. To prevent RF interference from the PET system, an RF bottle should be used with the MRI scanner.

Like the other approaches discussed in this chapter, for this arrangement, precise PET and MRI image co-registration can be achieved by using a common animal bed for both modalities that can be moved reproducibly to the exact same position within each modality. All hoses should connect at the rear so that the bed can be removed and transported without disconnecting heating or anaesthetic lines. These lines should connect to anaesthetic and heating equipment on a mobile cart that can be moved between scanners. To make use of the precise position control required for transmission scans, the bottom of the bed should clamp onto the motion control mechanism of the PET system. The bed should also slide into an RF coil inside the MRI bore where a set of stoppers would ensure precise and reproducible axial positioning. PET and MR images could then be co-registered in software using a pre-set rigid-body transformation. Following animal preparation, the typical scanning workflow would be to acquire MR images, remove the bed, carry it over to the PET system, perform a transmission scan for attenuation correction, inject radioisotope and finally acquire PET data.

When moving the PET system into place, it would be advisable to tether the scanner to a wall to reduce the risk of strong forces causing projectile motion. The PET system should also be chained or bolted securely to the wall or floor once it is in its permanent position to prevent anyone from moving the scanner accidentally. In concern for MR safety, some sort of physical barrier separating the two systems with a gate is recommended where possible. The barrier would act as a reminder of the magnetic field danger for individuals working around the

PET scanner and would reduce the risk of accidentally bringing non-MR-compatible tools or equipment close to the MR system. Such a barrier would be practical in the proposed arrangement at St. Joseph's Hospital, where there may be a large fraction of the room that is outside the 5 gauss line that can be accessed from the main room entrance.

When compared with the other techniques described in this chapter, the appeal of this approach lies in its simplicity, its low cost, its lack of major additional hardware, and requiring no software or hardware modifications to PET or MRI systems other than a multimodality animal bed. This method would be the easiest to implement at other institutions, provided the MRI facility has a large enough space that the PET system can be placed in a location with low field. The context of the approach described here was high-field superconducting MRI scanners; however, several vendors are now offering small animal MRI systems based on permanent magnets or low-field superconducting magnets having very weak fringe field profiles. For such MRI systems, the Siemens Inveon PET could be placed immediately adjacent to the MRI scanner [9].

3.4 References

1. Matter NI, Scott GC, Venook RD, Ungersma SE, Grafendorfer T, Macovski A, Conolly SM. Three-dimensional prepolarized magnetic resonance imaging using rapid acquisition with relaxation enhancement. *Magnetic Resonance in Medicine* 2006;56(5):1085-1095.
2. Gilbert KM, Scholl TJ, Handler WB, Alford JK, Chronik BA. Evaluation of a Positron Emission Tomography (PET)-Compatible Field-Cycled MRI (FCMRI) Scanner. *Magnetic Resonance in Medicine* 2009;62(4):1017-1025.
3. Peng H, Handler WB, Scholl TJ, Simpson PJ, Chronik BA. Proof-of-principle study of a small animal PET/field-cycled MRI combined system using conventional PMT technology. *Nucl Instrum Methods Phys Res Sect A* 2010;612(2):412-420.
4. Mao RH, Zhang LY, Zhu RY. Optical and Scintillation Properties of Inorganic Scintillators in High Energy Physics. *IEEE Transactions on Nuclear Science* 2008;55(4):2425-2431.
5. Zaidi H, Ojha N, Morich M, Griesmer J, Hu Z, Maniawski P, Ratib O, Izquierdo-Garcia D, Fayad ZA, Shao L. Design and performance evaluation of a whole-body Ingenuity TF PET-MRI system. *Physics in Medicine and Biology* 2011;56(10):3091-3106.
6. Cho ZH, Son YD, Kim HK, Kim KN, Oh SH, Han JY, Hong IK, Kim YB. A hybrid PET-MRI: An integrated molecular-genetic imaging system with HRRT-PET and 7.0-T MRI. *International Journal of Imaging Systems and Technology* 2007;17(4):252-265.
7. Kawasaki Y, Bertaina ME, Sakaki N, Shimizu HM, Inoue N, Hasegawa S, Ohtsu I, Adachi T, Ebisuzaki T, Hirota K *and others*. Performance of a multi-anode photomultiplier employing a weak electrostatic focusing system (Hamamatsu R8900 series). *Nuclear Instruments & Methods in Physics Research Section a-Accelerators Spectrometers Detectors and Associated Equipment* 2006;564(1):378-394.
8. Harris CT, Handler WB, Chronik BA. Electromagnet design allowing explicit and simultaneous control of minimum wire spacing and field uniformity. *Concepts in Magnetic Resonance Part B-Magnetic Resonance Engineering* 2012;41B(4):120-129.
9. Schmid A, Schmitz J, Mannheim JG, Maier FC, Fuchs K, Wehrl HF, Pichler BJ. Feasibility of sequential PET/MRI using a state-of-the-art small animal

PET and a 1 T benchtop MRI. *Molecular Imaging and Biology* 2013;15(2):155-165.

Chapter 4

4 First Image from a Combined PET and Field-cycled MRI System¹

In this demonstration, two PMT-based PET detectors were integrated with a field-cycled MRI system by placing them into an axial gap. The first multimodality images from the combined PET and field-cycled MRI system demonstrate the potential of this approach to combining PET and MRI.

4.1 Introduction

Modalities such as MRI and CT yield excellent contrast and resolution for visualizing anatomy, while positron emission tomography (PET) gives localized information about biochemical processes. There is significant interest in combining anatomical and functional information [1].

There are three ways to acquire multimodality images: One can do this with physically separate systems and combine the information using image registration techniques after the fact. Another way is to integrate two systems sharing a common bore axis with a bed that moves between the two fields of view for sequential imaging (for example, PET/CT, which is now widespread [1]). Finally, one can do this in a fully integrated manner where the imaging regions of the two

¹ A version of this chapter has been published: First image from a combined positron emission tomography and field-cycled MRI system. Bindseil GA, Gilbert KM, Scholl TJ, Handler WB, Chronik BA. *Magn Reson Med*. 2011 Jul;66(1):301-5.

systems coincide, acquiring data either completely simultaneously or in an interleaved fashion.

Of these three ways, the fully integrated approach is preferable because it would allow motion correction for the functional data [2] and would enable the user to track dynamic processes using both modalities [3]. Motion correction is significantly limited with sequential imaging sequences such as those used in PET/CT studies. Completely simultaneous imaging is important for studying physiological processes that occur quickly relative to the speed of the imaging method. Interleaved imaging is acceptable when the processes are relatively slow, and can generally provide motion correction when the movement or deformation occurs. Another unique advantage of simultaneous imaging is the ability to study processes that are not repeatable, such as those involving learning [4].

Unlike PET/CT, combining PET with MRI allows completely simultaneous or interleaved multimodality imaging. Other important advantages of PET/MRI over PET/CT include reduced total radiation dose and superior soft tissue contrast [5]. For small-animal imaging, the reduction in radiation dose can be substantial, thus enabling serial and longitudinal studies [6]. Improved soft tissue contrast is significant since PET studies typically involve functional analysis of soft tissue.

While PET/MRI offers numerous benefits, a serious technical challenge to combining the two modalities exists: Conventional PET detectors based on photomultiplier tubes (PMTs) cannot operate in the environment of the strong magnetic fields of an MR scanner. As a result, PET/MRI is currently an area of

active research and development and only a limited number of prototypes exist [4,7,8].

Simultaneous PET/MRI would require specialized PET detectors that are compatible with conventional static-field MRI systems. One such approach employs optical fibres to relay scintillation light from crystals inside the scanner to PMTs located in the fringe field [9-12]. A similar method uses an actively shielded split superconducting magnet with optical fibers guiding scintillation light out radially to a ring of PMTs in the fringe field [13]. These approaches generally preserve MRI performance; however, PET detection efficiency is reduced due to a loss of scintillation light from the limited coupling to the optical fibres. Another promising approach for simultaneous PET/MRI uses semiconductor-based detectors, such as avalanche photodiodes or silicon photomultipliers, which are unaffected by magnetic fields [3,14-16]. In principle, PET systems based on semiconductor-based detectors can achieve similar performance to PMT-based systems; however, semiconductor-based systems are still in the early stages of development and are not yet widely available. Recent approaches to small-animal PET/MRI using semiconductor-based detectors inserted into the magnet bore have had low absolute PET sensitivity when compared to commercial PMT-based systems due primarily to the limited radial space budget which places constraints on the thickness of the scintillation crystal [14].

Interleaved imaging could be accomplished using conventional PMT-based detectors if the MR system were itself time-varying, such as with field-cycled MRI [17-20] based on resistive electromagnets, where the main magnetic field can

be rapidly cycled off in 30 ms. Conventional PMTs can operate normally during the times when all magnetic fields are off. This approach would have the advantage of using existing, well-characterized PET detector systems.

One common form of field-cycled MRI, called prepolarized MRI, uses two independent magnets. The strong polarizing magnet produces the initial magnetization of the sample. Then, standard MR imaging is done in the environment of a lower-strength readout field with high spatial and temporal uniformity. Field-cycled MRI systems can produce images of comparable quality to clinical superconducting systems [20]. In addition to its PET compatibility, field-cycled MRI can offer unique benefits over traditional MRI. One such advantage is the ability to dynamically vary the magnitude of the main field, offering novel T_1 -dispersion contrast [21]. Other benefits include: significantly reduced susceptibility artifacts, the ability to image around metallic implants [22]; substantially reduced specific absorption rate (SAR) due to low radiofrequency (RF) power requirements; and silent gradient operation resulting from imaging at low-field.

In this note, we report on our work in implementing and demonstrating the first PET/MRI system for interleaved operation based on a field-cycled MRI platform. We present the first dual-modality image generated on such a system. The intention was to demonstrate the feasibility of this approach to combining PET and MRI.

4.2 Methods

A field-cycled MRI system with a 9-cm axial gap for the insertion of a group of PET detectors near the isocenter of the scanner was used to generate MR images [17]. The polarizing and readout magnets were pulsed to fields of 0.3 T and 94 mT, respectively. The system had a full set of first- and second-order shim coils to compensate for the reduced homogeneity introduced by the gap and the susceptibility of the PET detectors. The imaging regions of the PET and field-cycled MRI systems were coincident, permitting both PET and MR data to be acquired without movement of the subject. The system geometry is shown in Figure 4.1. A complete description of the field-cycled MRI system and its operation appears in reference [17]. All imaging was performed with an 8.3-cm-diameter low-pass birdcage RF coil driven in quadrature and tuned at 4.0 MHz. The field-cycled MRI system was interfaced to a Varian Unity Inova console for image acquisition.

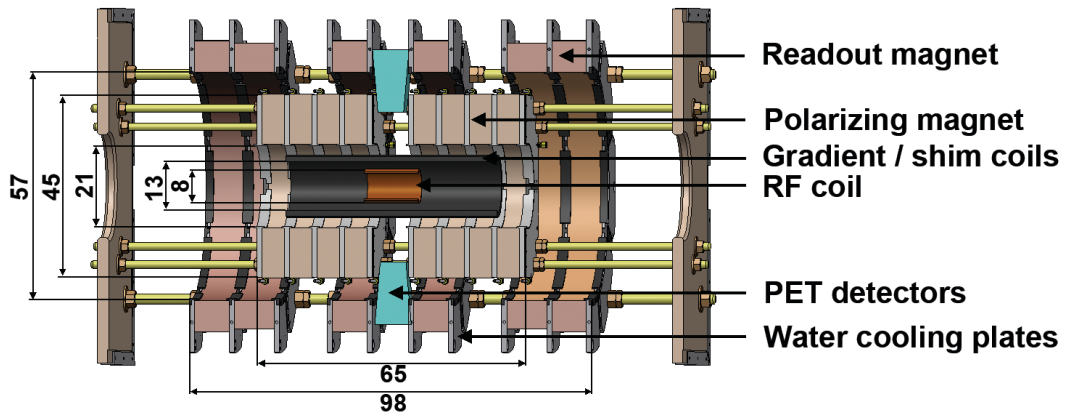


Figure 4.1: Schematic of PET detectors in field-cycled MRI system. The two PET detectors are located in the axial gap. All dimensions shown in centimeters.

The PET system consisted of two blocks of detectors connected through an RF-shielded feed-through panel to a CAEN coincidence detection system (Viareggio, Italy) located outside the RF shed. Each PET detector block, obtained from a decommissioned Siemens-CTI ECAT 951 clinical system, consisted of four PMTs optically coupled to a block of bismuth germanate scintillator and housed within a mu-metal enclosure. The scintillation crystal was cut into an array of 8x8 fingers, each having a pitch approximately $6.2 \times 5.6 \times 30 \text{ mm}^3$ along the axial-, azimuthal- and radial-directions, respectively, when defined with respect to the centre of the field of view (FOV). In conventional fashion, each crystal finger in the array is cut to various depths so that scintillation light is shared among the four PMTs in a way that permits the identification of the position of gamma ray interactions post-acquisition by Anger logic [23]. Signals from each PMT were amplified by a custom pre-amplifier and output to an acquisition system that recorded energy and timing information of coincidences. The efficiencies of the 64 crystal fingers in each detector were normalized by analyzing flood data acquired by attaching a point source to the opposing detector. The spatial sensitivity of the PET system was highest at the isocenter and decreased rapidly with increasing radial distance due to the two-detector geometry.

The feasibility of simultaneously acquiring PET and MR images was tested using a PET/MRI phantom. The phantom consisted of a triangular arrangement of positron-emitting point sources (Na-22, 2.6-year half-life, 0.11-MBq total activity, 10-mm separation between sources, 1-mm diameter per source, triangular casing with 2.54-cm side-length) embedded in an onion. The phantom was placed at the centre of the FOV of both systems.

To acquire all lines of response for the PET data with only two detectors, it was necessary to manually rotate the phantom (including the RF coil) in 12 steps of 15° each and combine the PET data post-acquisition. For consistency across all phantom rotation angles, PET and MR data were acquired at each rotation step in an interleaved sequence as shown in Figure 4.2. Each interleaving cycle began with a polarization and readout interval lasting 1252 ms followed by a PET acquisition interval of 950 ms. During MR operation, incoming signals to the PET detection hardware were rejected. All magnets were off and no PET data were recorded during intervals of 500 ms before and 50 ms after PET acquisition. Thus, the repetition time (TR) for the combined PET/MRI sequence was 2752 ms. A total of 83 s of PET data were recorded at each rotation angle. The MR image from only the first rotation angle was kept.

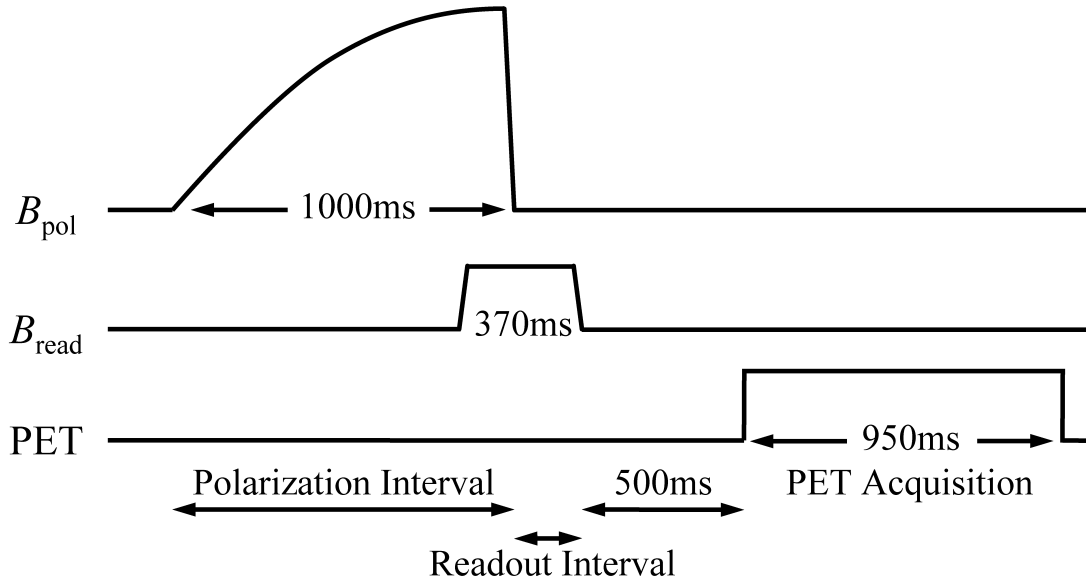


Figure 4.2: Timing diagram for interleaved sequence of field-cycled MRI and PET. B_{pol} provides the initial polarization, and all MR imaging is done during the readout

interval. After a delay of 500 ms, PET data acquisition is started. The sequence repeats after a TR of 2752-ms. Relative pulse magnitudes and timing are to scale.

PET data were filtered using a 300-700 keV energy window and a 50-ns coincidence-timing window, yielding approximately 15,000 coincidence detections per rotation angle. The sinogram was generated by stitching together the data from the different rotation steps. The geometry of the detector allowed for a sinogram of 15 equally-spaced distance bins and a total of 85 angle bins, for a single axial slice without rebinning. The sinogram was zero padded to 31 distance bins. The sinogram was reconstructed using filtered back-projection with a ramp filter and without attenuation correction. Two iterations of smoothing by linear interpolation using the MATLAB function `interp2` were applied to the image for ease of viewing. Image results are also shown for nearest neighbour interpolation. These interpolation methods increase the number of pixels but do not alter the spatial resolution of the PET image. The PET image was then scaled to match the dimensions of the MR image and superimposed.

4.3 Results

Figure 4.3 shows the original PET image reconstructed using either linear or nearest-neighbour interpolation in the back-projection step. Also shown are the images after smoothing by linear interpolation.

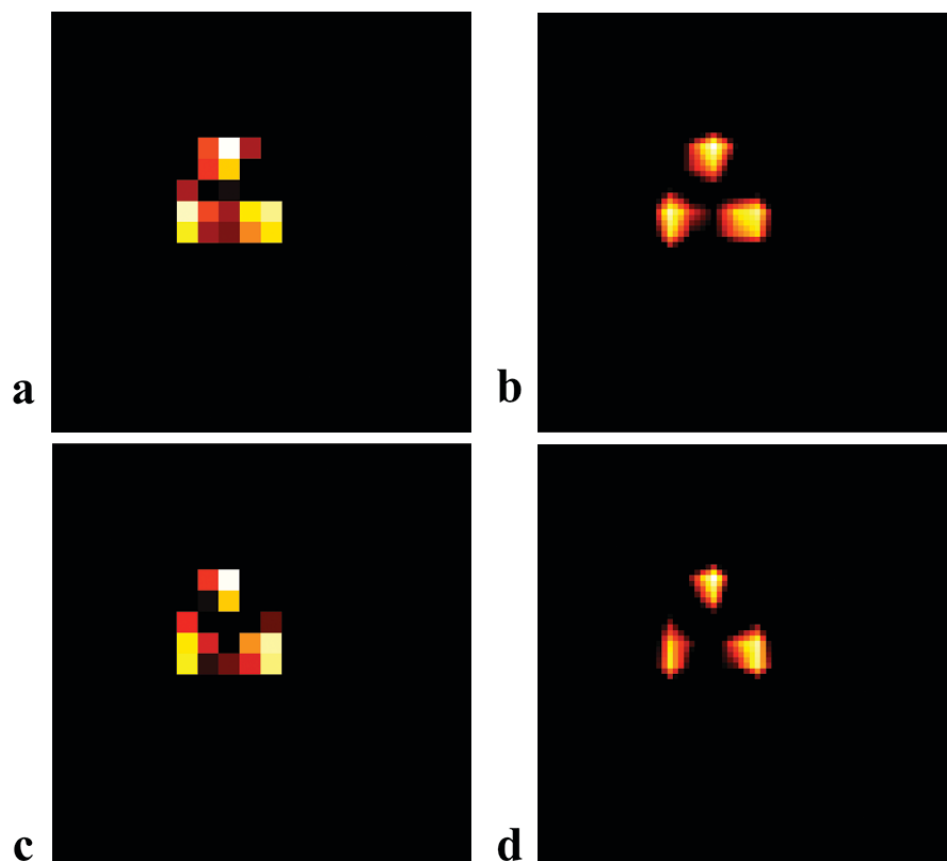


Figure 4.3: PET image reconstructed using linear interpolation for back-projection in the original resolution (a) and after smoothing (b). The same sinogram was reconstructed using nearest-neighbor interpolation for back-projection and is shown before smoothing (c) and after smoothing (d). Smoothing was performed by applying two iterations by linear interpolation as an aid in visualization on account of the coarseness of the pixels in the original image.

Figure 4.4 shows the PET and MR images as well as the superposition of the PET and MR images acquired in an interleaved manner on the combined PET and field-cycled MRI system. No artifacts are apparent in the PET image and no significant ghosting or phase encoding artifacts appear in the MR image. Additionally, the solid radioactive sources do not appear to have produced

susceptibility artifacts in the MR image; this is due to the low readout field of the FCMRI system.

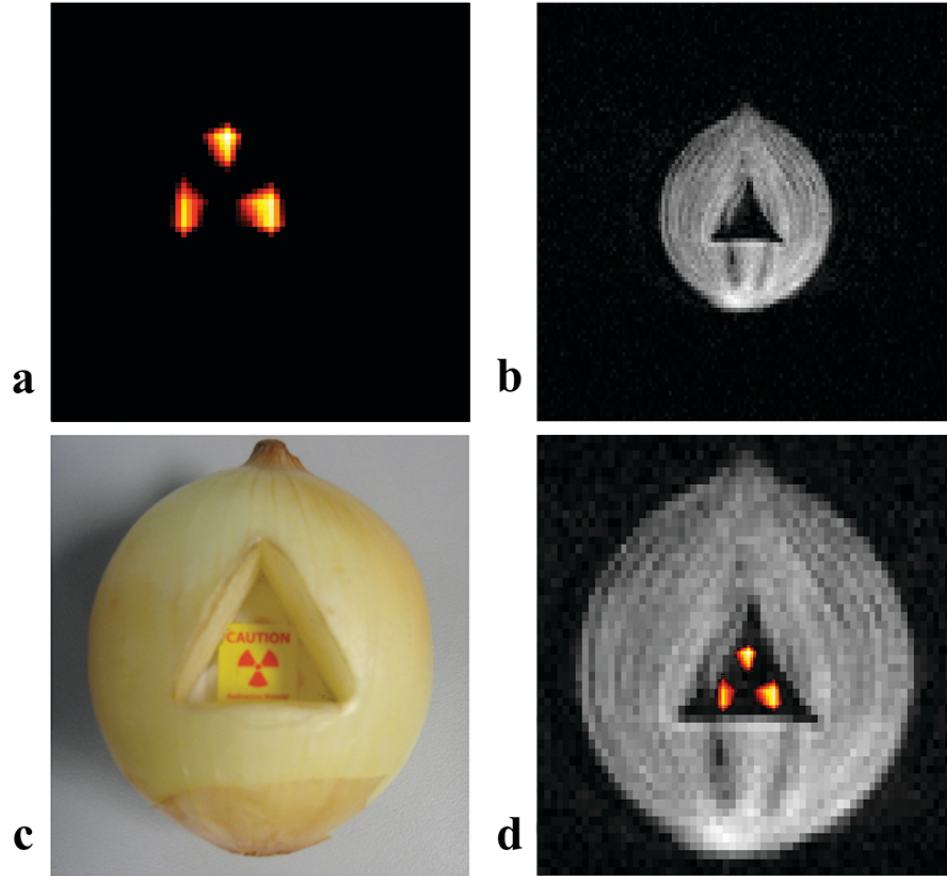


Figure 4.4: Smoothed nearest-neighbor PET image (a) and MR (b) image (not to scale). (c) Photograph of the phantom showing radioactive sealed source inside onion. The triangular cavity cuts through the entire onion. (d) Superimposition of PET onto MR image. The PET image was resized so that the separation between PET peaks was 10 mm in MR image space. MR imaging parameters: three-dimensional fast spin-echo; bandwidth = 20.03 kHz; FOV = 10 x 10 x 2 cm; echo train length = 8; $N_{\text{avg}} = 6$; Imaging matrix = 192 x 128 x 6; TR/TE = 2752 ms/21 ms; $T_{\text{scan}} = 32$ min; view = single transverse slice. Here, TR and T_{scan} include PET acquisition stages.

Layers of the onion are apparent in the MR image. On the reverse side of the triangular source, a small section of onion protruded into the interior of the triangular hole and is visible in the top left edge of the hole in the MR image. The three point sources are readily distinguishable in the PET image.

4.4 Discussion and Conclusions

The dimensions of the detectors limit resolution in PET. The crystal arrays in the human-scale clinical detectors used in this experiment are coarse compared with those typical of modern small-animal PET detectors, resulting in less precise position determination. A next-generation combined modality imager based on this approach would employ a ring of PET detectors optimized for a smaller FOV and a higher resolution.

A systematic source of noise in the PET image arises when coincidence data are reconstructed using only two detectors. In this case, the centre of the FOV is oversampled compared with off-axis positions. This effect occurs because the number of possible lines of response decreases as the distance from the centre of the imaging region increases, resulting in a radial shading in the reconstructed image. The spatial sensitivity of the PET image was corrected by appropriately weighting parts of the sinogram based on the geometry of the detection scheme. This normalization has the effect of amplifying the noise away from the centre of the image. The lower right point source in the PET image was closest to the centre of the FOV where the sensitivity is twice that of the positions of the other two point sources.

The presence of mu-metal-encased PET detectors in the gap of the field-cycled MRI system reduces the homogeneity of the readout field. However, since all imaging takes place at low field, distortions from readout field inhomogeneity are small. Nevertheless, removing the mu-metal shielding would improve field homogeneity in future experiments.

The acquisition time for the imaging sequence used in this experiment could be improved with a significant reduction of the 500-ms delay that preceded the PET acquisition stage. Magnetic field pulsing tests on linear and mesh PMTs have shown recovery to normal operation within several milliseconds of the field being turned off, with no long-term effects and that PET images produced by the detectors used in this experiment show no discernable degradation when the data are acquired interleaved with a strong magnetic field compared with a zero-field acquisition [24].

Although multimodality imaging was done in an interleaved manner, it is also possible to acquire PET and MR data in a sequential order as in Figure 4.5. Sequential imaging may be appropriate in animal PET studies where radioisotope is injected intraperitoneally and significant tumour uptake begins to occur tens of minutes after injection [25]. In such a study, MR images could be acquired during the initial uptake period after which PET data could be acquired without moving the animal from the imaging bed.

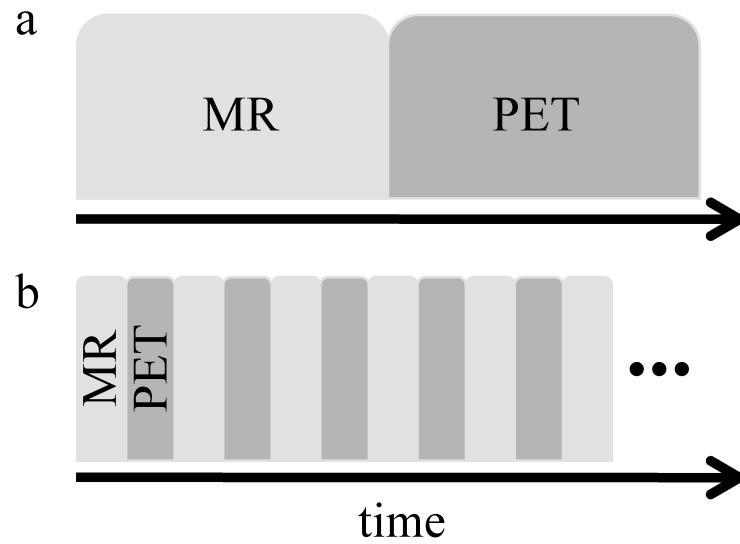


Figure 4.5: Conceptual timing for (a) sequential and (b) interleaved imaging sequences for PET and field-cycled MRI.

While higher polarizing field strengths would result in improved signal-to-noise, power and cooling requirements, which scale as the square of the field, place severe limitations on the field of resistive electromagnets. The system described here used a 200-V/150-A direct current power supply, which limited the polarizing field to 0.3 T at approximately 50% duty cycle. With the use of capacitor banks and reduced duty cycle, it may be possible to achieve polarizing fields in excess of 1 T.

The successful generation of the first dual modality PET and field-cycled MRI image demonstrates the feasibility of this approach to PET/MRI. Further tests are necessary to quantitatively evaluate the performance of this system under a variety of conditions.

4.5 Acknowledgements

This work was supported by the Natural Sciences and Engineering Research Council of Canada (NSERC), the Ontario Innovation Trust, the Canadian Foundation for Innovation, and the Plunkett Foundation. B.A.C holds the Canada Research Chair in Medical Physics at the University of Western Ontario. G.A.B. was supported by an NSERC Alexander Graham Bell Canada Graduate Scholarship.

4.6 References

1. Townsend DW. Positron emission tomography/computed tomography. *Seminars in Nuclear Medicine* 2008;38(3):152-166.
2. Chun SY, Reese T, Guerin B, Zhu X, Cho S, Ouyang J, Catana C, El Fakhri G. 4D tagged MR-based motion correction in simultaneous PET-MR. In *Proceedings of the 51st Annual Meeting of the Society of Nuclear Medicine*. Salt Lake City, Utah, USA; 2010. p 80.
3. Judenhofer MS, Wehrl HF, Newport DF, Catana C, Siegel SB, Becker M, Thielscher A, Kneilling M, Lichy MP, Eichner M *and others*. Simultaneous PET-MRI: a new approach for functional and morphological imaging. *Nature Medicine* 2008;14(4):459-465.
4. Wehrl HF, Judenhofer MS, Wiehr S, Pichler BJ. Pre-clinical PET/MR: technological advances and new perspectives in biomedical research. *European Journal of Nuclear Medicine and Molecular Imaging* 2009;36 Suppl 1:S56-68.
5. von Schulthess GK, Schlemmer HPW. A look ahead: PET/MR versus PET/CT. *European Journal of Nuclear Medicine and Molecular Imaging* 2009;36:3-9.
6. Boone JM, Velazquez O, Cherry SR. Small-animal X-ray dose from micro-CT. *Molecular Imaging* 2004;3(3):149-158.
7. Delso G, Ziegler S. Pet/Mri System Design. *European Journal of Nuclear Medicine and Molecular Imaging* 2009;36:86-92.
8. Cherry SR, Louie AY, Jacobs RE. The integration of positron emission tomography with magnetic resonance imaging. *Proceedings of the Ieee* 2008;96(3):416-438.
9. Yamamoto S, Imaizumi M, Kanai Y, Tatsumi M, Aoki M, Sugiyama E, Kawakami M, Shimosegawa E, Hatazawa J. Design and performance from an integrated PET/MRI system for small animals. *Annals of Nuclear Medicine* 2010;24(2):89-98.
10. Raylman RR, Majewski S, Velan SS, Lemieux S, Kross B, Popov V, Smith MF, Weisenberger AG. Simultaneous acquisition of magnetic resonance spectroscopy (MRS) data and positron emission tomography (PET) images with a prototype MR-compatible, small animal PET imager. *Journal of Magnetic Resonance* 2007;186(2):305-310.
11. Yamamoto S, Hatazawa J, Imaizumi M, Shimosegawa E, Aoki M, Sugiyama E, Kawakami M, Takamatsu S, Minato K, Matsumoto K *and others*. A Multi-Slice Dual Layer MR-Compatible Animal PET System. *IEEE Transactions on Nuclear Science* 2009;56(5):2706-2713.

12. Mackewn J, Strul D, Hallett W, Halsted P, Page R, Keevil S, Williams S, Cherry S, Marsden P. Design and development of an MR-compatible PET scanner for imaging small animals. *IEEE Transactions on Nuclear Science* 2005;52(5 Part 1):1376-1380.
13. Lucas AJ, Hawkes RC, Ansorge RE, Williams GB, Nutt RE, Clark JC, Fryer TD, Carpenter TA. Development of a combined microPET-MR system. *Technology in Cancer Research and Treatment* 2006;5(4):337-341.
14. Catana C, Procissi D, Wu YB, Judenhofer MS, Qi JY, Pichler BJ, Jacobs RE, Cherry SR. Simultaneous in vivo positron emission tomography and magnetic resonance imaging. *Proceedings of the National Academy of Sciences of the United States of America* 2008;105(10):3705-3710.
15. Woody C, Schlyer D, Vaska P, Tomasi D, Solis-Najera S, Rooney W, Pratte JF, Junnarkar S, Stoll S, Master Z *and others*. Preliminary studies of a simultaneous PET/MRI scanner based on the RatCAP small animal tomograph. *Nucl Instrum Methods Phys Res Sect A* 2007;571(1-2):102-105.
16. Schlemmer HP, Pichler BJ, Krieg R, Heiss WD. An integrated MR/PET system: prospective applications. *Abdominal Imaging* 2009;34(6):668-674.
17. Gilbert KM, Scholl TJ, Handler WB, Alford JK, Chronik BA. Evaluation of a Positron Emission Tomography (PET)-Compatible Field-Cycled MRI (FCMRI) Scanner. *Magnetic Resonance in Medicine* 2009;62(4):1017-1025.
18. Kegler C, Seton HC, Hutchison JM. Prepolarized fast spin-echo pulse sequence for low-field MRI. *Magnetic Resonance in Medicine* 2007;57(6):1180-1184.
19. Macovski A, Conolly S. Novel Approaches to Low-Cost MRI. *Magnetic Resonance in Medicine* 1993;30(2):221-230.
20. Matter NI, Scott GC, Venook RD, Ungersma SE, Grafendorfer T, Macovski A, Conolly SM. Three-dimensional prepolarized magnetic resonance imaging using rapid acquisition with relaxation enhancement. *Magnetic Resonance in Medicine* 2006;56(5):1085-1095.
21. Ungersma SE, Matter NI, Hardy JW, Venook RD, Macovski A, Conolly SM, Scott GC. Magnetic resonance imaging with T1 dispersion contrast. *Magnetic Resonance in Medicine* 2006;55(6):1362-1371.
22. Venook RD, Matter NI, Ramachandran M, Ungersma SE, Gold GE, Giori NJ, Macovski A, Scott GC, Conolly SM. Prepolarized magnetic resonance imaging around metal orthopedic implants. *Magnetic Resonance in Medicine* 2006;56(1):177-186.
23. Anger HO. Scintillation Camera. *Review of Scientific Instruments* 1958;29(1):27-33.

24. Peng H, Handler WB, Scholl TJ, Simpson PJ, Chronik BA. Proof-of-principle study of a small animal PET/field-cycled MRI combined system using conventional PMT technology. *Nucl Instrum Methods Phys Res Sect A* 2010;612(2):412-420.
25. Fueger BJ, Czernin J, Hildebrandt I, Tran C, Halpern BS, Stout D, Phelps ME, Weber WA. Impact of animal handling on the results of F-18-FDG PET studies in mice. *Journal of Nuclear Medicine* 2006;47(6):999-1006.

Chapter 5

5 Validation Tests on a Monte Carlo PET Simulation Architecture based on GATE¹

In this chapter, a new implementation of a Monte Carlo PET simulation architecture is described. This approach uses the histogramming and image reconstruction software of the Siemens Inveon PET to reduce possible inconsistencies between experimental and simulation workflows. To validate the architecture, this chapter presents a precise model of the NEMA NU 4-2008 image quality phantom and source distribution implemented in the Monte Carlo package GATE. Using the NEMA image quality measurement protocols, images from simulated data were compared with experimental images from the Siemens Inveon PET, with all corrections and reconstructions done using the software of the scanner. The simulated images showed good agreement with the experimental images, displaying matching activity distributions.

5.1 Introduction

Positron emission tomography (PET) has become an indispensable modality for preclinical studies using small animals. There have been many recent developments in the design and characterization of new high-performance small animal PET systems employing a variety of geometries and scintillator materials.

¹ At the time of this thesis publication, a manuscript based on this chapter was in the final stage of preparation for submission.

As a result, the importance of Monte Carlo simulations for assessing the performance of new PET systems has grown. One of the best-supported and widely used Monte Carlo frameworks for PET simulation is the GEANT4 Application for Tomographic Emission (GATE) package, maintained by the OpenGATE Collaboration [1]. The underlying GEANT4 Monte Carlo code has been validated extensively for fundamental physics interactions. GATE models of several commercial human-scale PET systems have been validated experimentally [2-4] and small animal PET systems have also been studied [5-8]. Model definitions for common PET phantoms for human-scale systems have been included with the GATE distribution; however, phantom models for small animal systems have not been generally available.

The National Electrical Manufacturers Association (NEMA) has published a set of phantom designs (NU 4-2008) for measuring the performance of small animal PET scanners [9]. Bahri, et al. [10] were among the first to make an extensive study with the NEMA NU 4-2008 image quality phantom. These phantoms and their associated scanning procedures are now considered to be the standard for the measurement of small animal PET system performance [11-15]. The geometries of most of the NEMA NU 4-2008 phantoms are simple and can be implemented easily in GATE. These include mouse-, rat- and monkey-sized scatter phantoms as well as a point source phantom. The exception is the NEMA small animal image quality phantom, which consists of an intricate arrangement of both hot (activity—containing) and cold (activity void) regions. This phantom is designed to measure uniformity, recovery coefficient and the accuracy of attenuation and scatter corrections.

To address the need for useful and accurate phantom models the authors have implemented a detailed definition of the NEMA image quality phantom in GATE and validated the simulated phantom with experimental data. The purpose of this paper is to describe the approach of integrating simulated PET data into experimental workflows and also to make the NEMA image quality phantom widely available to GATE users modelling small animal PET systems. The codes for the other NEMA NU 4-2008 phantoms are also provided in the appendices for convenience, but detailed results are not provided for them.

5.2 Materials & Methods

5.2.1 Description of the NEMA NU 4-2008 Image Quality Phantom

The NEMA NU 4-2008 image quality phantom consists of a poly(methyl methacrylate) (PMMA) cylinder with an internal diameter of 30 mm and length 50 mm containing three main structural regions. The first is a group of five fillable rods of diameters incremented from 1 mm to 5 mm containing water with activity. The rods are directly connected to a large cylindrical chamber. Within this chamber at the end opposite the rods are two smaller chambers: one containing water with no activity and the other containing air. Nylon screws and rubber gaskets seal the openings on either end of the phantom. A scale drawing of the NEMA image quality phantom is shown in Figure 5.1.

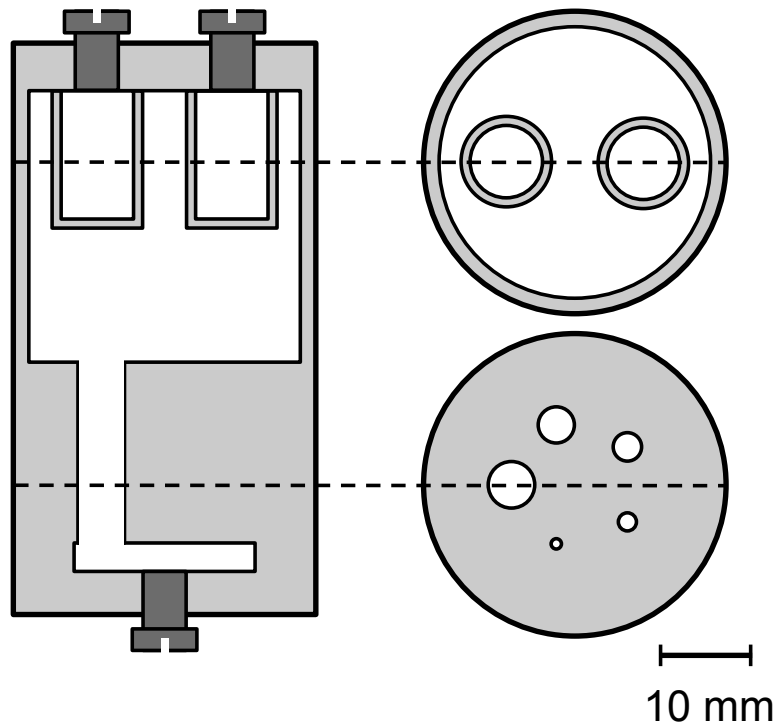


Figure 5.1: Scale drawing of the NEMA NU-2008 image quality phantom. Nylon screws are shown in dark grey and PMMA is shown in light grey. The main body of the phantom is filled with activity-containing water. The two smaller chambers at the top of the phantom contain non-radioactive water (left) and air (right). Six small nylon screws on the lower face of the phantom and several rubber gaskets are included in the model, but not shown in this drawing.

The elemental compositions of materials are defined in GATE using either mass fractions or element ratios in a materials definition file. The definitions used for the phantom construction materials are summarized in Table 5.1.

Table 5.1: Material definitions for NEMA NU 4-2008 image quality phantom.

Material	Density (g/cm ³)	Elemental Composition (mass fraction)
PMMA ^a	1.19	Hydrogen (0.080538) Carbon (0.599858) Oxygen (0.319614)
Nylon	1.14	Hydrogen (0.097976) Carbon (0.636856) Nitrogen (0.123779) Oxygen (0.141389)
Rubber (Buna-N)	0.99	Hydrogen (n = 9) Carbon (n = 7) Nitrogen (n = 1)

^aPMMA is included as ‘plexiglass’ in the default GATE materials definition file.

The NEMA specification calls for a total activity of 3.7 MBq ($\pm 5\%$) ¹⁸F in the water-filled hot regions at the beginning of data acquisition. The GATE macro files containing the geometric definition of this phantom and the source distribution are described in the Appendix.

It should be noted that the physical phantom used for the experiment differed slightly from the NEMA design and had the rods at a slightly different orientation (rotated slightly). In the simulation, the geometry of the phantom was chosen to match the physical phantom. This rotation is not expected to affect the results. The GATE macro files provided are for the phantom as specified in the NEMA standard, matching the orientation shown in Figure 5.1.

5.2.2 Monte Carlo Simulation Architecture

A GATE PET emission simulation was conducted with the image quality phantom using a model of the Siemens Inveon PET system (Siemens Medical Solutions, Knoxville, TN). The author developed software to convert coincidence data from the Monte Carlo simulation to the list mode format of the commercial scanner. Then, all sinogram generation and reconstruction of simulated data were performed on the software used to process list mode data from the real scanner (Inveon Acquisition Workplace 1.5). The benefit of having a common processing path for experimental and simulated data is that it allows images to be compared directly without the concern of having different data correction and reconstruction algorithms.

The PET system model was obtained from Konik, et al. [7] and was modified by rotating the detector ring 11.25 degrees to align the detector blocks with their positions on the physical scanner. The detector comprises four 16-block rings, each detector block containing a 20×20 array of $1.5 \text{ mm} \times 1.5 \text{ mm} \times 10 \text{ mm}$ lutetium orthosilicate (LSO) scintillator crystals attached to a position sensitive photomultiplier tube (see Figure 1.1). Only the scintillator crystal arrays were simulated. Light transport and shielding around the scintillator arrays were not modelled. As a consequence, the simulated system is expected to have greater sensitivity than the real scanner because these sources of loss are not included in the simulation. Furthermore, the lack of shielding at the ends of the detector could have an impact on the scatter fraction in the simulation; however, these effects would be minor because there was no simulated activity outside the axial field of view. The intrinsic radioactivity of LSO from ^{176}Lu was not simulated because the

comparatively high source activity and narrow energy window make any effects negligible [16].

A 3-mm-thick semi-circular pallet matching the dimensions of the carbon-fibre-reinforced polymer pallet included with the actual scanner was included in the model. The actual material composition and density of the physical pallet were unknown, so estimates were obtained from suppliers. In the simulation, a density of 1.58 g/cm^3 was assumed and the mass fractions were as follows: carbon (0.845), hydrogen (0.043) and oxygen (0.112).

The digitizer parameters in the simulation were chosen to match experimental values. The energy and coincidence timing windows were set to 350-650 keV and 3.43 ns, respectively. The coincidence sorter was set to the policy *takeWinnerOfGoods* for cases with three or more detections within the coincidence timing window. This policy records the two highest-energy detections that would form a valid line of response. Energy blurring was set to 14.6%, consistent with values measured experimentally [11].

From the simulation, it was possible to distinguish coincidences arising from different positron decays (random coincidences) from those arising from a single positron decay. These random coincidences were inserted twice into the listmode data stream: once as a normal coincidence event packet, and a second time as a random coincidence event packet. In this way, the simulated random events match the characteristics of the way random coincidences are treated by the PET system during an actual acquisition.

Radioactivity was modelled as ^{18}F in water. Positron decay was simulated using the positron energy spectrum of ^{18}F , which is built into GATE. The total activity was 3.7 MBq distributed uniformly throughout the hot regions.

The following physics models were enabled in the GATE simulation: positron annihilation, photoelectric effect (standard model), Compton scattering (standard model), Rayleigh scattering (Penelope model), electron ionization (standard model), bremsstrahlung radiation (standard model), and multiple scattering for electrons and positrons. The models included interaction cross-sections for each of these effects. The *MersenneTwister* random number engine was selected in the GATE parameters.

The simulation was run on a Mac Pro (Apple, Cupertino, CA) with 2×2.26 GHz Quad-Core Intel Xeon CPUs and 16 GB RAM. GATE version 6.1 [17] and ROOT version 5.3 were used. The total simulated time was 20 minutes and coincidence event output data from the emission simulation were recorded in the ROOT file format. To reduce computation time, the time course of the simulation was split into 80 parts evenly distributed in time with 8 simultaneous processes running at a given time. Each simulation had a different random number engine seed. The total computation time was 49 hours.

5.2.3 Simulated Data Processing Chain

Coincidence data from the ROOT files were processed with in-house software to form a single list mode file in the format used by the Siemens Inveon PET, including prompt and delayed coincidences as well as time marks.

Normalization calibration data were generated with a GATE emission simulation of a homogenous cylinder source (diameter: 6 cm, length: 12.7 cm, activity: 1 MBq) and stored in the ROOT file format. The physical properties and material composition of the cylinder were obtained from the manufacturer of the normalization phantom used in the experiment. These properties are described further in Chapter 6. Ge-68 is used in the physical calibration cylinder source; however, to reduce simulation time, the simulated source was modelled as a generator of back-to-back gamma rays in the region of activity. The activity was chosen to be lower than the typical value ($\sim 10^7$ decays per second) to shorten simulation time by reducing random events. This is not expected to have a significant impact on the normalization. Approximately 3.0×10^9 prompts were simulated for the normalization data. A list mode format file was generated from the ROOT files and the normalization correction sinogram was produced with the commercial software using the component-based algorithm. Scattered events were included in the normalization data.

The authors extended the GATE package by adding a custom actor class to produce an attenuation correction sinogram in the format used by the Siemens PET reconstruction software. Chapter 6 contains a detailed explanation of this new approach. This method produces an ideal noiseless attenuation correction sinogram. On the scanner, attenuation correction sinograms are generated using a ^{57}Co transmission source and this introduces an additional source of noise in the experimental images, which is not present in simulated images.

The simulated and experimental data reconstruction pipeline is shown schematically in Figure 5.2. The benefit of this approach is that the data

processing chain for experimental and simulated data is identical for many steps of the workflow.

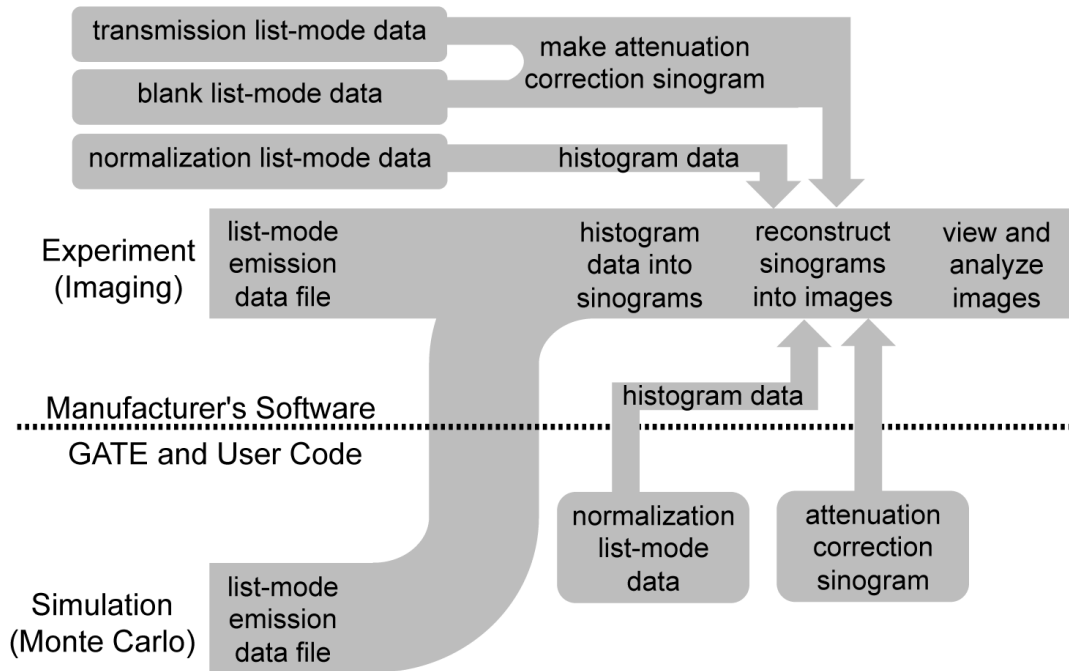


Figure 5.2: Schematic showing the workflow of experimental and simulated data reconstruction and corrections. In the simulation, the attenuation correction sinogram is computed directly from the lines of response through the phantom materials. In contrast, on the physical scanner, to compute the attenuation correction sinogram requires a blank transmission scan in addition to the transmission data with the phantom present.

5.2.4 Experimental PET Acquisition

A NEMA image quality phantom was filled with water containing ^{18}F -fluorodeoxyglucose (^{18}F -FDG) with activity 3.7 ± 0.1 MBq at the start of scanning, measured with a gamma counter. The phantom was positioned in the centre of the field of view on a carbon fibre pallet. A 20-minute emission

acquisition was performed on a Siemens Inveon Dedicated PET installed in our lab with the same parameters as the simulation. The phantom was then kept in the same position while the activity was allowed to decay to less than 1% of the original value (10 half-lives). Then, a 30-minute transmission scan was performed using the two built in ^{57}Co rotating sources to generate an attenuation correction sinogram.

5.2.5 Image Reconstruction and Analysis

Images for both simulated and experimental data were reconstructed using Inveon Acquisition Workplace 1.5 using the OSEM2D algorithm with 16 subsets and 4 iterations. For both images, the following corrections were applied: decay, scatter, arc, deadtime, component-based normalization, and attenuation correction.

The images were analysed to assess uniformity, recovery coefficients and the accuracy of corrections according to the protocols in the NEMA standard. All analysis was performed with MATLAB (The MathWorks Inc.). Due to the higher expected count rate for the simulation, the reconstructed activity of the simulation was scaled down by a factor of 0.841 such that the mean activity of the large uniform region matched that of the experimental image. The NEMA analysis protocols are described below.

Uniformity

A cylindrical volume of interest (VOI) with diameter 22.5 mm and length 10 mm was drawn in the centre of the large uniform region. The mean activity concentration, the percentage standard deviation (%STD) and the minimum and maximum values in the VOI were computed.

Recovery Coefficients

The image slices containing the central 10 mm length of the five rods were averaged to form one slice of lower noise. Then, the transverse coordinates of the maximum value pixel in each rod were recorded. These transverse coordinates were used to create line profiles in the axial direction along each rod. The mean activity concentration along each of the five line profiles was computed and divided by the mean activity concentration found in the uniform section to obtain the recovery coefficient for each rod. The percentage standard deviation of the recovery coefficient (%STD_{RC}) was computed as follows:

$$\%STD_{RC} = 100 \times \sqrt{\left(\frac{STD_{\text{lineprofile}}}{Mean_{\text{lineprofile}}} \right)^2 + \left(\frac{STD_{\text{uniform}}}{Mean_{\text{uniform}}} \right)^2} \quad (5.1)$$

Accuracy of Corrections

Cylindrical VOIs with diameter 4 mm and length 7.5 mm were drawn over the centres of the air- and water-filled cold regions. The spill over ratio (SOR) was computed as the ratio of the mean activity in the cold regions to the mean of the uniform hot region, expressed as a percentage. The uncertainties of the SOR values were also computed.

5.3 Results

Images reconstructed from experimental and simulated data are shown in Figure 5.3. The geometric distribution of reconstructed activity in the simulated image can be seen to match well with the experimental image.

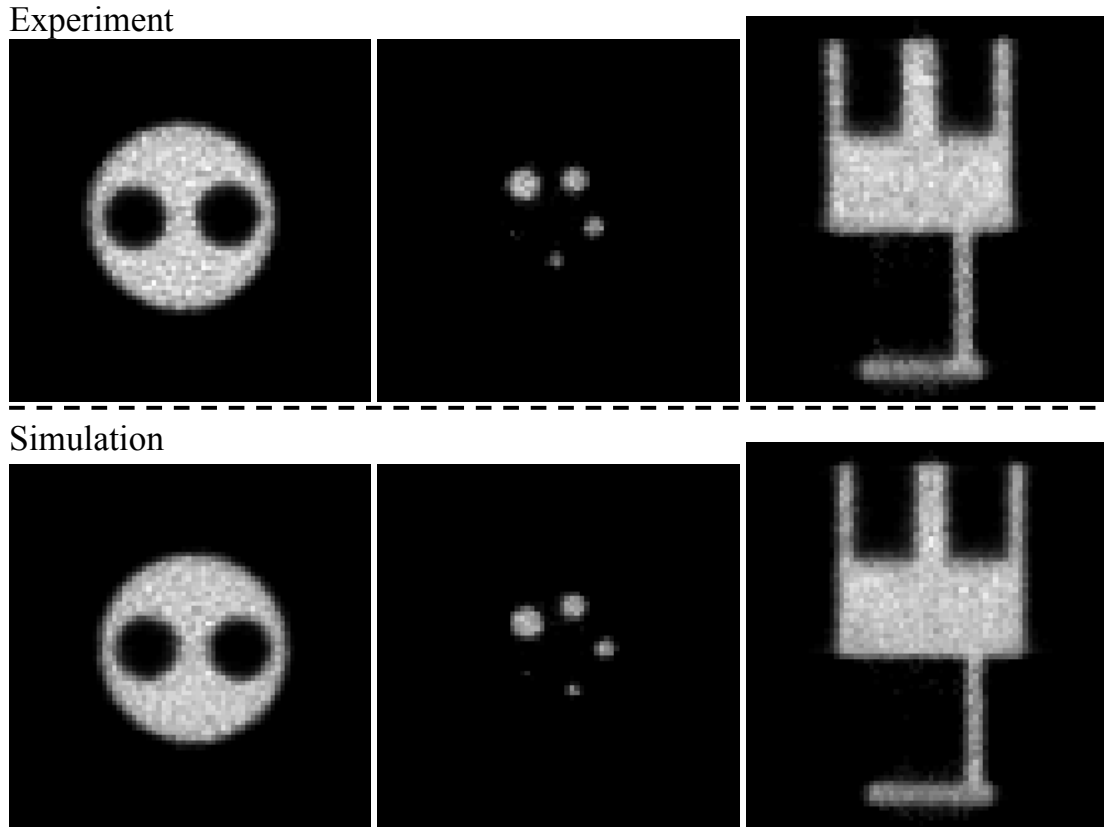


Figure 5.3: Reconstructed PET images of the NEMA NU 4-2008 image quality phantom for experimental data (top) and simulated data (bottom). Two transverse slices and one coronal slice are shown with no interpolation applied. The reconstructed activity distribution in the simulated image shows agreement with the experimental image. Higher noise is visible in the experimental image due to the fewer prompts recorded in the experimental acquisition.

The number of coincidence events recorded in the experimental acquisition was 1.8×10^8 prompts, whereas in the simulation there were 2.2×10^8 prompts of which there were 1.8×10^8 true coincidences, 3.6×10^7 object-scattered coincidences (16.4% scatter fraction), and 2.2×10^6 random coincidences (1.0% random rate). While it is impossible to distinguish true and scattered coincidences in the experimental data stream, the number of random coincidences detected in

the experiment by the delayed timing window approach was 1.5×10^6 (0.85% random rate).

The percentage standard deviations of the uniform region of the images were 7.0% (experiment) and 6.2% (simulation). The simulation contained more prompts than the experiment, which is a reason for the lower %STD of the simulated image. After truncating the simulated listmode data file so that the number of prompts matched that of the experiment, the %STD value for the simulation was found to be 6.8%, consistent with what would be expected from Poisson statistics.

The mean recovery coefficients for the five rods are shown in Figure 5.4 for experimental and simulated images. The error bars of the experimental and simulated recovery coefficients overlapped for each rod size.

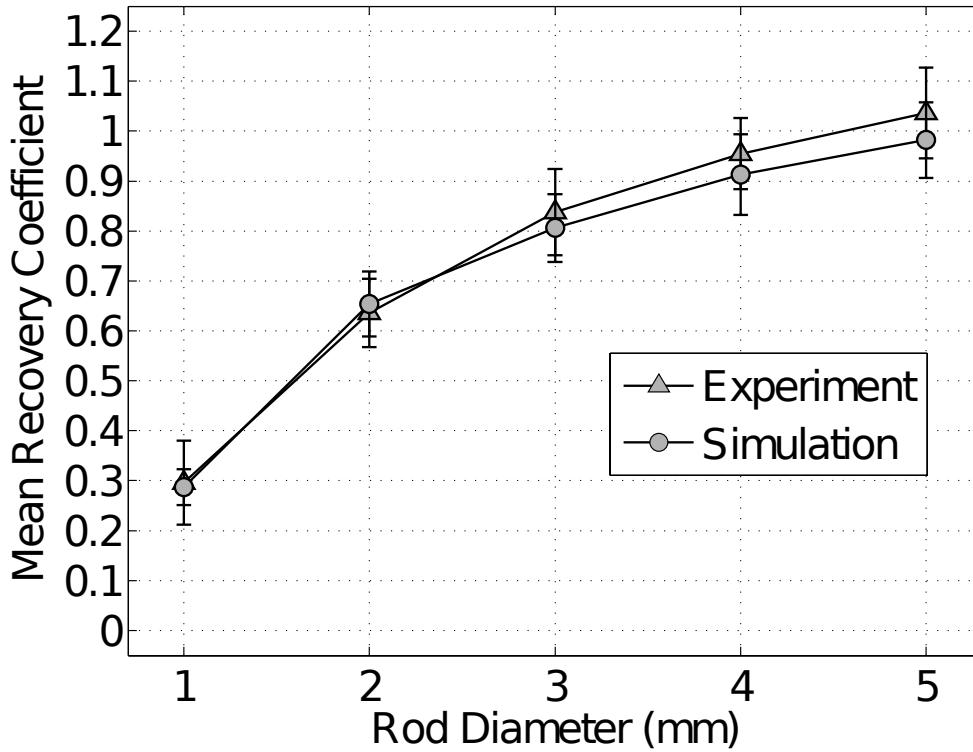


Figure 5.4: Mean recovery coefficient as a function of rod diameter for experimental and simulated images. The error bars represent the standard deviation calculated with Equation (5.1). Lines connecting the data points are meant as guides to the eye. The recovery coefficient is lower for the smaller rods because of the partial volume effect.

The SORs for the experimental image were (4.51 ± 0.08) % for the air-filled cold region and (5.29 ± 0.09) % for the water-filled region. For the simulated image, the SORs were (6.37 ± 0.09) % for the air-filled region and (6.77 ± 0.08) % for the water-filled region. SORs were highly dependent on the choice of reconstruction algorithm and whether scatter and attenuation corrections were applied, as was found by Bahri, et al. [10] using the previous-generation Siemens FOCUS 120 PET system and by Anizan, et al. [18] using the Siemens Inveon. In all cases, the

simulated image had significantly higher SOR values than the experimental image ($p < 0.01$, using Student's t-test) for a range of reconstruction algorithms.

5.4 Discussion

A visual comparison of the experimental and simulated images shows that the GATE phantom model is an accurate representation of the NEMA specification. The phantom model implemented is a good model for the GATE community to use to assess the quality of scanner simulations.

The image quality measurements do not match exactly for all indicators in both images. This is likely due to the experimental conditions not matching the ideal simulated conditions. The higher absolute counts recorded in the simulation was the likely cause of the percentage standard deviation of the uniform region (%STD) being lower for the simulated image. If the number of prompts in the simulation were the same as the experiment, the %STD of the simulated image is 6.8%, which is very close to the 7.0% recorded for the experimental image. The fact that the attenuation correction method did not add noise into the simulation may also have contributed to the lower noise in the simulated image. In light of this, the %STDs and the RCs of the both images were in agreement with experimental results published by Disselhorst, et al. [13]. The SORs for the experimental image were also consistent with those published by Disselhorst, et al. [13] and Anizan, et al. [18]; however, the SORs were higher for the simulated image indicating the possibility of more photon scattering in the simulated phantom or bed than was the case experimentally. It is not possible to measure scatter fraction experimentally; however, since the reconstruction pathway was the

same for both experimental and simulated images, we suspect that the cause of these differences was in the emission simulation. One possibility is that the choice of models for physics processes may have had an impact on the rate of scattering. In this simulation, standard model Compton scattering processes were used for all materials; however, non-parameterized models designed for use at lower energies, such as those based on the Livermore or Penelope data libraries, may be more accurate and should be investigated. Another possible source of differences in scattering behaviour between measured and simulated data is that the thin shielding material in the gantry of the scanner was not included in the simulation. The shielding geometry and material were unknown to the authors, but this could be included in future simulations with data from the manufacturer. While differences between simulation and experiment were observed by McIntosh, et al. [16] due to the non-linear energy response of the LSO-based detectors of the Inveon scanner, this effect is not expected to be important in this study because of the higher energy window used here (350-650 keV).

5.5 Conclusion

A precise definition of the NEMA NU 4-2008 image quality phantom for small animal PET scanners has been implemented in the GATE Monte Carlo framework. Images of the phantom generated from simulated and experimental data sets were analysed according to the NEMA protocol. The simulated image showed good agreement with the experimental image; however, spill over ratios were higher in the simulated images. The NEMA NU 4-2008 image quality phantom is now available for Monte Carlo GATE simulations of small animal PET and SPECT systems.

5.6 Acknowledgement

We thank Ziad Burbar (Siemens) for a helpful technical discussion on the raw data format of the PET system.

5.7 References

1. Jan S, Santin G, Strul D, Staelens S, Assie K, Autret D, Avner S, Barbier R, Bardies M, Bloomfield PM *and others*. GATE: a simulation toolkit for PET and SPECT. *Physics in Medicine and Biology* 2004;49(19):4543-4561.
2. Jan S, Comtat C, Strul D, Santin G, Trebossen R. Monte Carlo simulation for the ECAT EXACT HR plus system using GATE. *IEEE Transactions on Nuclear Science* 2005;52(3):627-633.
3. Lamare F, Turzo A, Bizais Y, Le Rest CC, Visvikis D. Validation of a Monte Carlo simulation of the Philips Allegro/GEMINI PET systems using GATE. *Physics in Medicine and Biology* 2006;51(4):943-962.
4. Poon JK, Dahlbom ML, Moses WW, Balakrishnan K, Wang W, Cherry SR, Badawi RD. Optimal whole-body PET scanner configurations for different volumes of LSO scintillator: a simulation study. *Physics in Medicine and Biology* 2012;57(13):4077-4094.
5. van der Laan DJ, Maas MC, de Jong HWAM, Schaart DR, Bruyndonckx P, Lemaitre C, van Eijk CWE. Simulated performance of a small-animal PET scanner based on monolithic scintillation detectors. *Nuclear Instruments & Methods in Physics Research Section a-Accelerators Spectrometers Detectors and Associated Equipment* 2007;571(1-2):227-230.
6. Goertzen AL, Stout DB, Thompson CJ. A method for measuring the energy spectrum of coincidence events in positron emission tomography. *Physics in Medicine and Biology* 2010;55(2):535-549.
7. Konik A, Madsen MT, Sunderland JJ. GATE Simulations of Human and Small Animal PET for Determination of Scatter Fraction as a Function of Object Size. *IEEE Transactions on Nuclear Science* 2010;57(5):2558-2563.
8. Zeraatkar N, Ay MR, Kamali-Asl AR, Zaidi H. Accurate Monte Carlo modeling and performance assessment of the X-PET (TM) subsystem of the FLEX Triumph (TM) preclinical PET/CT scanner. *Medical Physics* 2011;38(3):1217-1225.
9. National Electrical Manufacturers Association. NEMA Standard Publication NU 4-2008: Performance Measurements of Small Animal Positron Emission Tomographs. Rosslyn, VA: National Electrical Manufacturers Association; 2008.

10. Bahri MA, Plenevaux A, Warnock G, Luxen A, Seret A. NEMA NU4-2008 Image Quality Performance Report for the microPET Focus 120 and for Various Transmission and Reconstruction Methods. *Journal of Nuclear Medicine* 2009;50(10):1730-1738.
11. Bao Q, Newport D, Chen M, Stout DB, Chatziioannou AF. Performance Evaluation of the Inveon Dedicated PET Preclinical Tomograph Based on the NEMA NU-4 Standards. *Journal of Nuclear Medicine* 2009;50(3):401-408.
12. Constantinescu CC, Mukherjee J. Performance evaluation of an Inveon PET preclinical scanner. *Physics in Medicine and Biology* 2009;54(9):2885-2899.
13. Disselhorst JA, Brom M, Laverman P, Slump CH, Boerman OC, Oyen WJG, Gotthardt M, Visser EP. Image-Quality Assessment for Several Positron Emitters Using the NEMA NU 4-2008 Standards in the Siemens Inveon Small-Animal PET Scanner. *Journal of Nuclear Medicine* 2010;51(4):610-617.
14. Visser EP, Disselhorst JA, van Lier MGJTB, Laverman P, de Jong GM, Oyen WJG, Boerman OC. Characterization and optimization of image quality as a function of reconstruction algorithms and parameter settings in a Siemens Inveon small-animal PET scanner using the NEMA NU 4-2008 standards. *Nuclear Instruments & Methods in Physics Research Section a-Accelerators Spectrometers Detectors and Associated Equipment* 2011;629(1):357-367.
15. Goertzen AL, Bao QN, Bergeron M, Blankemeyer E, Blinder S, Canadas M, Chatziioannou AF, Dinelle K, Elhami E, Jans HS *and others*. Nema Nu 4-2008 Comparison of Preclinical Pet Imaging Systems. *Journal of Nuclear Medicine* 2012;53(8):1300-1309.
16. McIntosh B, Stout DB, Goertzen AL. Validation of a GATE Model of Lu-176 Intrinsic Radioactivity in LSO PET Systems. *IEEE Transactions on Nuclear Science* 2011;58(3):682-686.
17. Jan S, Benoit D, Becheva E, Carlier T, Cassol F, Descourt P, Frisson T, Grevillot L, Guigues L, Maigne L *and others*. GATE V6: a major enhancement of the GATE simulation platform enabling modelling of CT and radiotherapy. *Physics in Medicine and Biology* 2011;56(4):881-901.
18. Anizan N, Carlier T, Hindorf C, Barbet J, Bardies M. dAcquisition setting optimization and quantitative imaging for 124I studies with the Inveon microPET-CT system. *EJNMMI Res* 2012;2:7.

Chapter 6

6 Attenuation Correction Sinogram Add-On to GATE¹

This chapter describes a custom add-on that extends the GATE Monte Carlo PET simulation package to produce attenuation correction sinograms. The method implemented here is computationally fast and uses the photon interaction cross-sections and precise phantom and detector geometries of the emission simulation.

6.1 Introduction

PET images are reconstructed from sets of sinograms. A sinogram is a matrix representation of the coincidence emission data acquired by the PET detector. Each element of a sinogram corresponds to a particular pair of crystal elements and the line that connects two crystals is called a line of response (LOR). When a positron annihilation event occurs in the PET field of view, the two annihilation photons will arrive at opposing detector crystals within a very short time of each other if they do not interact and their direction lies along one of the possible LORs. The central principle of PET imaging is that the number of coincidences detected along any LOR in a given period of time is proportional to the total activity contained in that LOR.

¹ A manuscript based on the contents of this chapter was in preparation at the time of thesis publication.

In real PET systems, several corrections are necessary to increase the accuracy of the activity map generated by the PET reconstruction algorithm. The most important of these corrections include normalization, attenuation correction, scatter correction, random correction, dead-time correction, decay correction and arc correction. Normalization corrects both geometric and intrinsic variation in crystal detection efficiency. Attenuation correction improves the quantitative accuracy of PET images by incorporating information about the distribution of attenuating material in the PET field of view. Scatter correction methods model the effect of Compton scattering within the object being imaged and attempt to reduce the added blurring and noise that results from scattering in PET images. Random correction adjusts the measured activity downward by estimating the rate of simultaneous random detections arising from two different positron emissions. Dead-time correction adjusts the measured activity upward to account for the rate of missed coincidence detections due to detector dead-time. Arc correction compensates for the variation in the spacing between lines of response due to the circular nature of the detector ring. This chapter focuses on attenuation correction.

6.1.1 Principles of Attenuation Correction

As an annihilation photon travels from the point of generation through tissues and other materials, there is a chance that it could undergo one or more interactions. For the energies relevant to PET, the most important interactions are the photoelectric effect and Compton scattering. The probabilities of these interactions depend on photon energy, material composition, and density. If these are known, the attenuation behaviour can be described by the linear attenuation

coefficient, μ . For photons travelling through attenuating material, the photon intensity, I , after the photons have travelled a length x will be

$$I(x) = I_0 e^{-\mu x}, \quad (6.1)$$

where I_0 is the incident intensity such that the transmittance will be I/I_0 , and the fraction attenuation will be $(1 - I/I_0)$. For the same path length, a material having a larger attenuation coefficient, μ , will reduce the photon intensity to a greater extent. The total attenuation coefficient is the sum of the attenuation coefficients for each interaction process:

$$\mu_{\text{total}} = \mu_{\text{Compton}} + \mu_{\text{photoelectric}} + \dots. \quad (6.2)$$

For 511 keV photons passing through water, biological tissue and typical plastics, the photoelectric effect is several orders of magnitude less likely to occur than Compton scattering. Conversely, scintillation crystal materials are designed to have a high probability of photoelectric effect interactions.

If the photons travel through different materials with attenuation coefficients $\mu_1, \mu_2, \mu_1, \dots, \mu_n$ having path lengths $x_1, x_2, x_1, \dots, x_n$, the total transmittance will be

$$\frac{I}{I_0} = e^{-(\mu_1 x_1 + \mu_2 x_2 + \mu_3 x_3 + \dots + \mu_n x_n)}. \quad (6.3)$$

For PET imaging, photon attenuation will reduce the number of annihilation gamma ray pairs measured in each LOR. This can be corrected by multiplying the

measured number of counts in an LOR by the attenuation correction factor, ACF, which is equal to the inverse of the expected transmission:

$$\text{ACF} = \frac{I_0}{I} = e^{+(\mu_1 x_1 + \mu_2 x_2 + \mu_3 x_3 + \dots + \mu_n x_n)} \quad (6.4)$$

An attenuation correction sinogram is a matrix of ACF values for each line of response. If the sinogram ordering of the attenuation and emission sinograms are the same, the two sinograms can be multiplied together on an element-by-element basis prior to reconstruction to produce an attenuation corrected PET image [1]. Attenuation correction sinograms typically represent 2D axial slices and to correct 3D emission data, reconstruction algorithms must interpolate the attenuation sinograms or rebin the emission sinograms.

Attenuation coefficients represent the likelihood that a photon will undergo an interaction within a given length of material. For photoelectric effect interactions, the photon is completely absorbed; however, for Compton scattering interactions, the photon changes direction and loses some of its energy but is not completely attenuated. Both analytical and Monte Carlo techniques have been implemented in reconstruction algorithms to estimate and correct for the presence of scattered photons in PET data [2-5].

In a photoelectric effect interaction, a photon transfers all of its energy to an electron. The original photon is completely absorbed, and in a scintillator, as the electron moves through the crystal, its scattering will result in the production of secondary photons, through crystal excitation and fluorescence. Compton scattering is the dominant interaction for 511 keV photons in biological materials.

In Compton scattering, a photon collides inelastically with an electron, transferring a fraction of its energy to the electron and changing its direction. For 511 keV photons, small photon scattering angles are significantly more likely than large angles. Figure 6.1 shows how Compton scattering probability for 511 keV photons varies as a function of photon scattering angle, calculated using the Klein-Nishina formula [6,7].

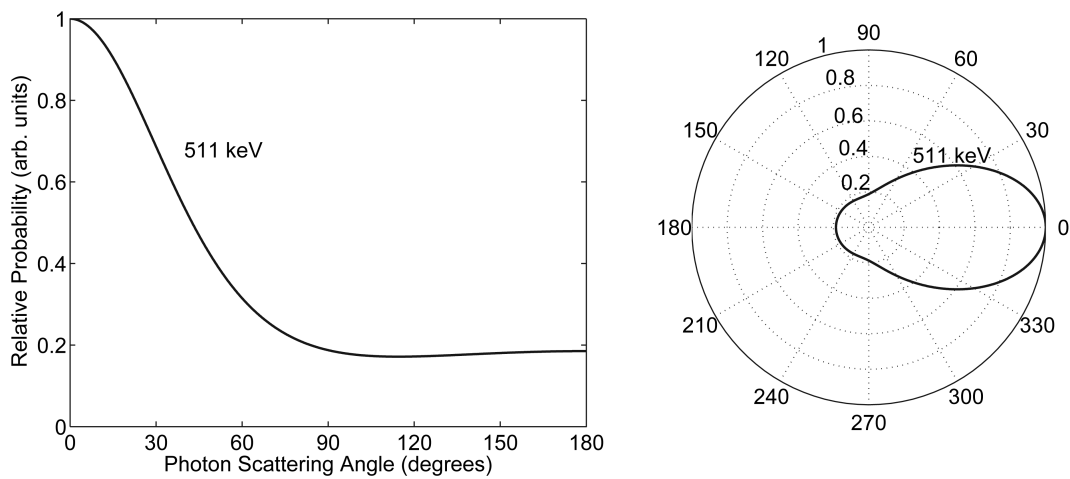


Figure 6.1: Relative probability of Compton scattering as a function of 511 keV photon scattering angle shown in Cartesian form (left) and in polar form (right). The likelihood of small-angle scattering is significantly greater than large-angle scattering.

Photons that undergo large-angle Compton scattering are not detected because the coincidence may occur in an invalid LOR or the remaining photon energy may be too low. Compton scattering at smaller angles introduces noise and blurring into PET images because the incorrect LORs are incremented. However, photons that are scattered through very small angles may still be assigned to the correct LOR or a nearest neighbour LOR with little or no effect on the image. Small-angle scattered photons are indistinguishable from unscattered photons in transmission

scan or CT-based measurements of photon attenuation. Attenuation coefficients generated from models should be adjusted downward to remove the contribution due to small-angle Compton scattering. The magnitude of this adjustment is dependent on the detector geometry and can be estimated by computing the maximum scattering angle that would put the resulting annihilation photons in an adjacent (nearest neighbour) LOR, as shown in Figure 6.2. The interaction probability of Figure 6.1 can be integrated over this small angle range to estimate a global adjustment factor. For the Siemens Inveon detector geometry, the scattering angle should be below 1.77° to be considered small-angle scattering as defined above. Integrating Figure 6.1 for this angle range suggests that 2.8% of scattered photons fall within this limit, yielding an adjustment factor of 0.973. The adjustment factor depends on the assumptions used to determine which scattering angles should be included or excluded from the ACF calculation. The requirement to adjust attenuation coefficients may be considered a drawback of model-based attenuation correction schemes when compared with those based on measured or simulated transmission data.

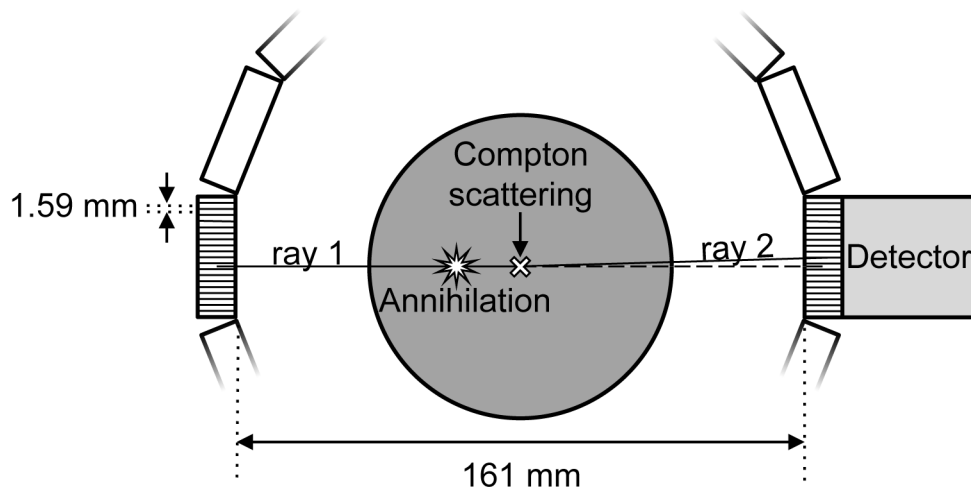


Figure 6.2: Detector geometry of the Siemens Inveon PET showing the approximate angular range for small-angle Compton scattering. The annihilation photon labeled ray 2 has undergone Compton scattering, but should not be considered as having been attenuated. Attenuation correction factors should be adjusted to exclude the contribution from small-angle scattering. For the Siemens Inveon PET detector configuration shown, it is estimated that 2.8% of singly scattered annihilation photons would result in no change in the LOR or be placed in a nearest neighbour LOR with negligible impact on the final image.

6.1.2 Attenuation Correction in Monte Carlo PET Studies

The Geant4 Application for Tomographic Emission (GATE) Monte Carlo simulation package is among the most widespread codes in use for modelling PET and SPECT systems [8] and has recently been extended to enable modelling of CT and radiotherapy systems [9]. GATE lacks a built-in method for rapidly generating attenuation correction sinograms. Some GATE simulation studies of small-animal PET systems have not included attenuation correction [10,11]; however, a variety of approaches have been used for human-scale PET models and for some small-animal PET models. In some studies, a measured CT or transmission image is used to generate a voxelized geometry for the emission

simulation and the measured CT or transmission data can be used to produce attenuation correction sinograms for the simulation [12,13]. In other studies, analytic or voxelized phantoms are imported into a third-party forward-projection tool to produce attenuation correction sinograms [14,15]. GATE CT simulations could be used to model phantom attenuation, and while CT simulations are computationally intensive, various acceleration techniques have been proposed [9]. A similar approach is to simulate singles-mode transmission data, such as using rotating Co-57 or Ge-68 sources [16].

This chapter introduces a novel approach that extends the GATE package to enable the rapid generation of attenuation correction sinograms. The algorithm presented here is highly integrated with GATE and uses the exact material definitions and geometries modelled in the emission simulation.

6.2 Methods

6.2.1 Concept

The GATE attenuation correction add-on described in this chapter loops over each line of response and computes its associated attenuation correction factor. The algorithm tracks the path of a *geantino* (an imaginary particle in Geant4 that does not interact) fired from the centre of one detector crystal toward the other corresponding crystal, passing through the field of view. The attenuation correction factor is built up by obtaining both the path lengths through various materials, including the bed, and the associated 511 keV cross-sections used by the emission simulation.

For the detector geometry and crystal pitch of the Siemens Inveon PET, shown in Figure 6.2, attenuation coefficients generated using this model-based approach were reduced by approximately 2.8% to account for small-angle Compton scattering assuming the average scattering location is at the centre. This factor was computed with the following assumption: photons that scatter once at the centre do not contribute to the ACF if the scattering angle is small enough that the new path would intersect with the detector no farther than one crystal element away from the original path (less than 1.77° on the Siemens Inveon scanner). This simple estimate gives the approximate magnitude of the effect; however, each LOR will have a slightly different response that is dependent on the path of the LOR and the distribution of attenuating material. In the results described in this Chapter, a single global correction factor was used.

6.2.2 Implementation

The attenuation correction add-on is implemented as a GATE *actor* class and can be called from a macro script. The add-on consists of two C++ classes with associated header files and must be compiled along with the GATE package prior to use. The *GateAttenuationCorrectionActorMessenger* class allows the user to set variables such as the sinogram dimensions and output file name. The *GateAttenuationCorrectionActor* class contains the main code. Appendix A.4 contains instructions for obtaining and implementing the code.

The algorithm is designed to loop over all lines of response to match the precise ordering of the Siemens PET sinogram format. The crystal identification scheme was obtained from Siemens for converting GATE emission data to the proprietary list-mode format, as described in Chapter 5; however, the sinogram ordering was

not known. To determine the sinogram ordering, artificial list-mode data files were generated, each containing only coincidences between a different specific crystal pair. Then, the list-mode files were processed using the histogramming software in Inveon Acquisition Workplace and the location of the corresponding LORs were identified in the resulting sinograms.

The Geant4 tracking classes give access to the parameters of the simulation at the various stages of initialization (“run”), particle generation (“event”), and particle tracking (“step”). When the run is first initialized, the attenuation correction actor computes the linear attenuation coefficients of all materials included in both phantom and detector geometries and stores these values in an array. Additional arrays are allocated in memory to store crystal coordinates and ACF values. The algorithm then computes the coordinates of the centres of all the crystal elements in the detector from the internal specification of the detector geometry. The crystal coordinates array is ordered in terms of the azimuthal crystal ID (range 0 – 319 for the Inveon) and the axial ring number (range 0 – 79)².

At the beginning of each primary particle generation event, the appropriate crystal pair is selected and the starting position and direction of the *geantino* particle is set. The *geantino* is then tracked as it steps through phantom materials on its way to the opposing crystal element. For each step through a single phantom material,

² The algorithm was designed to compute the proper ordering for any general block-crystal PET detector geometry and values relevant to the Siemens Inveon PET are shown in parenthesis.

the exact path length and attenuation coefficient³ are multiplied and added to a cumulative sum $(\mu x)_{\text{cumulative}} = \mu_1 x_1 + \mu_2 x_2 + \mu_3 x_3 + \dots$. When the *geantino* reaches the opposing crystal, tracking is stopped and the ACF is computed according to equation (6.4). When the ACFs of all possible LORs have been computed, the ACF values are written to the output sinogram in 32-bit floating-point binary representation.

6.2.3 Validation Testing

Two studies were performed to validate the GATE attenuation correction processing chain. The aim was to verify that the Siemens Inveon Acquisition Workplace software correctly interpreted the simulated AC map. In the first investigation, attenuation correction sinograms of different distributions of attenuating material were produced and the reconstructed attenuation maps were analysed. The second experiment was to compare emission images acquired on the actual scanner with and without attenuation correction to simulated PET images using a model of the same simple phantom.

In each experiment, an attenuation correction sinogram was produced using the GATE add-on. The attenuation sinograms were reconstructed to produce attenuation maps using the filtered back-projection (FBP) algorithm implemented

³ The attenuation coefficient of air is subtracted from the phantom material attenuation coefficient for each step to account for the different LOR lengths. Also, an attenuation correction scale factor is applied to account for small-angle Compton scattering (2.8% reduction for the Inveon PET). On the actual scanner, the transmission scan procedure compensates for both effects inherently.

in the Inveon Acquisition Workplace 1.5 software (ramp filter). The voxel values of the attenuation maps were linear attenuation coefficient (LAC) values. PET emission images were also reconstructed using this algorithm. Attenuation maps and emission images were analysed using AsiPro, an image analysis tool designed specifically for Siemens PET image data.

6.2.3.1 Accuracy of Attenuation Maps

A cylindrical solid phantom containing three thick parallel rods was implemented in GATE. The bulk material of the large cylinder was poly(methyl methacrylate) (PMMA) and different rod material compositions were chosen to have different LAC values. One arrangement (test A) had materials with large differences in LAC (lithium, air, and aluminum), and the other arrangement (test B) used typical biological materials (lung, bone, and water). Figure 6.3 shows the geometry of the phantom and the LAC values of the various materials used in tests A & B, which were computed internally by the GATE physics models.

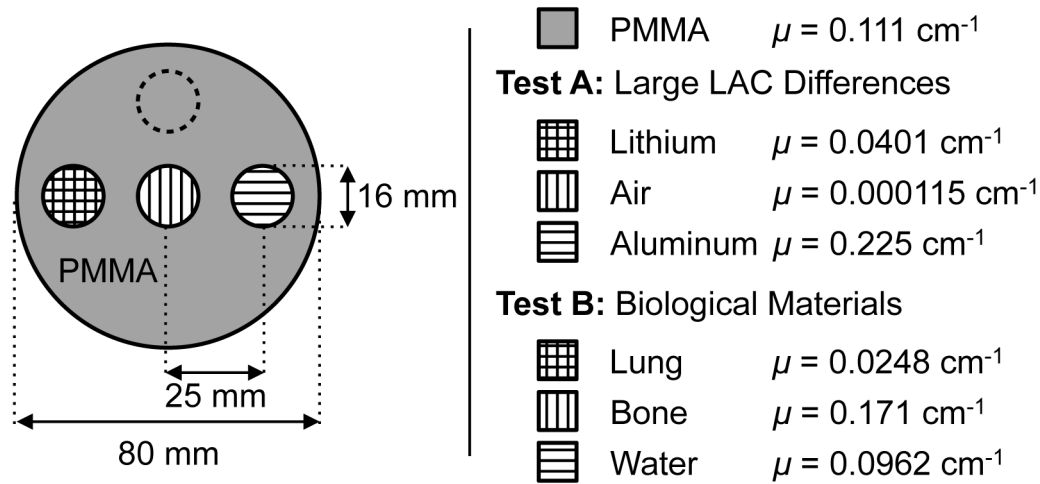


Figure 6.3: Phantom model for testing the accuracy of attenuation maps generated by the simulation. Three rods of different material are shown embedded in a large cylinder of PMMA. The material definitions (density and composition) were the same as those contained in the default materials database distributed with the GATE package. The ‘RibBone’ material definition was used for bone. The linear attenuation coefficient (LAC) values computed by the GATE physics models at 511 keV are shown for PMMA and the three materials used in each test configuration. The dashed circle indicates the location where the LAC value of PMMA was measured in the reconstructed attenuation map.

For each configuration of the phantom model shown in Figure 6.3, an attenuation correction sinogram was produced by the GATE add-on and an attenuation map was reconstructed with filtered back-projection using the Siemens software. The pixel values of the attenuation maps contained the attenuation coefficient for 511 keV photons. The attenuation maps were analysed in two ways: First, the reconstructed LAC values were measured using four circular regions of interest (diameter 10 mm) drawn in the centres of each of three rods and in the bulk PMMA material shown by the dashed circle in Figure 6.3. The results were compared with the internal LAC values computed by the GATE physics models.

Second, a horizontal line profile was computed through the centre of the attenuation map and the results were plotted to show the extent of spatial variations. The thickness of the line profile spanned 5 pixels (approximately 4.2 mm).

6.2.3.2 Comparison of Simulated and Measured PET Images

In the second test, images from an emission simulation were compared with PET images acquired on the actual scanner and the effects of attenuation and scatter corrections were investigated. The Siemens reconstruction software uses a proprietary direct analytical calculation for scatter correction. PET data were acquired on the physical scanner using the homogenous cylindrical Ge-68 source, pictured in Figure 6.4, placed at the centre of the field of view. The active volume of the source had diameter 55.8 mm, length 130 mm, and total activity 1.66 MBq at the time of acquisition.

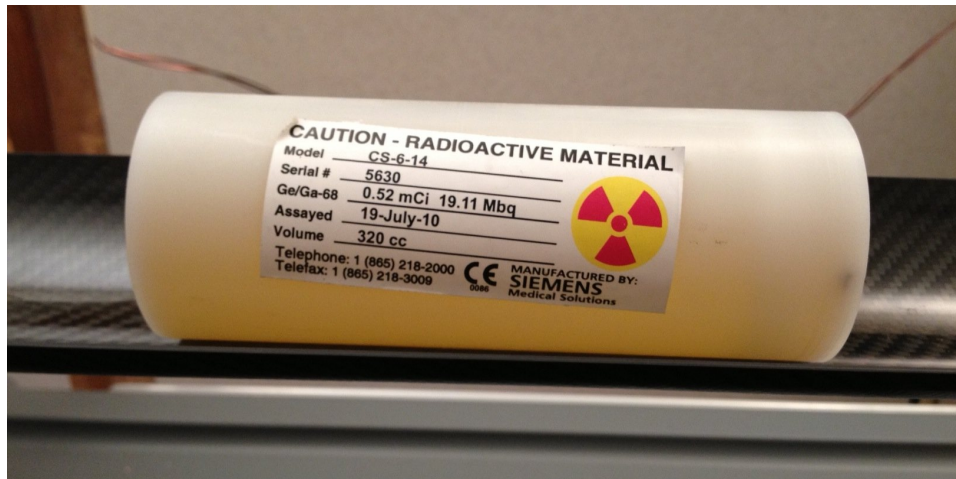


Figure 6.4: Photograph of the Ge-68 phantom used on the physical scanner. A model based on this phantom was used in the simulation.

A model of the physical phantom was implemented in GATE. The precise geometry and estimates for material compositions were obtained from the manufacturer. The inner active region was Ge-68 suspended in epoxy with diameter 55.8 mm and length 130 mm. The outer casing was polyethylene with an inner diameter of 55.8 mm, an outer diameter of 60 mm, and 7.4-mm-thick caps on either end of the inner epoxy. The manufacturer designed the epoxy to have an expected LAC of 0.104 cm^{-1} . The positron emitting source was modelled as a uniform distribution of 1.66 MBq Ga-68 with half-life 271 days. Ga-68 is the short-lived positron-emitting daughter nucleus of the long-lived Ge-68. The simulation included the energy spectrum of Ga-68 decay and positron travel.

The simulation and experiment were both 45-minute emission acquisitions with energy window 350-650 keV and coincidence timing window 3.43 ns. The properties of the simulation were identical to those described in Chapter 5. For the simulated data, the GATE add-on was used to generate an attenuation correction sinogram. For the experimental data, a 1-hour Co-57 transmission scan of the phantom (657,000,000 prompts) was performed to generate the attenuation correction sinogram. A 15-hour blank transmission scan and a normalization scan (3 billion prompts) were acquired immediately prior to the experiment.

The simulated emission data were processed according to the workflow described in Chapter 5. Emission images for both simulated and measured data were reconstructed with 2D FBP for three cases: with no attenuation correction, with attenuation correction, and with both attenuation and scatter corrections applied. Attenuation correction data generated from the GATE add-on was used for the simulated emission data and transmission scan data was used for attenuation

correction of the emission data acquired on the physical scanner. For the images with both attenuation and scatter corrections, a cylindrical volume of interest (VOI) was drawn in the centre of active region in the image (diameter 39 mm, length 64 mm) and the mean voxel value was measured. Because the precise activity was known, simulated and experimental images for each case were scaled by the same factor so that the mean voxel value within the VOI for the image with scatter and attenuation corrections was 5.23 kBq/cm³.

Horizontal line profiles through the middle of the image were measured for each of the experimental and simulated images to investigate uniformity and the effect of the corrections. To reduce noise, each line profile was averaged across 125 axial planes ($\Delta z = 99.5$ mm) and also across 5 vertical planes ($\Delta y = 3.9$ mm). Line profiles were plotted for the cases with no attenuation correction (no AC), with attenuation correction (AC only), and with both attenuation and scatter correction (AC + SC).

6.3 Results of Validation

6.3.1 Accuracy of Attenuation Maps

The attenuation maps for test A and test B are plotted in Figure 6.5. A comparison of the linear attenuation coefficients used internally by the GATE simulation and the values measured from the attenuation map are summarized in Table 6.1.

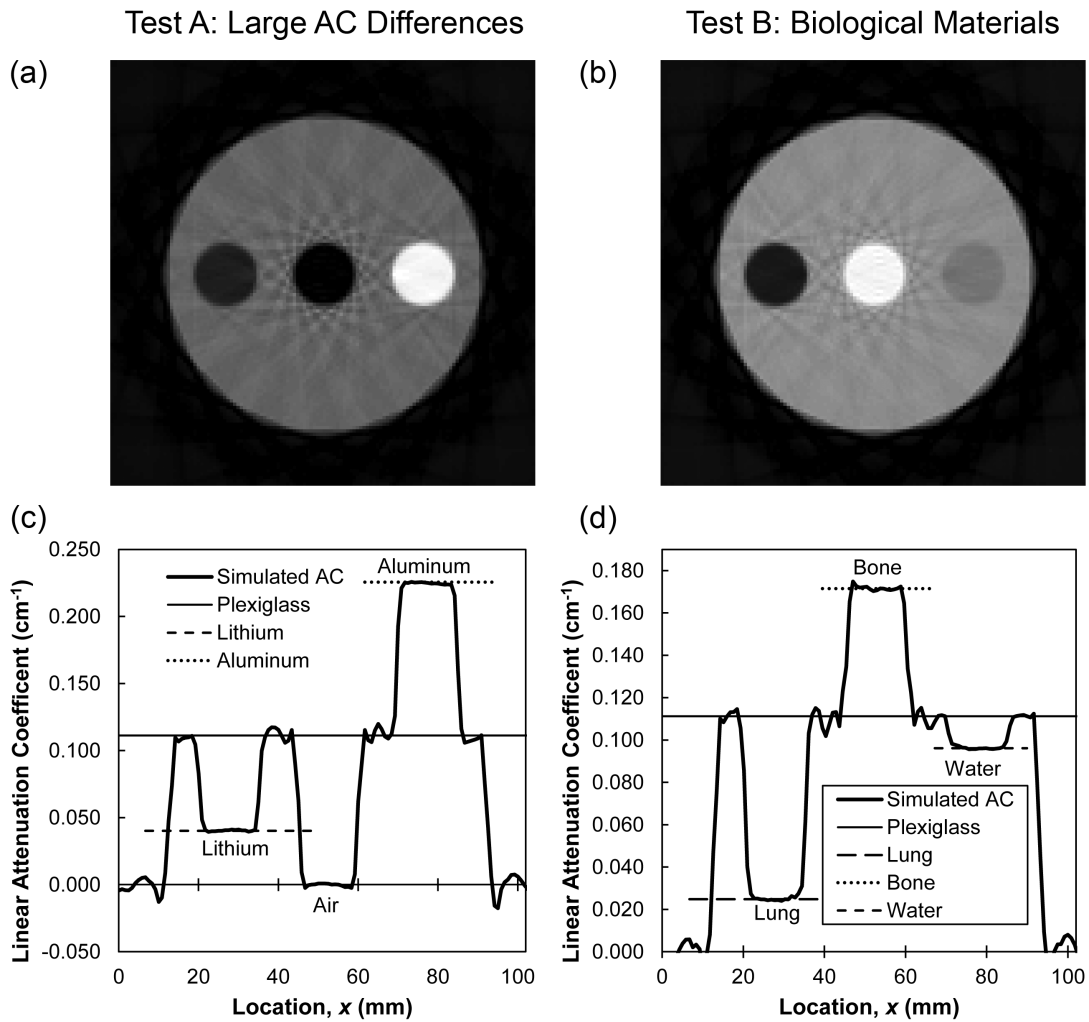


Figure 6.5: (a) & (b) Reconstructed attenuation maps for the two configurations. The greyscale in (a) has a range $0 - 0.23 \text{ cm}^{-1}$ and the range in (b) is $0 - 0.18 \text{ cm}^{-1}$. The streaking visible in the attenuation maps is a property of the discrete number of lines of response and filtered back-projection reconstruction algorithm. (c) & (d) Horizontal line profiles through the centre of the attenuation maps. For each material, the reconstructed attenuation coefficient matched the value generated by the GATE physics models. In the figure, plexiglass refers to PMMA.

Table 6.1: Comparison of linear attenuation coefficients used by the GATE simulation with values measured from the reconstructed attenuation maps.

Material	GATE Internal Linear Attenuation Coefficient (cm ⁻¹)	Linear Attenuation Coefficient in the Reconstructed Image (cm ⁻¹)
PMMA (Test A)	0.1112	0.1111 ± 0.0004 ^a
PMMA (Test B)	0.1112	0.1119 ± 0.0004
Lithium	0.04009	0.0402 ± 0.0002
Air	1.153 × 10 ⁻⁵	(−0.3 ± 0.4) × 10 ⁻⁵
Aluminum	0.2254	0.2252 ± 0.0003
Lung	0.02479	0.0248 ± 0.0001
Bone	0.1714	0.1712 ± 0.0002
Water	0.0962	0.0959 ± 0.0003

^aAll reported uncertainties are standard error of the mean using 110 voxels.

For each material, the linear attenuation coefficients measured from the attenuation map were equal to the values used internally by the emission simulation within the given uncertainties. This result demonstrated that the reconstruction algorithm implemented in the Siemens Inveon Acquisition Workplace software correctly interpreted the attenuation correction sinograms generated by the GATE add-on.

6.3.2 Comparison of Simulated and Measured PET Images

Figure 6.6 compares the attenuation map generated by the GATE add-on with the map generated from the transmission scan. Each map accurately reproduced the correct attenuation coefficient, as provided by the manufacturer, within the phantom. Unlike the measured attenuation map, the map generated by the simulation had no noise.

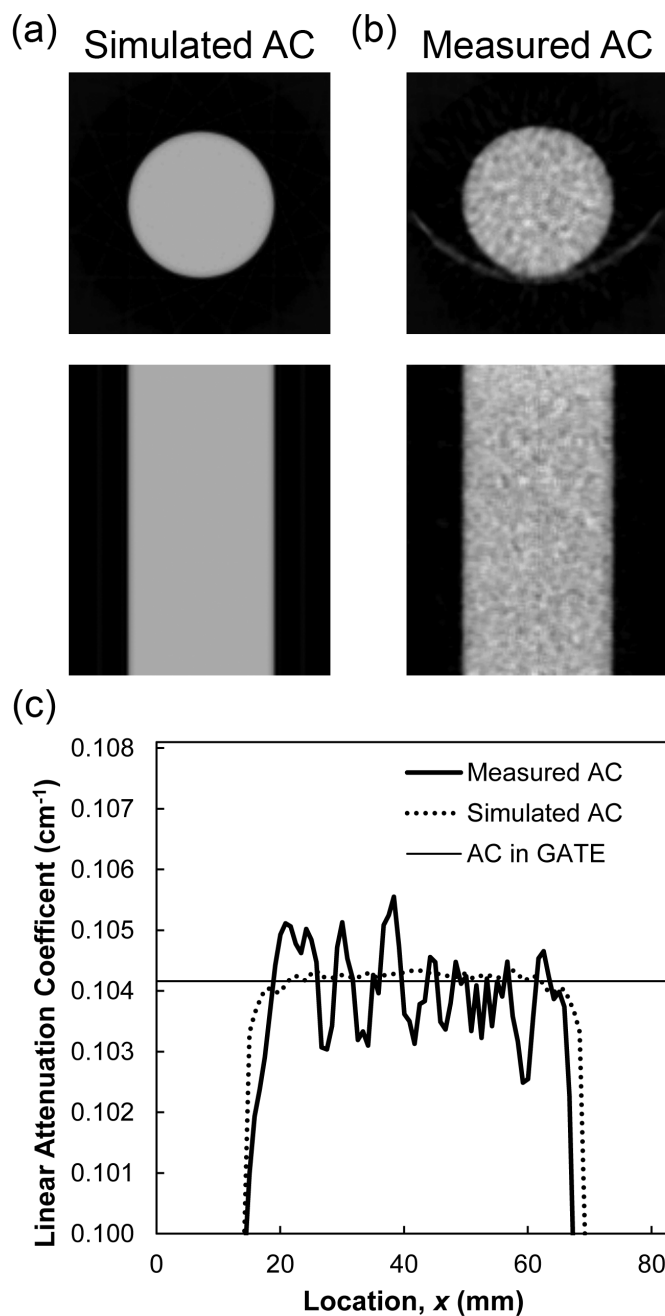


Figure 6.6: Axial and coronal views of the reconstructed attenuation maps generated by the GATE add-on (a) and the transmission scan on the actual scanner (b). They grayscale range is $0 - 0.145 \text{ cm}^{-1}$ for both attenuation maps. (c) Line profiles through both attenuation maps show the agreement between simulated and measured attenuation coefficients.

Reconstructed emission images are shown in Figure 6.7 for the cases with no attenuation correction and with both attenuation and scatter correction applied. A dip in the reconstructed activity was visible in the centres of the images with no attenuation correction. For the images with all corrections applied, the percentage standard deviation in the VOI was 37.7% for the simulated image and 37.4% for the experimental image.

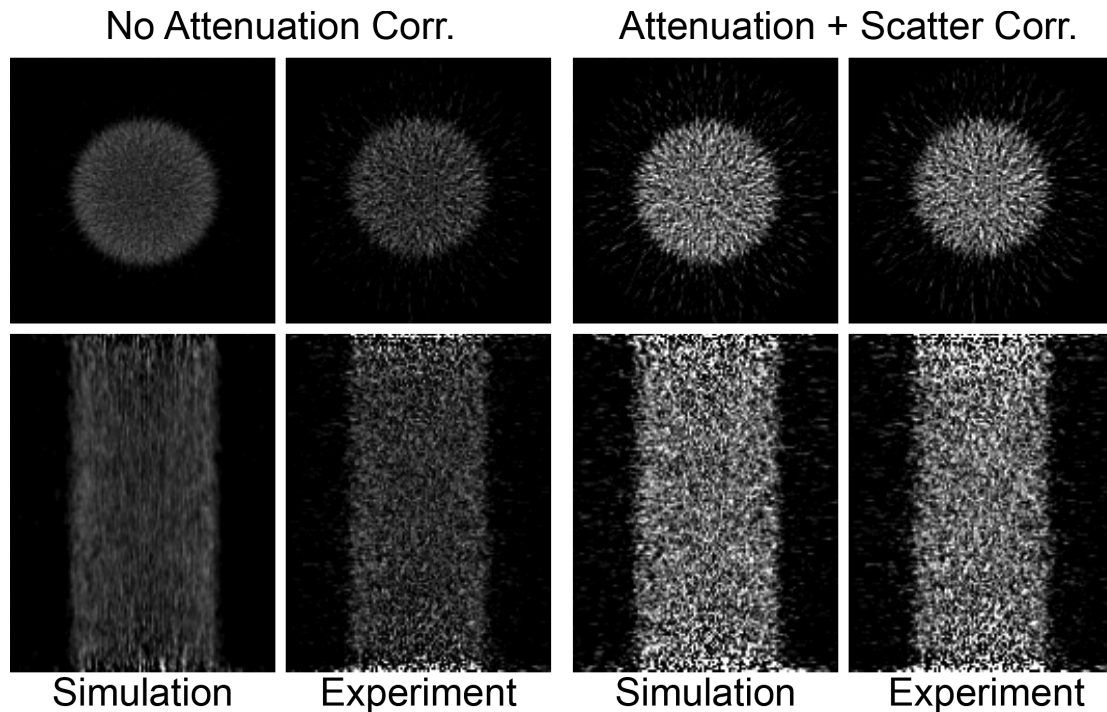


Figure 6.7: Filtered back-projection PET emission images for simulated data and data acquired on the physical scanner. Images reconstructed with no attenuation correction are shown on the left, and those with attenuation and scatter corrections applied are shown on the right. The greyscale range for all images is 1 – 10 kBq/cm³.

Line profiles through the centre of the image are shown in Figure 6.8 for each of the three reconstruction configurations. For the cases with no attenuation correction, the reconstructed activity is lower in the centre of the phantom than the

edges for both simulation and experiment, as expected. Applying attenuation correction without scatter correction appeared to overcompensate for this effect. When scatter correction is applied with attenuation correction, the uniformity of both the simulated and experimental images improved and the noise outside the active region was reduced.

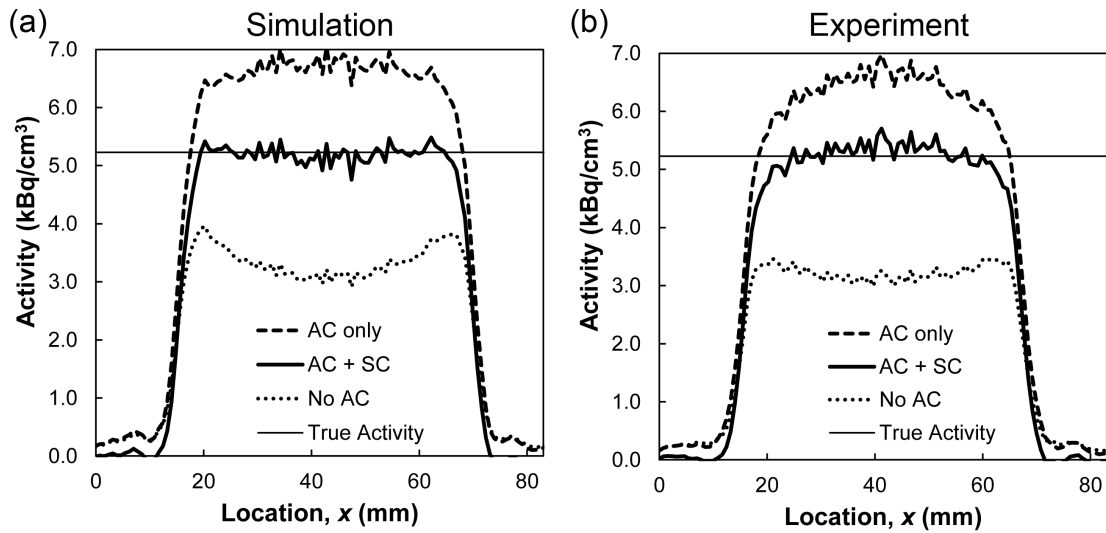


Figure 6.8: Line profiles through the images reconstructed from simulated data (a) and data measured on the actual scanner (b).

6.4 Discussion and Conclusion

The validation tests demonstrate that the GATE add-on produces accurate attenuation correction sinograms in the data format of the Siemens Inveon PET. We have shown that attenuation and scatter corrections are important for rat-sized phantoms.

The GATE add-on approach introduced here has several appealing benefits. The computation time to generate the entire set of attenuation correction sinograms is several minutes on a single workstation computer for a typical small-animal PET

configuration. This is significantly faster than would be the case for simulated CT data, which requires the simulation of a very large number of photons. In addition, this approach uses the 511 keV linear attenuation coefficients computed by the physics models used in the emission simulation. Another important benefit is that the GATE add-on method uses the exact geometry of the phantom and detector ring used in the emission simulation. Any analytic or voxelized geometry can be used, including voxelized animal or human models. This is superior to using a third-party program to compute the attenuation map because it eliminates the possibility of geometric or material mismatch between the emission simulation and the attenuation correction sinogram generation. While the current implementation of the GATE add-on produces an ideal noiseless attenuation correction sinogram, the algorithm can be customized to add noise to mimic that of measured transmission attenuation data, which could be estimated from measured data. In addition, the GATE add-on has been designed to generate attenuation correction sinograms for any PET detector geometry that uses the block-detector configuration and is suitable for modelling both human- and animal-scale scanners.

This approach also has several limitations. Due to the effect of small-angle Compton scattering, the linear attenuation coefficients provided by the GATE physics models slightly overestimate the true photon attenuation within a line of response and the attenuation correction factors must be adjusted to compensate for this effect. The adjustment implemented in the GATE add-on is a simple first-order estimate of the magnitude of the effect. With a better understanding of the effect, a more sophisticated approach that considers the path of the line of

response through the phantom geometry could be added to improve accuracy. The reconstructed attenuation maps were in good agreement with the known attenuation coefficients, suggesting that the assumptions used for the small-angle Compton scattering adjustment were likely reasonable. Another limitation of the GATE add-on is that phantom geometries having interfaces with large differences in attenuation coefficient may produce streak artefacts in attenuation maps because the sinogram does not sample the edges of interfaces perfectly. In a transmission scan on a real scanner, these effects are typically masked by incoherent noise; however, the GATE add-on produces noise-free attenuation sinograms. The computation of attenuation correction factors could be improved by averaging two or more linear paths through each line of response, rather than using one path going from crystal centre to crystal centre.

6.5 References

1. Chow PL, Rannou FR, Chatziioannou AF. Attenuation correction for small animal PET tomographs. *Physics in Medicine and Biology* 2005;50(8):1837-1850.
2. Ollinger JM. Model-based scatter correction for fully 3D PET. *Physics in Medicine and Biology* 1996;41(1):153-176.
3. Watson CC, Newport D, Casey ME, DeKemp RA, Beanlands RS, Schmand M. Evaluation of simulation-based scatter correction for 3-D PET cardiac imaging. *Nuclear Science, IEEE Transactions on* 1997;44(1):90-97.
4. Watson CC. New, faster, image-based scatter correction for 3D PET. *Nuclear Science, IEEE Transactions on* 2000;47(4):1587-1594.
5. Sarrhini O, Bentourkia M. Simultaneous attenuation and scatter corrections from the projections in small animal PET imaging. *Computer Methods and Programs in Biomedicine* 2012;108(3):889-899.
6. Klein O, Nishina T. Über die Streuung von Strahlung durch freie Elektronen nach der neuen relativistischen Quantendynamik von Dirac. *Zeitschrift für Physik* 1929;52(11-12):853-868.
7. Attix FH. *Introduction to radiological physics and radiation dosimetry*. Weinheim: Wiley-VCH; 2004. xxi, 607 p. p.
8. Jan S, Santin G, Strul D, Staelens S, Assie K, Autret D, Avner S, Barbier R, Bardies M, Bloomfield PM *and others*. GATE: a simulation toolkit for PET and SPECT. *Physics in Medicine and Biology* 2004;49(19):4543-4561.
9. Jan S, Benoit D, Becheva E, Carlier T, Cassol F, Descourt P, Frisson T, Grevillot L, Guigues L, Maigne L *and others*. GATE V6: a major enhancement of the GATE simulation platform enabling modelling of CT and radiotherapy. *Physics in Medicine and Biology* 2011;56(4):881-901.
10. Sauerzapf S, Thomas L, Behe M, Weber W, Zakhnini A, Pietrzyk U, Mix M. Using Monte-Carlo Simulations to Implement Corrections for I-124 as a Non-Pure Positron Emitter in Small Animal and Human PET Imaging. 2011 *Ieee Nuclear Science Symposium and Medical Imaging Conference (Nss/Mic)* 2011:2688-2691.
11. Zhang H, Bao QA, Vu NT, Silverman RW, Taschereau R, Berry-Pusey BN, Douraghy A, Rannou FR, Stout DB, Chatziioannou AF. Performance

- Evaluation of PETbox: A Low Cost Bench Top Preclinical PET Scanner. *Molecular Imaging and Biology* 2011;13(5):949-961.
12. Lamare F, Turzo A, Bizais Y, Le Rest CC, Visvikis D. Validation of a Monte Carlo simulation of the Philips Allegro/GEMINI PET systems using GATE. *Physics in Medicine and Biology* 2006;51(4):943-962.
 13. Jan S, Comtat C, Strul D, Santin G, Trebossen R. Monte Carlo simulation for the ECAT EXACT HR plus system using GATE. *IEEE Transactions on Nuclear Science* 2005;52(3):627-633.
 14. Jan S, Frisson T, Sarrut D. GATE Simulation of C-12 Hadrontherapy Treatment Combined With a PET Imaging System for Dose Monitoring: A Feasibility Study. *IEEE Transactions on Nuclear Science* 2013;60(1):423-429.
 15. Konik A, Koesters T, Madsen MT, Sunderland JJ. Evaluation of Attenuation and Scatter Correction Requirements as a Function of Object Size in Small Animal PET Imaging. *IEEE Transactions on Nuclear Science* 2011;58(5):2308-2314.
 16. Vandervoort E, Camborde ML, Jan S, Sossi V. Monte Carlo modelling of singles-mode transmission data for small animal PET scanners. *Physics in Medicine and Biology* 2007;52(11):3169-3184.

Chapter 7

7 Effect of MR-Compatible Bed Materials and RF Coil Components on PET Performance¹

This chapter contains two related Monte Carlo PET investigations. The first is a study of how inclusion of various MR-compatible materials in the animal holder impacts PET performance. The second investigates the effect of discrete RF coil components on PET imaging and the importance of including the RF coil in attenuation correction.

7.1 Monte Carlo PET Simulation of Effect on Image Quality of Various MR-Compatible Animal Bed Materials

7.1.1 Introduction

A single animal imaging bed suitable for both PET and MRI is a requirement for simultaneous techniques and is desirable for sequential methods in order to eliminate animal positioning differences between modalities. It is important to investigate the effects of different MR-compatible bed materials on PET image quality. A suitable material for the animal holder should have low scattering and absorption of photons. A comprehensive Monte Carlo simulation has been developed that uses the actual histogramming and image reconstruction software

¹ The content of this chapter has not been submitted for publication to any journal. Versions of some of the figures and text contained in this chapter have appeared in conference contributions presented by the author.

of the commercial PET system. This process was used to investigate how different MR-compatible bed materials affect PET image quality.

7.1.2 Methods

Simulated PET data were generated with the GEANT4 Application for Tomographic Emission (GATE) package [1,2]. The Siemens Inveon small-animal PET scanner was modelled. The coincidence timing and energy windows were 3.43 ns and 350-650 keV with a 14.6% energy blurring. Simulated emission data were first converted to the list-mode data format of the scanner and then all histogramming and reconstruction were performed in the scanner's software using the method described in Chapter 5. Attenuation correction sinograms were generated within GATE by a custom algorithm that calculates an attenuation correction factor between each crystal pair as described in Chapter 6. OSEM3D-MAP reconstruction was performed with default settings (16 subsets and 4 iterations) and scatter correction was selected. The MAP reconstruction uses prior information about the detector geometry to improve the accuracy of the reconstructed activity map.

The NEMA small animal image quality phantom (see Figure 5.1) with an initial activity of F-18 at 3.7 MBq was simulated for 20 minutes [3]. The decay of F-18 and positron annihilation were included in the simulation. The phantom was located on slightly larger animal bed consisting of a 6.35-mm-thick half-tube with six small lengthwise internal channels for heating water. The bed also contained two delrin tubes for anaesthetic gas. The simulated bed geometry is shown in Figure 7.1.

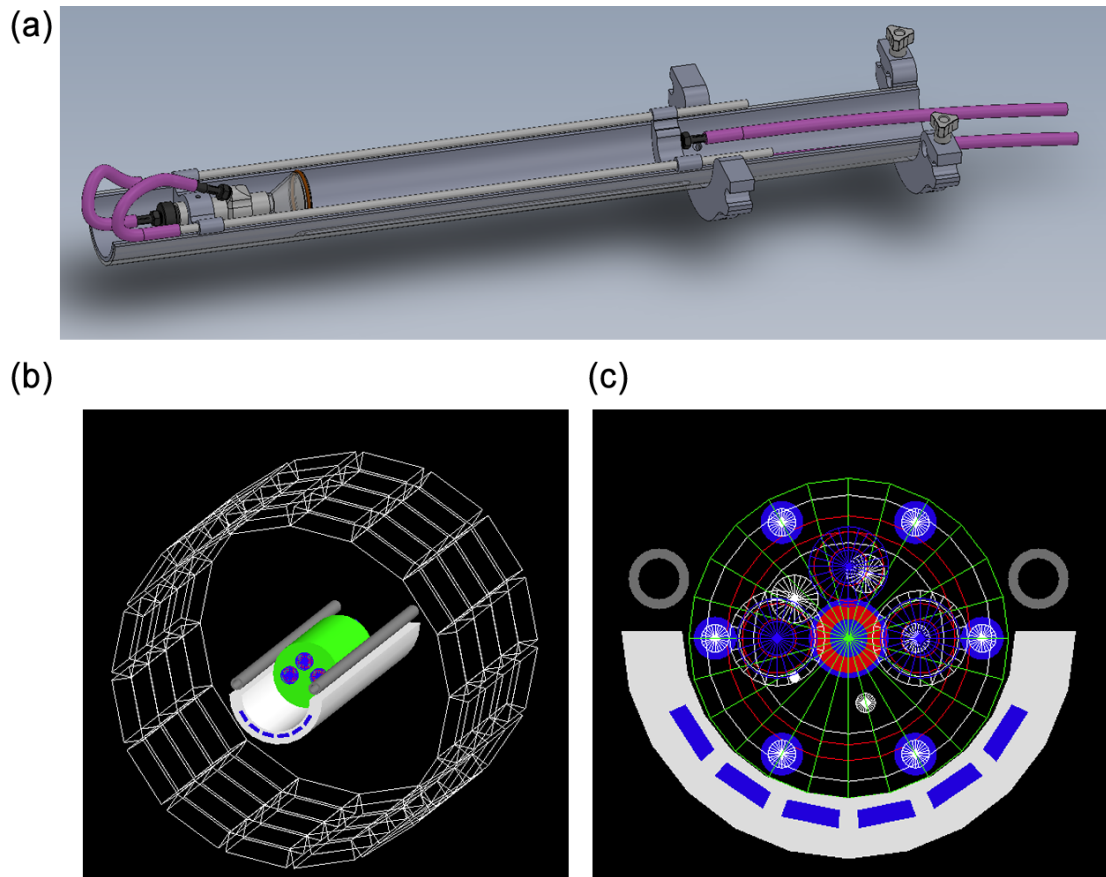


Figure 7.1: (a) CAD model of the PET-MRI mouse bed model. Parallel tubes carry anaesthetic gas to and from the nose cone. All anaesthetic gas and heating water lines connect at the rear of the bed. (b) & (c) Schematic of the simulated phantom geometry. The NEMA NU 4-2008 phantom is shown in green with acrylic screws (blue) and rubber gaskets (red) sitting on the animal holder (white). The blue in the bed corresponds to the heating water channels. The grey rods are delrin anaesthetic gas lines. The white wireframe boxes indicate the position of the PET detector scintillator crystal blocks.

The four different bed materials tested were: PMMA, PVC, G10, and FR4. For comparison, the phantom was also simulated with the standard carbon fibre pallet included with the scanner. Carbon fibre is typically used with PET; however, it is also electrically conductive and thus in some circumstances unsuitable for PET-

MRI due to RF heating [4]. A summary of the densities and elemental compositions or mass fractions of the simulated materials is given in Table 7.1.

Table 7.1: Material definitions used in PET simulations for MR-compatible animal holders.

Material	Density (g/cm ³)	Elemental Composition (mass fraction)
PMMA ^a	1.19	Hydrogen (0.080538) Carbon (0.599858) Oxygen (0.319614)
PVC	1.65	Hydrogen (n = 3) Carbon (n = 2) Chlorine (n = 1)
G10	1.70	Hydrogen (0.0660184) Carbon (0.268193) Oxygen (0.417187) Silicon (0.219883) Chlorine (0.0287186)
FR4	1.70	Hydrogen (0.0684428) Carbon (0.278042) Oxygen (0.405633) Silicon (0.180774) Bromine (0.0671092)
Carbon Fibre	1.58	Hydrogen (0.043) Carbon (n = 0.845) Nitrogen (n = 0.112)

^aPMMA is included as ‘plexiglass’ in the default GATE materials definition file.

Each image was scaled by a single calibration factor such that the mean voxel value was 1 in the uniform region of the carbon fibre case. Recovery coefficients

for activity-filled rods of various diameters, and the spill over ratios (SORs) for the water- and air-filled cold regions were computed according to the methods described in Chapter 5.

7.1.3 Results

The normalized mean activities in the uniform region, percentage standard deviations, SORs and scatter fractions are summarized in Table 7.2 for various bed materials. Recovery coefficients for various rod diameters are shown in Figure 7.2. PMMA and PVC tended to have better performance measures than G10 and FR4. The differences in SOR values between each material were statistically significant ($p < 0.01$, using Student's t-test).

Table 7.2: Simulated PET Performance Measures for Various Bed Construction Materials.^a

Bed Material	Mean in Uniform Region (Normalized to Carbon Fibre)	Percent Standard Deviation (%)	SOR, Water Cavity (%)	SOR, Air Cavity (%)	Total Coincidences (prompts) ($\times 10^8$)	Fraction of Coincidences Scattered (%)
Carbon Fibre Pallet	1.0000	4.53	6.58	4.77	2.1968	16.6
PMMA	0.9969	5.67	5.72	3.82	2.1709	17.7
PVC	0.9977	5.72	6.49	4.21	2.1706	17.4
G10	0.9986	6.73	7.36	4.25	2.1402	18.5
FR4	0.9992	6.53	7.69	4.10	2.1403	18.5

^aThe uncertainty in the SOR values was ± 0.01 in each case (standard error).

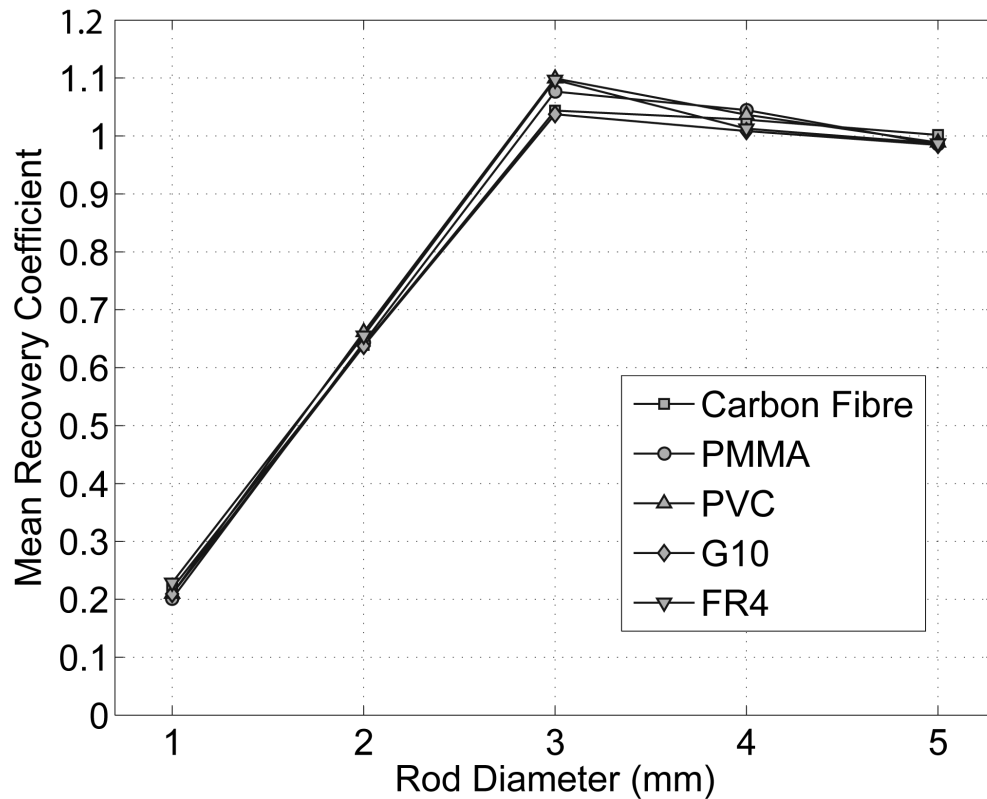


Figure 7.2: Mean recovery coefficient associated with each activity-containing rod for various animal bed materials.

7.1.4 Discussion and Conclusions

The results suggest that of the MR-compatible bed materials tested, PMMA had the least impact on PET image quality when compared with the standard carbon fibre pallet. Overall, PMMA and PVC tended to have better performance measures than G10 and FR4. While differences in some performance metrics were significant between materials, none of the four materials tested resulted in a severe degradation in PET image quality compared with the carbon fibre pallet. Therefore, a wider range of materials could be considered when developing a PET-MRI bed system.

7.2 Design Considerations of RF Coils for PET-MRI Applications and their Impact on PET Performance

7.2.1 Introduction

Attenuation correction of PET images is necessary for obtaining quantitative results. Methods of MR-based attenuation correction typically involve using MR data to segment materials having different attenuation properties, such as soft tissue, air, lung and bone [5,6], and several other alternate methods have been proposed [7-9]. In simultaneous PET-MRI, the RF coil must be located inside the PET detector ring. While this can be avoided in sequential PET-MRI with two separate scanners, it is sometimes desirable to have an RF coil built into the patient or animal handling system which remains in place during PET acquisition. Herrick, *et al.* have used a Monte Carlo simulation to show that the presence of RF coil materials within a PET detection system can result in a significant increase in photon scattering [10]. Increased scattering and absorption result in greater image noise and lower detection sensitivity. Furthermore, many RF coils consist of a symmetrical arrangement of discrete highly attenuating components: copper, solder and capacitors.

RF coil components in the PET field of view introduce additional sources of photon scatter and attenuation. MR-based attenuation correction schemes are complicated by the fact that the RF coil does not appear in the MR image. Since the RF coil does not appear in the MR image, non-MR attenuation correction methods are required. The most common approach is to combine a CT attenuation map of the RF coil with the MR-generated attenuation map to produce a full attenuation map [7]. This approach requires the precise alignment of CT and MR

image spaces, which is not always practical, especially for flexible coils or those with variable positioning. In these cases, RF coil attenuation correction is sometimes omitted. For flexible surface coils typically used in human scanners, global sensitivity losses of up to 5% have been observed with even greater local effects in PET images near RF coil elements [11,12]. In this section, I use a Monte Carlo simulation to investigate and identify any significant effects the RF coil components have on PET image quality. I also explore the effect of omitting RF coil attenuation correction on the quantitative accuracy of PET images.

7.2.2 Methods

7.2.2.1 Monte Carlo Simulation Architecture

Simulated PET data were generated with the GEANT4 Application for Tomographic Emission (GATE) package version 6.1, which is based on the GEANT4 Monte Carlo toolkit [1,2]. There are three stages to PET image generation: data acquisition, histogramming data into sinograms and reconstruction. The Siemens Inveon dedicated small-animal PET scanner was modeled. The detector is composed of 4 axial 16-block rings with each block containing a 20 x 20 array of lutetium oxyorthosilicate (LSO) scintillator having dimensions (1.51 x 1.51 x 10) mm. Coincidence energy and timing windows were set to 350-650 keV and 3.43 ns, with a 14.6% energy blurring applied.

In order to make the image generation workflow as close as possible to an experimental PET workflow, simulated emission data were first converted to the raw list-mode data format of the commercial PET scanner and then all histogramming and reconstruction were performed in the commercial software

according to the method described in Chapter 5. Normalization of the PET detection scheme was accomplished by acquiring simulated coincidence data from a uniform cylindrical Ge-68 source (radius: 3 cm, length: 12.7 cm) for a total of 3 billion coincidences, followed by conversion to list-mode format and histogramming by the component-based method implemented in the commercial software. Attenuation correction (AC) sinograms were generated within GATE by the custom algorithm described in Chapter 6 that computes the attenuation correction factor for each line of response (crystal centre to crystal centre) using the material definitions, phantom geometry and interaction cross-sections used internally by the emission simulation. All emission reconstructions were performed in the commercial software using the two-dimensional Ordered Subset Expectation Maximization (OSEM2D) method with default settings (16 subsets and 4 iterations, Fourier rebinning) including scatter correction using the direct analytical calculation method built into Inveon Acquisition Workplace where indicated.

7.2.2.2 Phantom and RF Coil Model

The mouse-sized phantom, shown in red in Figure 7.3, consisted of a water-filled acrylic cylinder (inner radius: 15 mm, outer radius: 16.75 mm, length: 60 mm) centred in the field of view. The water volume contained a uniform initial activity of the positron emitter F-18 at 3.7 MBq with each simulation lasting 20 minutes. The decay of F-18 and positron annihilation were included in the simulation. The phantom was located on a slightly larger animal bed (described in section 7.1.2) consisting of a 6.35-mm-thick acrylic half-tube with six small lengthwise internal

channels for heating water. The bed also contained two delrin tubes for anaesthetic gas.

An RF coil was modelled as an 8-rung birdcage coil just wide enough to contain the bed and phantom. The conductor consisted of copper tape (thickness: 0.2 mm, width: 6 mm), shown yellow, placed on a 3-mm-thick acrylic former, not shown. Two 5-mm-thick end plates, not shown, supported a RF shield (copper thickness: 0.03 mm) at 1.4 times the radius of the RF coil supported by a 3-mm-thick acrylic former, shown in wireframe. Two models of an 8-rung birdcage RF coil were tested: a band-pass coil and a high-pass coil. For the band-pass coil, sets of two capacitors (combined dimensions: 1.86 x 2.55 x 5.1 mm) were placed at the centre of each rung and between each rung connection on each end ring of the coil. The high-pass coil had no capacitors on the axial rungs and instead had a continuous strip of copper. The capacitor material was chosen to be a 1:1 mixture of BaTiO₃ and Pd₇₀Ag₃₀ for the body, shown green, and Cu₉₀Sn₁₀ for the terminators, shown blue. Lead-free Sn_{95.8}Ag_{3.5}Cu_{0.7} solder joints (thickness: 1.5 mm), shown grey, connected each conductor rung to the end rings and each capacitor to the copper conductor. Attenuation maps reconstructed from the simulated attenuation correction sinograms by filtered back-projection show the linear attenuation coefficients for the phantom, bed, and various coil configurations in Figure 7.4.

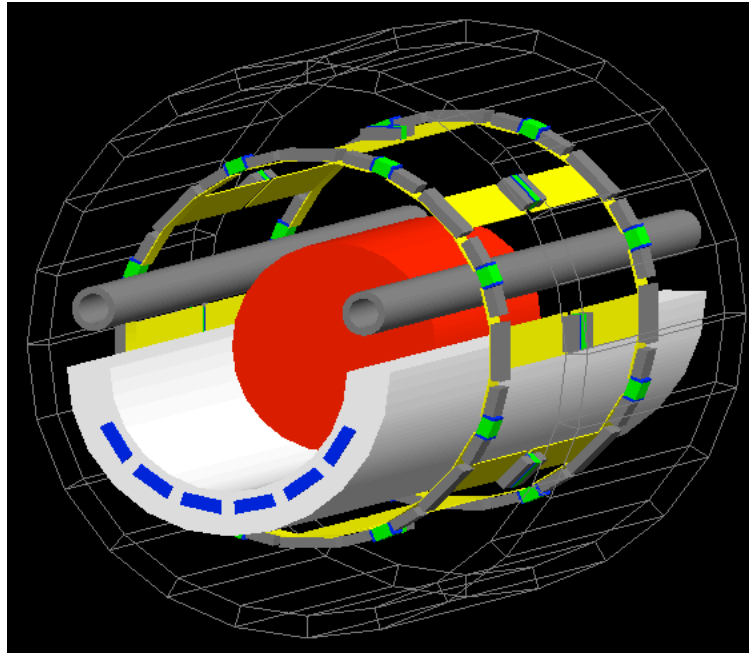


Figure 7.3: Simulation geometry. The band-pass birdcage coil model with low-pass capacitors on the rungs is shown. A high-pass coil was also modeled which had no capacitors on the rungs. The homogenous cylindrical phantom, shown in red, rests on the same PET bed model discussed earlier. The RF coil consists of the following materials: copper tape (yellow), capacitors (green), terminators (blue), and solder (grey). The RF coil is supported by a copper former (not shown) and the wireframe shows the location of the RF shield.

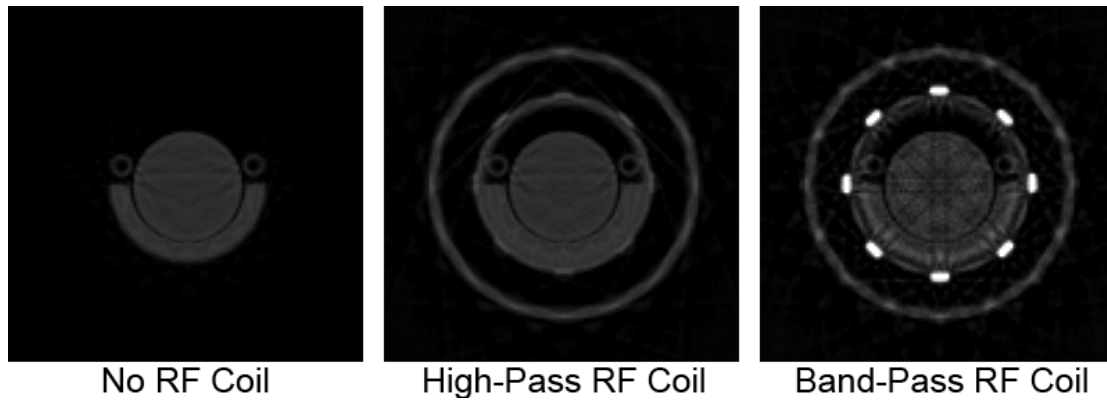


Figure 7.4: 511 keV attenuation maps of the central transverse plane with no RF coil (left), the high-pass RF coil (middle), and the band-pass RF coil (right). The maps show linear attenuation coefficient and were reconstructed from the attenuation correction sinogram. The capacitor attenuation coefficient was $\sim 0.7 \text{ cm}^{-1}$; however, all maps were windowed with a scale $0 - 0.4 \text{ cm}^{-1}$. A smoothing filter (linear interpolation) was applied. In the band-pass RF coil attenuation map, the streaks are due to the abrupt difference in attenuation coefficient between the capacitors and the adjacent material and arise because of the nature of the sampling of the sinogram and reconstruction algorithm.

7.2.2.3 Simulation Setup and Image Analysis

Two investigations were performed: The first test compared PET image noise and artefacts for the cases with and without the band-pass RF coil present, applying all corrections. The purpose was to analyse images from the best and worst case scenarios. The second test compared images reconstructed with and without the RF coil included in the attenuation correction for the cases with the band-pass coil, the high-pass coil and no RF coil. The purpose was to investigate the errors introduced by not including the RF coil in attenuation correction.

For the first test, two cases were modelled with full attenuation and scatter corrections: with the RF coil and without the RF coil. Statistics were recorded for

prompts (total coincidences), scatters (coincidences with at least one Compton scatter interaction), randoms (coincidences originating from different decays) and trues (valid coincidences with no scattering). Each image was scaled so that the total activity in the region of activity matched the known activity. The standard deviation of the reconstructed activity in the voxels in the region of activity was computed.

For the second test, three emission simulations were performed: with no RF coil, with a high-pass coil and with a band-pass coil. All images included attenuation correction for the bed and phantom. For the cases with an RF coil present, images were reconstructed with and without the attenuation correction of the RF coil. For ease of comparison, each image was scaled with the same factor such that the mean activity per voxel in the phantom volume was 100 for the image with no RF coil. Variations in reconstructed activity along the axial length of the phantom were investigated by averaging the activity in groups of four adjacent slices and plotting the difference from the mean activity of the entire phantom. Images were also compared with scatter correction enabled or disabled in the image reconstruction algorithm to test the effectiveness of including this correction on the quantitative accuracy of the reconstructed activity.

7.2.3 Results

7.2.3.1 Comparison With and Without Band-Pass RF Coil

Data for the emission simulation and image analysis are shown in Table 7.3 for the cases with and without the band-pass RF coil. The scatter fraction was significantly greater for the simulation with the RF coil. Figure 7.5 shows the reconstructed PET images for both cases. The standard deviations of the activity in the case with no RF coil and with the RF coil were 4.0 Bq/voxel and 5.0 Bq/voxel, respectively, where the actual activity in each water voxel was 41.9 Bq.

Table 7.3: Comparison of simulation results for the cases with and without RF coil.

Property	No RF Coil	Band-Pass RF Coil	Percent Change (relative to no RF)
prompts	207×10^6	190×10^6	− 8.2 %
true	168×10^6	140×10^6	− 17 %
scatters	36×10^6	47×10^6	+ 30 %
randoms	2.3×10^6	2.1×10^6	− 8.7 %
scatter fraction	17.4 %	24.7 %	+ 42 %
total sensitivity	4.96 %	4.55 %	− 8.3 %
percentage standard deviation	9.5 %	11.9 %	+ 25 %

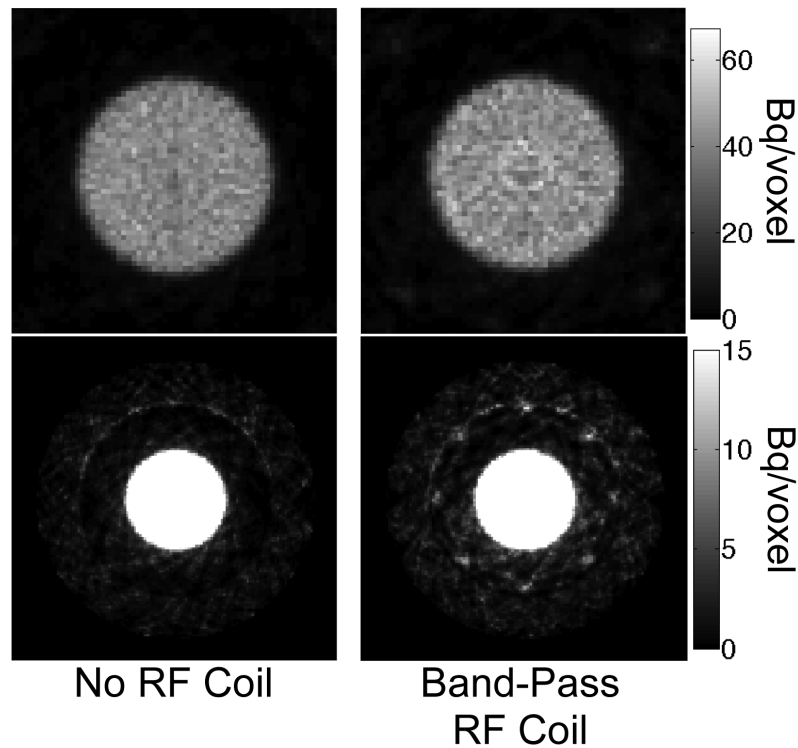


Figure 7.5: Reconstructed PET images showing the central axial slice. The greyscale has units Bq/voxel. The images on the left correspond to the simulation with no RF coil present, and those on the right are for the case with the RF coil, including the RF coil in attenuation and scatter corrections. The top row shows the PET images with a zoom factor of 2 and full greyscale. Increased noise (25% higher standard deviation) and a circular-shape artifact are apparent in the RF coil image (top right) when compared to the case with no RF coil (top left). The bottom row shows the full field of view windowed to make the background noise visible. The case with the RF coil (bottom right) shows significantly increased noise outside the phantom when compared with the case with no RF coil (bottom left). A symmetric artifact arising from the ring of 8 capacitors is evident.

7.2.3.2 Effect of Omitting the RF Coil in Attenuation Correction

With the RF coils included in the attenuation correction, the reconstructed activity matched that of the image with no RF coil within two percent. Omitting the RF

coil from the attenuation correction resulted in a significant drop in the reconstructed activity, as shown in Figure 7.6. When no attenuation correction was applied, the mean activity was reduced to 60-70% of the correct value, depending on the whether an RF coil was present.

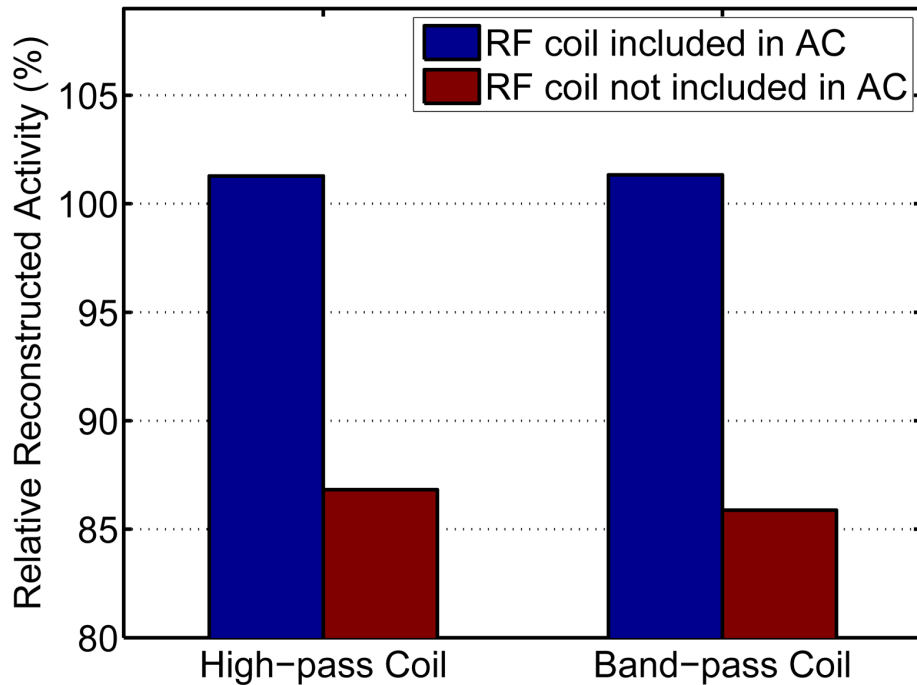


Figure 7.6: Relative reconstructed activities averaged over the phantom volume are shown for simulations with the two RF coil models and scatter correction. The activity values are scaled to a reference image from a simulation with no RF coil present (100%). Omitting the RF coil in the attenuation correction (AC) results in a significant underestimation of the activity. Error bars were too small to be visible.

Figure 7.7 shows how the reconstructed activity varied axially along the phantom for various cases. Deviations from the average phantom activity of several percent were apparent in the central region for the band-pass RF coil. Table 7.4 shows the

effect of scatter correction on the mean relative activity for images with full attenuation correction.

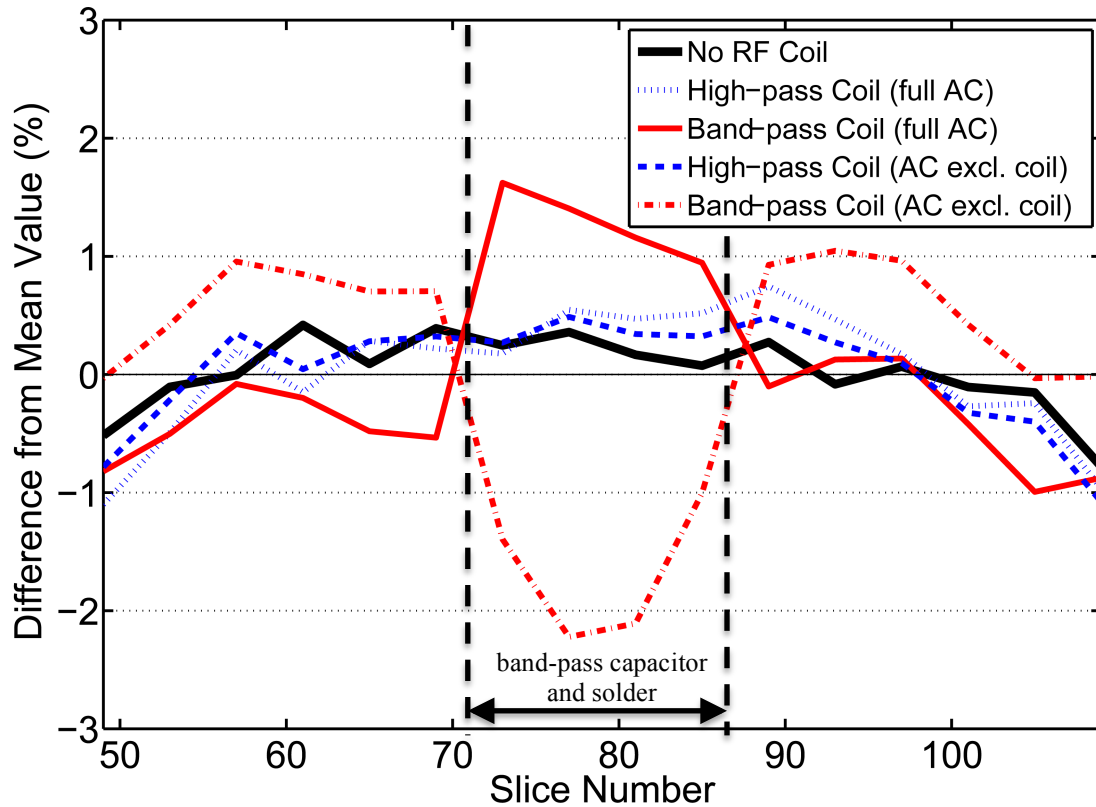


Figure 7.7: Axial profile of the mean activity with scatter correction. Four slices were averaged to produce each data point. The presence of rung capacitors in the band-pass coil results in greater variation across the image along the axial direction.

Table 7.4: Mean relative activity in the central slice for scatter correction enabled or disabled.

	Scatter Correction Enabled	Scatter Correction Disabled
No RF Coil (reference)	100	100
High-Pass RF Coil	100.9 ± 0.3	102.6 ± 0.3
Band-Pass RF Coil	101.6 ± 0.3	103.8 ± 0.3

7.2.4 Discussion and Conclusions

A Monte Carlo simulation that used the histogramming and reconstruction software of the commercial system modelled showed that the presence of discrete RF coil components, specifically capacitors and solder, within the PET field of view results in a significant increase in image noise and a potential for image artefacts. This study suggests that birdcage RF coils with capacitors located in the middle of the rungs (band-pass) are not suitable for combined PET-MRI. Care must also be taken when designing array coils for PET-MRI due to the high number of discrete capacitor components surrounding the subject in close proximity. The use of high-channel number array coils remains an outstanding problem for human simultaneous PET-MRI. 32 channel (and higher) receive coil arrays are critical for accelerated imaging and there is no obvious way to design these coils without discrete components in the field of view. Currently, CT attenuation data of rigid RF coils in human PET-MRI scanners are included in the PET reconstruction, but the attenuation from flexible array coils is not considered.

The Monte Carlo PET simulations also showed that for PET-MRI studies to be quantitative, it is necessary to include the RF coil in the attenuation correction. Attenuation correction is especially important in applications where RF coils with capacitors in the PET field of view cannot be avoided. Even with attenuation correction, discrete components in RF coils located within the PET field of view can result in increased variations in reconstructed activity across the PET image. Analysis of images with and without scatter correction showed that scatter correction could improve quantitative accuracy by several percent with an RF coil present.

7.3 References

1. Jan S, Santin G, Strul D, Staelens S, Assie K, Autret D, Avner S, Barbier R, Bardies M, Bloomfield PM *and others*. GATE: a simulation toolkit for PET and SPECT. *Physics in Medicine and Biology* 2004;49(19):4543-4561.
2. Jan S, Benoit D, Becheva E, Carlier T, Cassol F, Descourt P, Frisson T, Grevillot L, Guigues L, Maigne L *and others*. GATE V6: a major enhancement of the GATE simulation platform enabling modelling of CT and radiotherapy. *Physics in Medicine and Biology* 2011;56(4):881-901.
3. National Electrical Manufacturers Association. NEMA Standard Publication NU 4-2008: Performance Measurements of Small Animal Positron Emission Tomographs. Rosslyn, VA: National Electrical Manufacturers Association; 2008.
4. Liu Y, Shen J, Kainz W, Qian S, Wu W, Chen J. Numerical investigations of MRI RF field induced heating for external fixation devices. *Biomedical Engineering Online* 2013;12:12.
5. Martinez-Moller A, Souvatzoglou M, Delso G, Bundschuh RA, Chefd'hotel C, Ziegler SI, Navab N, Schwaiger M, Nekolla SG. Tissue classification as a potential approach for attenuation correction in whole-body PET/MRI: evaluation with PET/CT data. *Journal of Nuclear Medicine* 2009;50(4):520-526.
6. Berker Y, Franke J, Salomon A, Palmowski M, Donker HC, Temur Y, Mottaghy FM, Kuhl C, Izquierdo-Garcia D, Fayad ZA *and others*. MRI-based attenuation correction for hybrid PET/MRI systems: a 4-class tissue segmentation technique using a combined ultrashort-echo-time/Dixon MRI sequence. *Journal of Nuclear Medicine* 2012;53(5):796-804.
7. Wagenknecht G, Kaiser HJ, Mottaghy FM, Herzog H. MRI for attenuation correction in PET: methods and challenges. *Magnetic Resonance Materials in Physics Biology and Medicine* 2013;26(1):99-113.
8. Navalpakkam BK, Braun H, Kuwert T, Quick HH. Magnetic resonance-based attenuation correction for PET/MR hybrid imaging using continuous valued attenuation maps. *Investigative Radiology* 2013;48(5):323-332.
9. Hofmann M, Bezrukov I, Mantlik F, Aschoff P, Steinke F, Beyer T, Pichler BJ, Scholkopf B. MRI-based attenuation correction for whole-body PET/MRI: quantitative evaluation of segmentation- and atlas-based methods. *Journal of Nuclear Medicine* 2011;52(9):1392-1399.

10. Herrick PDE, Ansorge RE, Hawkes RC, Sawiak SJ, Stevick JW, Carpenter TA. Radiofrequency coil design for simultaneous PET/MR systems. 2010 Oct. 30 2010-Nov. 6 2010. p 2560-2567.
11. Paulus DH, Braun H, Aklan B, Quick HH. Simultaneous PET/MR imaging: MR-based attenuation correction of local radiofrequency surface coils. Medical Physics 2012;39(7):4306-4315.
12. Tellmann L, Quick HH, Bockisch A, Herzog H, Beyer T. The effect of MR surface coils on PET quantification in whole-body PET/MR: results from a pseudo-PET/MR phantom study. Medical Physics 2011;38(5):2795-2805.

Chapter 8

8 Conclusion and Future Work

8.1 Thesis Summary

The central aim of this thesis was to investigate approaches of combining MRI with small animal PET systems with detectors based on photomultiplier tubes (PMT). Various aspects of PET-MRI system integration and design considerations were explored through experimentation and Monte Carlo simulation.

MRI provides excellent soft tissue contrast for imaging anatomy, while PET provides functional information about cellular metabolism with exceptional sensitivity. Combining PET with MRI in a dual-modality system provides the ability to co-register PET images with anatomical features, among other benefits. Thus, approaches for developing combined PET and MRI systems are of great interest. The physics challenge of this integration arises from the incompatibility of conventional PET detectors containing PMTs with magnetic fields. Several tactics to overcome this include the following: PMTs can be replaced with solid-state detectors immune to magnetic fields, the MRI system can be adapted to accommodate conventional PET detectors or MRI and PET systems can be separated sufficiently to minimize interference. The majority of research in the past five years has been focused on developing MR-compatible PET inserts for simultaneous imaging. This thesis describes the exploration and development of the latter two approaches to PET-MRI.

A high-performance commercial small animal PET scanner was obtained and methods of integrating this PET system with MRI were investigated. Chapter 2 described magnetic field exposure experiments on the PET system to characterize performance and image quality as a function of magnetic field. The results of this experiment established external magnetic field limits, indicating that the PET system could be operated during exposure to fields up to 0.9 mT with negligible effect on image quality. Based on this field limit, Chapter 3 surveyed a wide range of approaches to combining the PET system with various configurations of field-cycled MRI and superconducting MRI systems. For each case, a design study was conducted and the advantages and shortcomings were discussed. A feature of field-cycled MRI is that all magnetic fields can be turned off rapidly, enabling the use of conventional PMT-based PET detectors. Chapter 4 described the integration of a prototype PET system using conventional PMT-based detectors with a field-cycled MRI scanner. Interleaved PET and MRI acquisition of a dual modality phantom was performed, generating a co-registered PET-MRI image and demonstrating the feasibility of this approach. Next, a Monte Carlo PET simulation workflow was implemented to inform the design of animal holders compatible with both PET and MRI and to investigate the impact of the presence of a radiofrequency coil on PET image quality. Chapter 5 introduced a sophisticated simulation workflow where the simulated PET data were converted to the raw list-mode data format of the commercial scanner modelled. This approach was implemented so that the histogramming and image reconstruction pathways of the simulated data matched those of the experimentally acquired data. The simulation was validated against experimental data in Chapter 5 using a highly precise GATE model for the NEMA NU 4-2008 image quality phantom.

Chapter 6 introduced a novel method of rapidly generating attenuation correction sinograms for simulated PET studies using an add-on built into GATE. Several validation tests demonstrated the effectiveness of this approach. Finally, in Chapter 7, Monte Carlo PET studies were performed to investigate the impact of different MR-compatible bed materials on PET performance and image quality. Furthermore, simulations were used to study the impact of discrete RF coil components on photon scattering, attenuation and image quality, and to investigate the importance of including the RF coil in attenuation correction on the quantitative accuracy of PET images.

8.2 Future Work

Several designs for combining the commercial PET system with MRI were explored in this thesis. A design for removing the PET detector ring from the Siemens Inveon and inserting it into a new field-cycled MRI scanner was considered, but not pursued. A design study showed that building a field-cycled MRI system for docking on the end of the PET system, using a track to move the animal holder between scanners, was feasible and could be considered for further development. Next, the concept of placing the PET scanner in the vicinity of a conventional superconducting MRI system was investigated. Designs for active electromagnet shield coils to null the magnetic field in the PET detectors were investigated; however, this approach introduces unnecessary complication when compared to the alternative of physically separating the scanners within the same room. Therefore, small animal MRI facilities that have sufficient floor space should consider the simple approach of placing the PET system in a location where the fringe magnetic field is below 0.9 mT.

The magnetic field exposure tests in Chapter 2 were limited to fields oriented in the axial direction of the PET system. In general, due to physical room constraints, the optimal location for a PET system in an MR suite may be such that the fringe field at the PET detectors is oriented in a non-axial direction. Additional experiments are needed to characterize the performance of the PET system when exposed to fields in a variety of directions. This would necessitate either the use of a larger coil than the one used in Chapter 2 or moving the PET system within the fringe field of an actual MRI system.

The final system integration will require the construction of a common bed that can be used with both PET and MRI modalities, such as the design proposed in Chapter 7. If an RF coil is to be integrated with the bed, the design should ensure that the capacitors are outside the PET field of view.

The Monte Carlo simulation could be made more accurate by including materials part of the actual detector housing, such the thin aluminium cylinder that protects the scintillator crystal rings, including scintillation light detection in the model, and using more sophisticated physics models that are more accurate at low energies. To implement any of these changes it would be necessary to also repeat the normalization simulation, a process that took nearly two months to complete on an 8-CPU computer using the fastest parameters. Access to a computer cluster would allow these modifications to be simulated in a reasonable amount of time.

8.3 Conclusion

Research into combined PET-MRI has developed and expanded rapidly throughout the past fifteen years. This thesis describes several original

contributions to this field. The first hybrid system to combine PET and field-cycled MRI was demonstrated. Results from the magnetic field exposure tests on the Siemens Inveon PET will be important to other institutions considering a sequential PET-MRI small animal imaging facility with both scanners in the same room. The Monte Carlo simulation results yielded useful insights into RF coil design for simultaneous PET-MRI approaches, and the significant consequences of omitting the RF coil from attenuation correction were revealed. In addition to these contributions to the field of PET-MRI research, this thesis includes contributions that are expected to be of broad utility to the GATE PET simulation community, specifically, the novel attenuation correction add-on and the precise implementation of the NEMA NU 4-2008 small animal PET phantoms.

Appendix A

Some of the programs, classes and scripts that were developed during the course of this thesis work may be useful to other researchers. Because they include thousands of lines of code, it is impractical to include the code directly in this thesis document. Instead, the source codes are made available as supplementary data and also on Prof. Chronik's group website, which can be accessed through the website of the Department of Physics and Astronomy at Western University (<http://physics.uwo.ca>). At the time of thesis publication, Prof. Chronik's website was available at the following URL: <http://silverberg.physics.uwo.ca>

A summary of the available codes is given below.

A.1 Code to Convert GATE ROOT Output to Siemens Inveon List-mode Format (*root2lst_multi*)

Description

This C++ program processes GATE ROOT files containing coincidences and outputs a Siemens Inveon list mode data format ".lst" file that can be used by Inveon Acquisition Workplace for making sinograms and reconstruction. The directory where root files are stored should contain files named with the following convention: filename_0.root, filename_1.root, filename_2.root, etc. The user must specify the number of files to process in the directory.

From the command line, the usage for *root2lst_multi* is as follows:

```
root2lst_multi <trues> <num_root_files> <rootfile_path> <output_file_name>
```


<trues>: set to ‘trues’ for only true unscattered coincidences, ‘prompts’ for all prompts, and ‘prompts_plus_delays’ to include random coincidences as delayed event packets.

<num_root_files>: set the number of root files to process in the directory.

<first_root_file_name>: set the path to the first root file. For example:
/Data/inveonPET/inveonPET_0.root.

<output_file_name> set the name of the list-mode file for output. For example:
/Data/inveonPET/filename.lst

Availability

root2lst_multi.cpp

A.2 Batch Script to Split GATE Simulations into Multiple Runs for Parallel Processing on Multi-CPU Computers

Description

This perl script splits large GATE simulation runs into multiple runs of equal time. The user specifies the maximum number of CPUs to use, the start time of the simulation, the number of seconds of simulated time for each run, and the total number of runs. This script requires no compilation and is a simpler alternative to the GATE Job Splitter (‘gjs’) that is distributed with the latest versions of GATE. The script requires the Forks::Super perl package which is available from the code repository at <http://www.cpan.org>. It should be noted that improvements in computation time can be achieved as long as the number of simultaneous runs is

less than or equal to the number of available physical processors. As of GATE 6.1, the use of additional logical processing cores (i.e. through hyper-threading) does not decrease the total computation time.

Availability

gate_batch_splitter.pl

A.3 Specification of the NEMA NU 4-2008 Phantom and Source Macros in GATE

Description

This set contains the GATE macro files for the phantom geometries and source distributions of the small animal PET imaging protocols of the NEMA NU 4-2008 standard. These files can be used to test the accuracy of GATE simulations of small animal PET scanners, regardless of the scanner geometry.

Availability

phantom_nema_image_quality.mac

phantom_nema_point_source.mac

phantom_nema_mouse_scatter.mac

phantom_nema_rat_scatter.mac

phantom_nema_mouse_scatter.mac

source_nema_image_quality.mac

source_nema_point_source.mac

source_nema_mouse_scatter.mac

source_nema_rat_scatter.mac

source_nema_mouse_scatter.mac

A.4 GATE Attenuation Correction Add-on

The GATE attenuation correction add-on consists of two classes and two headers. These must be inserted into the GATE source directory and compiled. To use the GATE add-on to generate an attenuation correction sinogram, the user runs a special GATE macro different from the emission simulation macro. The attenuation macro should call the same phantom and detector macros as the emission simulation. The attenuation correction actor is called after the physics processes are initialized and before the run is initialized as follows:

```
# Initialize Physics Processes
/control/execute physics.mac

# Attenuation Correction Actor
/gate/actor/addActor AttenuationCorrectionActor myAtten
/gate/actor/myAtten/attachTo world
/gate/actor/myAtten/setNumProjectionBins 128
/gate/actor/myAtten/setNumAngleBins 160
/gate/actor/myAtten/setNumAxialSinograms 159
/gate/actor/myAtten/save my_attenuation_sinogram.atn

# Initialize Run
/gate/run/initialize
```

The add-on requires that a source be initialized with the total number of primaries equal to the number of LORs. For the case above, the number of LORs required is $128 \times 160 \times 159 = 3256320$ and the number of primaries can be set as follows:

```
/gate/application/setTotalNumberOfPrimaries 3256320
```

Availability

Sources (../GATE/source/digits_hits/src/):

GateAttenuationCorrectionActor.cc

GateAttenuationCorrectionActorMessenger.cc

Headers (../GATE/source/digits_hits/include/):

GateAttenuationCorrectionActor.hh

GateAttenuationCorrectionActorMessenger.hh

Letters of Permission

JOHN WILEY AND SONS LICENSE TERMS AND CONDITIONS

Jun 11, 2013

This is a License Agreement between Geron A Bindseil ("You") and John Wiley and Sons ("John Wiley and Sons") provided by Copyright Clearance Center ("CCC"). The license consists of your order details, the terms and conditions provided by John Wiley and Sons, and the payment terms and conditions.

All payments must be made in full to CCC. For payment instructions, please see information listed at the bottom of this form.

License Number	3141471178846
License date	May 03, 2013
Licensed content publisher	John Wiley and Sons
Licensed content publication	Magnetic Resonance in Medicine
Licensed content title	First image from a combined positron emission tomography and field-cycled MRI system
Licensed copyright line	Copyright © 2010 Wiley-Liss, Inc.
Licensed content author	Geron A. Bindseil, Kyle M. Gilbert, Timothy J. Scholl, William B. Handler, Blaine A. Chronik
Licensed content date	Feb 1, 2011
Start page	301
End page	305
Type of use	Dissertation/Thesis
Requestor type	Author of this Wiley article
Format	Print and electronic
Portion	Full article
Will you be translating?	No
Total	0.00 USD
Terms and Conditions	

TERMS AND CONDITIONS

This copyrighted material is owned by or exclusively licensed to John Wiley & Sons, Inc. or one of its group companies (each a "Wiley Company") or a society for whom a Wiley Company has exclusive publishing rights in relation to a particular journal (collectively "WILEY"). By clicking "accept" in connection with completing this licensing transaction, you agree that the following terms and conditions apply to this transaction (along with the billing and payment terms and conditions established by the Copyright Clearance Center Inc., ("CCC's Billing and Payment terms and conditions"), at the time that you opened your RightsLink account (these are available at any time at <http://myaccount.copyright.com>).

Terms and Conditions

1. The materials you have requested permission to reproduce (the "Materials") are protected by copyright.

2. You are hereby granted a personal, non-exclusive, non-sublicensable, non-transferable, worldwide, limited license to reproduce the Materials for the purpose specified in the licensing process. This license is for a one-time use only with a maximum distribution equal to the number that you identified in the licensing process. Any form of republication granted by this license must be completed within two years of the date of the grant of this license (although copies prepared before may be distributed thereafter). The Materials shall not be used in any other manner or for any other purpose. Permission is granted subject to an appropriate acknowledgement given to the author, title of the material/book/journal and the publisher. You shall also duplicate the copyright notice that appears in the Wiley publication in your use of the Material. Permission is also granted on the understanding that nowhere in the text is a previously published source acknowledged for all or part of this Material. Any third party material is expressly excluded from this permission.

3. With respect to the Materials, all rights are reserved. Except as expressly granted by the terms of the license, no part of the Materials may be copied, modified, adapted (except for minor reformatting required by the new Publication), translated, reproduced, transferred or distributed, in any form or by any means, and no derivative works may be made based on the Materials without the prior permission of the respective copyright owner. You may not alter, remove or suppress in any manner any copyright, trademark or other notices displayed by the Materials. You may not license, rent, sell, loan, lease, pledge, offer as security, transfer or assign the Materials, or any of the rights granted to you hereunder to any other person.

4. The Materials and all of the intellectual property rights therein shall at all times remain the exclusive property of John Wiley & Sons Inc or one of its related companies (WILEY) or their respective licensors, and your interest therein is only that of having possession of and the right to reproduce the Materials pursuant to Section 2 herein during the continuance of this Agreement. You agree that you own no right, title or interest in or to the Materials or any of the intellectual property rights therein. You shall have no rights hereunder other than the license as provided for above in Section 2. No right, license or interest to any trademark, trade name, service mark or other branding ("Marks") of WILEY or its licensors is granted hereunder, and you agree that you shall not assert any such right, license or interest with respect thereto.

5. NEITHER WILEY NOR ITS LICENSORS MAKES ANY WARRANTY OR REPRESENTATION OF ANY KIND TO YOU OR ANY THIRD PARTY, EXPRESS, IMPLIED OR STATUTORY, WITH RESPECT TO THE MATERIALS OR THE ACCURACY OF ANY INFORMATION CONTAINED IN THE MATERIALS, INCLUDING, WITHOUT LIMITATION,

ANY IMPLIED WARRANTY OF MERCHANTABILITY, ACCURACY, SATISFACTORY QUALITY, FITNESS FOR A PARTICULAR PURPOSE, USABILITY, INTEGRATION OR NON-INFRINGEMENT AND ALL SUCH WARRANTIES ARE HEREBY EXCLUDED BY WILEY AND ITS LICENSORS AND WAIVED BY YOU.

6. WILEY shall have the right to terminate this Agreement immediately upon breach of this Agreement by you.

7. You shall indemnify, defend and hold harmless WILEY, its Licensors and their respective directors, officers, agents and employees, from and against any actual or threatened claims, demands, causes of action or proceedings arising from any breach of this Agreement by you.

8. IN NO EVENT SHALL WILEY OR ITS LICENSORS BE LIABLE TO YOU OR ANY OTHER PARTY OR ANY OTHER PERSON OR ENTITY FOR ANY SPECIAL, CONSEQUENTIAL, INCIDENTAL, INDIRECT, EXEMPLARY OR PUNITIVE DAMAGES, HOWEVER CAUSED, ARISING OUT OF OR IN CONNECTION WITH THE DOWNLOADING, PROVISIONING, VIEWING OR USE OF THE MATERIALS REGARDLESS OF THE FORM OF ACTION, WHETHER FOR BREACH OF CONTRACT, BREACH OF WARRANTY, TORT, NEGLIGENCE, INFRINGEMENT OR OTHERWISE (INCLUDING, WITHOUT LIMITATION, DAMAGES BASED ON LOSS OF PROFITS, DATA, FILES, USE, BUSINESS OPPORTUNITY OR CLAIMS OF THIRD PARTIES), AND WHETHER OR NOT THE PARTY HAS BEEN ADVISED OF THE POSSIBILITY OF SUCH DAMAGES. THIS LIMITATION SHALL APPLY NOTWITHSTANDING ANY FAILURE OF ESSENTIAL PURPOSE OF ANY LIMITED REMEDY PROVIDED HEREIN.

9. Should any provision of this Agreement be held by a court of competent jurisdiction to be illegal, invalid, or unenforceable, that provision shall be deemed amended to achieve as nearly as possible the same economic effect as the original provision, and the legality, validity and enforceability of the remaining provisions of this Agreement shall not be affected or impaired thereby.

10. The failure of either party to enforce any term or condition of this Agreement shall not constitute a waiver of either party's right to enforce each and every term and condition of this Agreement. No breach under this agreement shall be deemed waived or excused by either party unless such waiver or consent is in writing signed by the party granting such waiver or consent. The waiver by or consent of a party to a breach of any provision of this Agreement shall not operate or be construed as a waiver of or consent to any other or subsequent breach by such other party.

11. This Agreement may not be assigned (including by operation of law or otherwise) by you without WILEY's prior written consent.

12. Any fee required for this permission shall be non-refundable after thirty (30) days from receipt

13. These terms and conditions together with CCC's Billing and Payment terms and conditions (which are incorporated herein) form the entire agreement between you and WILEY concerning this licensing transaction and (in the absence of fraud) supersedes all prior agreements and representations of the parties, oral or written. This Agreement may not be amended except in writing signed by both parties. This Agreement shall be binding upon and inure to the benefit of the parties' successors, legal representatives, and authorized assigns.

14. In the event of any conflict between your obligations established by these terms and conditions and those established by CCC's Billing and Payment terms and conditions, these terms and conditions shall prevail.

15. WILEY expressly reserves all rights not specifically granted in the combination of (i) the license details provided by you and accepted in the course of this licensing transaction, (ii) these terms and conditions and (iii) CCC's Billing and Payment terms and conditions.

16. This Agreement will be void if the Type of Use, Format, Circulation, or Requestor Type was misrepresented during the licensing process.

17. This Agreement shall be governed by and construed in accordance with the laws of the State of New York, USA, without regards to such state's conflict of law rules. Any legal action, suit or proceeding arising out of or relating to these Terms and Conditions or the breach thereof shall be instituted in a court of competent jurisdiction in New York County in the State of New York in the United States of America and each party hereby consents and submits to the personal jurisdiction of such court, waives any objection to venue in such court and consents to service of process by registered or certified mail, return receipt requested, at the last known address of such party.

Wiley Open Access Terms and Conditions

Wiley publishes Open Access articles in both its Wiley Open Access Journals program [<http://www.wileyopenaccess.com/view/index.html>] and as Online Open articles in its subscription journals. The majority of Wiley Open Access Journals have adopted the [Creative Commons Attribution License](#) (CC BY) which permits the unrestricted use, distribution, reproduction, adaptation and commercial exploitation of the article in any medium. No permission is required to use the article in this way provided that the article is properly cited and other license terms are observed. A small number of Wiley Open Access journals have retained the [Creative Commons Attribution Non Commercial License](#) (CC BY-NC), which permits use, distribution and reproduction in any medium, provided the original work is properly cited and is not used for commercial purposes.

Online Open articles - Authors selecting Online Open are, unless particular exceptions apply, offered a choice of Creative Commons licenses. They may therefore select from the CC BY, the CC BY-NC and the [Attribution-NoDerivatives](#) (CC BY-NC-ND). The CC BY-NC-ND is more restrictive than the CC BY-NC as it does not permit adaptations or modifications without rights holder consent.

Wiley Open Access articles are protected by copyright and are posted to repositories and websites in accordance with the terms of the applicable Creative Commons license referenced on the article. At the time of deposit, Wiley Open Access articles include all changes made during peer review, copyediting, and publishing. Repositories and websites that host the article are responsible for incorporating any publisher-supplied amendments or retractions issued subsequently. Wiley Open Access articles are also available without charge on Wiley's publishing platform, **Wiley Online Library** or any successor sites.

Conditions applicable to all Wiley Open Access articles:

- The authors' moral rights must not be compromised. These rights include the right of "paternity" (also known as "attribution" - the right for the author to be identified as such) and "integrity" (the right for the author not to have the work altered in such a way that the author's reputation

or integrity may be damaged).

- Where content in the article is identified as belonging to a third party, it is the obligation of the user to ensure that any reuse complies with the copyright policies of the owner of that content.
- If article content is copied, downloaded or otherwise reused for research and other purposes as permitted, a link to the appropriate bibliographic citation (authors, journal, article title, volume, issue, page numbers, DOI and the link to the definitive published version on Wiley Online Library) should be maintained. Copyright notices and disclaimers must not be deleted.
 - Creative Commons licenses are copyright licenses and do not confer any other rights, including but not limited to trademark or patent rights.
- Any translations, for which a prior translation agreement with Wiley has not been agreed, must prominently display the statement: "This is an unofficial translation of an article that appeared in a Wiley publication. The publisher has not endorsed this translation."
- **Conditions applicable to non-commercial licenses (CC BY-NC and CC BY-NC-ND)** For non-commercial and non-promotional purposes individual non-commercial users may access, download, copy, display and redistribute to colleagues Wiley Open Access articles. In addition, articles adopting the CC BY-NC may be adapted, translated, and text- and data-mined subject to the conditions above. **Use by commercial "for-profit" organizations** Use of non-commercial Wiley Open Access articles for commercial, promotional, or marketing purposes requires further explicit permission from Wiley and will be subject to a fee. Commercial purposes include:
 - Copying or downloading of articles, or linking to such articles for further redistribution, sale or licensing;
 - Copying, downloading or posting by a site or service that incorporates advertising with such content;
 - The inclusion or incorporation of article content in other works or services (other than normal quotations with an appropriate citation) that is then available for sale or licensing, for a fee (for example, a compilation produced for marketing purposes, inclusion in a sales pack)
 - Use of article content (other than normal quotations with appropriate citation) by for-profit organizations for promotional purposes
 - Linking to article content in e-mails redistributed for promotional, marketing or educational purposes;
 - Use for the purposes of monetary reward by means of sale, resale, license, loan, transfer or other form of commercial exploitation such as marketing products
 - Print reprints of Wiley Open Access articles can be purchased from: corporatesales@wiley.com
 - The modification or adaptation for any purpose of an article referencing the CC BY-NC-ND License requires consent which can be requested from RightsLink@wiley.com.
- Other Terms and Conditions:
 -
 - BY CLICKING ON THE "I AGREE..." BOX, YOU ACKNOWLEDGE THAT YOU HAVE READ AND FULLY UNDERSTAND EACH OF THE SECTIONS OF AND PROVISIONS SET FORTH IN THIS AGREEMENT AND THAT YOU ARE IN AGREEMENT WITH AND ARE WILLING TO ACCEPT ALL OF YOUR OBLIGATIONS AS SET FORTH IN THIS AGREEMENT.
- **v1.8**

Curriculum Vitae

Name:	Geron Bindseil
Post-secondary Education and Degrees:	<p>Trent University Peterborough, Ontario, Canada 2003-2007 B.Sc. Physics</p> <p>Western University London, Ontario, Canada 2007-2013 Ph.D. Physics</p>
Honours and Awards During Graduate Studies:	<p>Natural Sciences and Engineering Research Council (NSERC) Canada Graduate Scholarship - Masters 2007-2008</p> <p>Natural Sciences and Engineering Research Council (NSERC) Canada Graduate Scholarship - Doctoral 2008-2009, 2009-2010, 2010-2011</p> <p>International Society for Magnetic Resonance in Medicine Magna Cum Laude 2012</p> <p>Faculty of Science, Western University Faculty of Science Graduate Teaching Award 2012</p> <p>Department of Physics & Astronomy, Western University TA Award of Excellence for Demonstrating 2012</p>
Related Work Experience	<p>Teaching Assistant Department of Physics & Astronomy, Western University 2007-2012</p> <p>Learning Development Fellow Faculty of Science, Western University 2012</p>

Publications:

Articles Published in Refereed Journals

Bindseil, G., Scholl, T., Handler, W., Gilbert, K., and Chronik, B. (2011) First Image from a Combined Positron Emission Tomography (PET) and Field-Cycled MRI System. *Magnetic Resonance in Medicine*. 65: 301-305.

Refereed Contributions to Conferences

(* presenting author)

Bindseil, G.*, Handler, W., and Chronik, B. (2012) Monte Carlo PET Simulation of Effect on Image Quality of Various MR-Compatible Animal Bed Materials. 2012 World Molecular Imaging Congress, Dublin, Ireland; p. 348. (Poster, International)

Bindseil, G.*, Handler, W., and Chronik, B. (2012) Discrete RF Coil Components Introduce Significant Noise and Artifacts into PET Images in Combined PET-MRI Systems. 20th International Society for Magnetic Resonance in Medicine Annual Meeting, Melbourne, Australia; p. 0146. (Oral, International)

Bindseil, G.*, Handler, W., and Chronik, B. (2011) Small Animal PET and MRI in the Same Room: Design Considerations and Implementation. 2011 World Molecular Imaging Congress, San Diego, CA; p. 490. (Poster, International)

Bindseil, G.*, Handler, W., and Chronik, B. (2011) Preclinical MRI and PET in a Single Room. 2011 Lawson Research Day, London, Canada; p. 2. (Poster, Institutional)

Bindseil, G.*, Harris, C., Handler, W., Scholl, T., and Chronik, B. (2010) Collinear PET/MRI: External Magnetic Field Limits and Magnetic Shield Design for a Small-Animal PET System. 2010 World Molecular Imaging Congress, Kyoto, Japan; p. 0300B. (Poster, International)

Bindseil, G.*, Scholl, T., Handler, W., Harris, C., and Chronik, B. (2010) Active magnetic shielding of PET detectors for a small-animal multimodality PET/MRI system. 2010 Society of Nuclear Medicine Annual Meeting, Salt Lake City, UT; p. 412. (Oral, International)

Bindseil, G.*, Scholl, T., Handler, W., Harris, C., and Chronik, B. (2010) Design of a Dynamically-Controlled Resistive Shield for a Combined PET and Superconducting MRI System for Small Animal Imaging. 18th International Society for Magnetic Resonance in Medicine Annual Meeting, Stockholm, Sweden; p. 3949. (E-Poster, International)

Bindseil, G.*, Handler, W., Scholl, T., and Chronik, B. (2010) Magnetic Field Exposure Tests on a Siemens Inveon Small Animal PET System: A Feasibility Study for Multimodality PET and Field-Cycled MRI. 18th International Society for Magnetic Resonance in Medicine Annual Meeting, Stockholm, Sweden; p. 1547. (Poster, International)

Bindseil, G.*, Harris, C., Handler, W., Scholl, T., and Chronik, B. (2010) A Small-Animal Hybrid PET-MRI System: Magnetic Shielding of PET Detectors. 2010 Lawson Research Day, London, Canada; p. 34. (Poster, Institutional)

Bindseil, G.*, Scholl, T., Handler, W., Gilbert, K., and Chronik, B. (2009) First Images from a Combined PET and Field-cycled MRI System. 2009 Society of Nuclear Medicine Annual Meeting, Toronto, Canada; p. 1530. (Poster, International)

Bindseil, G.*, Handler, W., Scholl, T., Gilbert, K., and Chronik, B. (2009) First Hybrid Images from a Combined PET and Field-cycled MRI System. 17th International Society for Magnetic Resonance in Medicine Annual Meeting, Honolulu, HI; p. 590. (Oral, International)

Bindseil, G.*, Handler, W., Scholl, T., Gilbert, K., Peng, H., and Chronik, B. (2009) Design of a Docking PET and Field-Cycled MRI System for Small Animal Imaging. 17th International Society for Magnetic Resonance in Medicine Annual Meeting, Honolulu, HI; p. 3089. (Poster, International)

Bindseil, G.*, Handler, W., Scholl, T., Gilbert, K., Peng, H., and Chronik, B. (2008) Design of a Combined PET and Field-Cycled MRI System for Small Animal Imaging. 16th ISMRM Annual Meeting, Toronto, Canada; p. 351. (Oral, International)

Bindseil, G., LeBlanc, Y.*, Burton, L., and Wingate, J. (2006) Identification and Characterization of Metabolites and Markers Indicative of Effectiveness of Schizophrenia Treatment. 54th American Society for Mass Spectrometry Conference. Seattle, WA; p. 461. (Poster, International).